

Overloaded Array Processing:

System Analysis, Signal Extraction Techniques, and Time-delay Estimation

by

Saffet Bayram

Thesis submitted to the faculty of the
Virginia Polytechnic Institute & State University
in partial fulfillment of the requirements of the degree

MASTER OF SCIENCE

in

Electrical Engineering

Approved:

Dr. Jeffrey H. Reed, Chairman

Dr. Robert J. Boyle

Dr. Brian D. Woerner

December 8, 2000

Blacksburg, Virginia

Keywords: Overloaded Array, Joint Detection, Antenna Array, Interference Mitigation

Overloaded Array Processing: System Analysis, Signal Extraction Techniques, and Time-delay Estimation

Saffet Bayram

ABSTRACT

In airborne communication systems such as *airborne cell-extender repeaters* the receiver faces the challenge of demodulating the signal of interest (SOI) in the presence of excessive amounts of Co-Channel Interference (CCI) from a large number of sources. This results in the *overloaded environment* where the number of near-equal power co-channel interferers exceeds the number of antenna array elements. This thesis first analyzes the interference environment experienced by an airborne cellular repeater flying at high altitudes. Link budget analysis using a two-ray propagation model shows that the antenna array mounted on an airborne receiver has to recover the SOI out of hundreds of co-channel interfering signals. This necessitates use of complex *overloaded array signal processing* techniques. An extensive literature survey on narrowband signal extraction algorithms shows that joint detection schemes, coupled with antenna arrays, provide a solution for narrowband overloaded array problem where as traditional beamforming techniques fail. Simulation results in this thesis investigates three “promising” overloaded array processing algorithms, Multi-User Decision Feedback Equalizer (MU-DFE), Iterative Least Squares with Projection (ILSP), and Iterative Least Squares with Enumeration (ILSE). ILSE is a non-linear joint maximum-likelihood detector, is shown to demodulate many more signals than elements even when the users are closely spaced and the channel is blindly estimated.

Multi-user time delay estimation is one of the most important aspects of channel estimation for overloaded array processing. The final chapter of the thesis proposes a low-complexity data-aided time-delay estimation structure for embedding in a Per Survivor Processing (PSP) trellis for overloaded array processing. An extensive analysis proves that the multi-user delay estimation is separable, which leads to the proposed multi-user algorithm that estimates the user

delays with a bank of simple data-aided synchronization loops to reduce the complexity. This thesis shows simulation results for the single-user case where the low-complexity Delay Locked Loop (DLL) structure, working at a low oversampling rate of 2 samples per symbol, estimates and compensates for any integer or non-integer sample delay within $\pm T_{\text{sym}}$ (symbol period).

Two extensions to this technique are proposed to provide efficient multi-user delay estimation. The first multi-user structure employs a bank of DLLs, which compensate for the timing offset of each user simultaneously. This multi-user algorithm is suitable for CDMA-type applications, where each user has a distinct PN-code with good auto- and cross-correlation properties. We show that for spreading gain of 31, the presence of an interpolator enables us to reduce the oversampling factor from 4 to 2 samples per chip. Thus, the requirements of the A/D converter are relaxed without sacrificing system performance. Furthermore, we show that the proposed scheme meets the requirements of multi-user interference cancellation techniques for residual worst-case timing errors, i.e., residual timing error $< 0.2 T_c$, as reported in [200]. Finally, the thesis recommends a similar multi-user structure for narrowband TDMA-type system, which is based on bank of DLLs with whitening pre-filters at the front end of each branch.

ACKNOWLEDGEMENTS

I would like to express my gratitude to my advisor, Dr. Jeffrey Reed and my committee members, Dr. Brian D. Woerner and Dr. Robert J. Boyle for carefully reviewing my thesis and providing valuable suggestions. I would like to especially thank Dr. Boyle and Dr. Reed for giving direction to my research and shaping my thesis.

I would like to also thank fellow students working in MPRG who have made my three semesters of stay at MPRG a great learning experience in every aspect. My research partner, James Hicks, has been the greatest contributor in my achievements at MPRG. He has been very generous in sharing his vast technical knowledge with me. Along with Dr. Boyle and Dr. Reed, he is the main contributor in shaping my research as well as my thesis.

I would also like to thank Ran Gozali and Jay Tsai for their contribution and team work in the time delay estimation research effort. I would also give my gratitude to Kazi Zahid and Bror Peterson for their help and useful suggestions.

Finally, I would like to thank my family and my good friends from Cyprus for their constant encouragement and emotional support during my entire graduate school study.

TABLE OF CONTENTS

CHAPTER 1: INTRODUCTION	1
CHAPTER 2: SYSTEM ANALYSIS	2
2.1 Introduction to the overloaded signal scenario.....	2
2.2 System level analysis	3
2.2.1 Geometry of the interference environment	4
2.2.2 Preliminary System Analysis	5
2.2.3 Link budgets.....	5
2.2.4 System analysis results	8
CHAPTER 3: BACKGROUND	13
3.1 Signal Models	13
3.1.1 Transmitted Signal Model.....	13
3.1.2 Mobile Radio Channel Model.....	16
3.1.3 Received Signal Model.....	18
3.2 Introduction to the Signal Extraction Techniques.....	20
3.2.1 Analogy between Linear Array Processing and Temporal Equalization.....	20
3.2.2 Common adaptation techniques.....	21
3.2.3 MIMO filtering vs. MISO filtering.....	25
3.2.4 Non-linear Processing.....	26
CHAPTER 4: SURVEY OF NARROWBAND SIGNAL EXTRACTION ALGORITHMS 31	
4.1 Single-channel Signal Extraction Algorithms.....	31
4.1.1 Interference rejection algorithms	32
4.1.2 Joint detection and estimation algorithms.....	37
4.2 Multi-channel Signal Extraction Algorithms.....	39
4.2.1 Interference Rejection Techniques.....	40
4.2.2 Joint Detection Techniques	52
4.3 SUMMARY	54
CHAPTER 5: SIGNAL EXTRACTION ALGORITHMS	55
5.1 Multi-user Decision Feedback Equalizer (MU-DFE).....	55
5.1.1 Introduction.....	55

5.1.2	Channel and Signal Models	56
5.1.3	MIMO Feedforward Filter	57
5.1.4	MIMO Feedback Filter	58
5.1.5	Design of the filter coefficients.....	59
5.1.6	Simulation results.....	60
5.1.7	Effect of changing the filter lengths	62
5.1.8	Angular spacing of the users	62
5.1.9	Computational complexity.....	64
5.2	ILSP and ILSE	65
5.2.1	Introduction.....	65
5.2.2	System model.....	65
5.2.3	ILSE and ILSP Algorithms	66
5.2.4	Analytical probability of error	67
5.2.5	Simulation scenarios	68
5.2.6	Apriori known channel.....	68
5.2.7	Training-based Channel Estimation.....	68
5.2.8	Blind channel estimation.....	69
5.3	Summary.....	77

CHAPTER 6: MULTI-USER TIME DELAY ESTIMATION AND SYNCHRONIZATION
79

6.1	Introduction.....	79
6.2	Analysis of multi-user delay estimation problem.....	82
6.2.1	Discrete equivalent channel model	83
6.2.2	maximum likelihood cost function	85
6.2.3	analysis results	86
6.3	Data-aided Single-user delay estimation algorithm	91
6.3.1	Delay Locked Loop (DLL).....	92
6.3.2	Proposed scheme.....	93
6.3.3	Simulation results.....	100
6.3.4	summary of DLL results	102
6.4	Summary of the multi-user time delay estimation research effort	105
6.5	Interpolation based DA-Timing recovery scheme for multi-user cdma receivers	
	108	
6.5.1	Multi-user DLL Simulation Architecture	108
6.5.2	Multi-user DLL Simulation results	109

CHAPTER 7: CONCLUSIONS AND FUTURE WORK.....113

APPENDIX A: PHYSICAL ENVIRONMENT CALCULATIONS.....	116
A.1 Spherical Earth Model	116
A.2 Depression angles	117
A.3 Angular spacing between two co-channel cells	118
A.4 Viewable Area and maximum number of co-channel cells	119
APPENDIX B: LINK BUDGET CALCULATIONS.....	121
B.1 Link Budgets	121
B.1.1 Received power.....	121
B.1.2 Antenna array gain.....	121
B.1.3 Signal to Noise ratio.....	121
B.1.4 Two-ray model Geometry.....	122
APPENDIX C: DERIVATION OF DOPPLER SHIFT AND RATE-DOPPLER.....	126
C.1 Doppler Shift	126
C.2 Race-track loitering pattern.	128
C.2.1 Circular Loitering Pattern	131
APPENDIX D: CIRCULAR ANTENNA ARRAY	133
APPENDIX E: BIBLIOGRAPHY	135

TABLE OF FIGURES

Figure 2.1: “Base station in the sky system” offered by SkyStation International.....	3
Figure 2.2: A typical overloaded co-channel interference environment experienced by an airborne cellular repeater / airborne base-station.	4
Figure 2.3: Aerial view of the interference environment. The region of interest includes the desired user plus all the cochannel interferers. This region of interest is defined by the angle, θ , which can range between 0° (a rather uninteresting case) and 180° . The actual value of θ will depend on the specific nature of the application. However, in our analysis we consider the whole annulus ($0 < \theta \leq 360^\circ$) as a potential source of interferers.	5
Figure 2.4: Two-ray propagation model geometry. Transmitting mobile signals reach the receiver at the ACN through two paths: Direct LOS path and the ground reflected path.	6
Figure 2.5: A snapshot of the interference environment. Repeater flying at an altitude of 45,000ft has a view of a total of 400 co-channel uniformly distributed cells. The desired user has an elevation angle of 7°	9
Figure 2.6: Pathloss variation with continuous distance from the repeater. Free-space pathloss curve increases monotonically with distance. However, Two-ray pathloss curve has several ripples. For certain distance ranges, Two-ray pathloss is constructive (less than the Free Space pathloss). As we approach the horizon, Two-ray pathloss shoots up and becomes highly destructive.	10
Figure 2.7: Comparison of the SNRs per element for each user before beamforming. At distances where the Two-ray pathloss is destructive e.g. towards the horizon, the SNR of the users become insignificant, e.g. SNR < 0 dB. Two-ray model produces a more favorable interference scenario, i.e. there are 144 CCIs with SNRs < 7 dB whereas in the free-space model all the CCIs have SNRs > 7 dB. In the 2-Ray Model, we see that approximately 84 CCIs have negative SNRs and therefore can be treated as additive noise rather than interference.....	10
Figure 2.8: Comparison of the sorted SNRs per element for each CCI before beamforming. Two-ray model results in a scenario where a collection of CCIs has almost negligible power levels, i.e. SNR < 0 dB. The average SNR of all 399 CCIs is 7.9567dB for Two-ray model whereas that for the free-space model is 11.021dB.	12
Figure 2.9: SINR plots for both propagation models. Suppose that the ACN employs a processor that is a concatenated version of a beamformer followed by a joint detector. The Two-ray model needs less number of CCI to be jointly detected in order to achieve a reasonable SINR using linear beamforming.	12
Figure 3.1: Geometry of an arbitrary antenna array.....	17
Figure 3.2: Linear beamformer for single user interference rejection. Complex antenna weights, \mathbf{w} , are updated by using an adaptive algorithm. The beamformer output is a linear combination of the received signal with the complex weights.	21
Figure 3.3: Linear equalizer using an adaptive algorithm to adapt the complex taps, \mathbf{w}	21
Figure 3.4: MIMO Beamformer. Multi-user linear beamformer is a multiple input multiple output linear system where each user is beamformed and demodulated simultaneously.	26
Figure 3.5: FIR digital equivalent channel model: binary BPSK symbols $\in \{-1,1\}$ are shifted into a shift register. The current output is a linear combination of the current and previous symbols.	28

Figure 3.6: Full trellis structure. BPSK symbols pass through a frequency-selective multipath channel (modeled as FIR filter) with 3 symbols of ISI (i.e., $L = 3$).....	29
Figure 3.7: Zooming in the transition at the k^{th} stage. Equation for calculating the error metric for the $i \rightarrow j$ transition is also given here.....	30
Figure 4.1: A breakdown of the single-channel signal extraction algorithms	32
Figure 4.2: Linear Time-Dependent Adaptive Filter.....	34
Figure 4.3: Application of a DFE to signal extraction. Both feedforward and feedback filters are realized as tapped delay lines. The feedforward filter acts as an interference canceller whereas the feedback filter cancels the ISI for the desired user. Generally, the filter weights are updated using either LMS or RLS algorithms.....	35
Figure 4.4: The signal capture problem: CMA captures the interfering signal, $s_i(t)$ instead of the desired signal, $s_d(t)$	36
Figure 4.5: Block diagram of the ICE joint detector. The ICE uses a reduced state ML sequence estimator, RSSE, by accounting for ISI in the error metric of the Viterbi Algorithm. The channel is estimated from a set of training sequences with the RLS algorithm, and tracked with a decision feedback equalizer.....	38
Figure 4.6: Two-Stage JMAPSD Algorithm	38
Figure 4.7: Chart showing the breakdown of the multi-channel signal extraction algorithms.....	39
Figure 4.8: Linear ST-MMSE beamformer is concatenated with a nonlinear ST-MLSE processor. The linear beamformer attempts to cancel the interference whereas the following ST-MLSE processor gets rid of the ISI.....	43
Figure 4.9: Application of DOA estimation to beamforming. The DOA estimator estimates the array steering vector of each incident signal waveform. The estimated DOAs are then used by the following beamformer or another type of signal canceller to extract the desired waveform.....	46
Figure 4.10: Multi-Target LS-CMA adaptive array. M is the number of antenna elements and it is usually equal to the number of ports, i.e. $M=P$. P different beamformer weights are adapted independently by LS-CMA technique. GSO orthogonalizes the weight vectors so that each port corresponds to a unique weight vector. Sorting procedure relates the port outputs to each user's signal. If number of users, D , is larger than the number of elements (or ports), then one output port may contain the signals of several users.....	49
Figure 4.11: VESPA creates a copy of the main real array and forms a virtual array of M sensors displaced in space with a known displacement vector. Only one pair of sensors forms a doublet rather than a full-copy of the array (this is done in ESPRIT algorithm). This results in two subarrays: one with M real sensors the other with M virtual elements. Due to the overlap of one virtual and one real element (forms the doublet), the total aperture consists of $2M - 1$ sensors.....	52
Figure 4.12: Multi-user receiver employing an M antenna array. Transmitted symbols of all users are separated and demodulated jointly using Joint-MAP (JMAP) algorithm. Channel estimates are obtained through the use of training sequences or pilot symbols (for CDMA type systems).....	53
Figure 5.1: Multi-user detector employing a multiple input multiple output (MIMO) Decision Feedback Equalizer (DFE). The MIMO feedforward filter acts as a beamformer/ equalizer. Symbol decision device is a hard limiter whose output (hard limited symbol estimates for the interference) is fed back using a MIMO feedback filter. The MU-DFE incorporates a	

decision delay denoted by l in such a way that hard symbol estimates of k^{th} symbol of each user are made at the end of the $(k+l)^{\text{th}}$ interval.	57
Figure 5.2: Visualizing the MIMO feedforward filter. FF filter has $ns+1$ taps and each tap consists of a $d \times m$ coefficient matrices	58
Figure 5.3: Visualizing the MIMO feedforward filter. The l^{th} coefficient matrix, \mathbf{S}_l acts as a bank of optimal SINR beamformers for the $(k-l)^{\text{th}}$ symbol of each user. The rest of the coefficient matrices are approximately zeros.....	58
Figure 5.4: Visualizing the feedback filter. FB filter has $nq+1$ taps and each tap consists of $d \times d$ coefficient matrices.....	59
Figure 5.5: Performance of MU-DFE using an 8-element circular array of radius = 0.25λ . The array geometry is kept constant while the number of users impinging on it is increased from 1 to 8. The users are spaced equally with a spacing of 45° . As the number of users increases, the performance of the algorithm decreases. For this simulation, we used $L = 1$, $ns = 4$, $l = 3$	61
Figure 5.6: Simulation results for the critically loaded case. The user angles are equally spaced from 0° to 360° . Users are assumed to have equal powers, and channel is assumed to be 2-tap stationary multipath channel ($L = 1$) with scatterers impinging on the antenna array from the same direction as the LOS signals.	61
Figure 5.7: The effect of feedback filter on the performance of MU-DFE in a multipath channel. Four equal spaced, equal power QPSK users impinge on a 4-element circular array. The non-linear processor, MU-DFE with feedback, is robust to the increasing channel length, $L+1$. However, the performance of the linear ST-filter, MU-DFE without feedback, decreases with increasing channel length. Non-linear feedback corrects for the severe multipath distortion. For both cases, the feedforward filter was chosen to be of length $ns = 4$. For the non-linear case, the decision delay was chosen to be $l = 3$	63
Figure 5.8: 2 equal power QPSK users impinge on a 3-element circular array. Performance degrades significantly as the users are closely spaced.	64
Figure 5.9: Computational complexity of the MU-DFE per snapshot per iteration. The complexity is polynomial in m and d . The complexity is also affected by the FF filter length, ns and channel order, L	65
Figure 5.10: Block diagram of the two iterative detectors employing an overloaded array. Symbol synchronous Finite Alphabet user symbols can be extracted by estimating the channel and estimating the symbol matrix iteratively. Symbol estimation can be done either by using the linear ILSP or non-linear ILSE algorithms. The relative complexities in terms of <i>flops</i> are denoted in the diagram.	66
Figure 5.11: Example of AOA randomization for blind ILSE and blind ILSP	70
Figure 5.12: Port shuffle problem in blind joint detection techniques.	70
Figure 5.13: Performance curves for ILSP with (1) perfectly known channel, (2) training based channel estimation and (3) blind channel estimation. The array is fully loaded. The users are equally spaced in AOA. The performance degrades with the increasing number of users and antenna elements due to smaller angular spacing of the users. The performance for all three cases are very similar.	72
Figure 5.14: (a) Three equal-power synchronous users impinge on a three-element array. ILSE can demodulate closely spaced users whereas ILSP fails drastically. (b) Performance of ILSE in demodulating 3 closely spaced users. The AOA of user 2 is closest to the other two	

signals and therefore has the highest SER whereas user 3 has the lowest SER since it is well separated from the others.	73
Figure 5.15: The users are equally spaced over 360° (except for the case $m = 3, d = 6$ where the users are equally spaced over 180°). Single user (AOA = 60°) performance is also illustrated as a baseline. The figure shows that ILSE performs well for the cases $d \neq m^2$..	74
Figure 5.16: <i>Signal crowding</i> . Assume a zero-phase unity gain channel. 5 baud-synchronized BPSK users impinge on a 2-element array. Signal points at array output gets closer as more users impinge on the array, i.e. harder to draw decision boundaries. Un-equal powers may help reduce the crowding, e.g. for user 1. Signal crowding is worse for closely spaced users.	74
Figure 5.17: Signal ambiguity in joint detection of equal-power synchronous users. Signal ambiguity is most prevalent whenever the user signals are perfectly symbol-synchronous and have equal powers. In that case, the minimum Euclidean distance, $d_{i,min}$ among the symbols after mapping on the array response becomes zero. This results in an ambiguous point on the signal space. Thus the symbol-by-symbol joint detector cannot distinguish between the distinct transmitted user symbols.....	75
Figure 5.18: Average SER curves for the four closely spaced unequal-power and equal-power QPSK users impinging on a two element array ILSE is able to separate all four unequal-power closely spaced users whereas it fails when the users have equal powers.	76
Figure 5.19: Comparison of ILSE (1) blind channel estimation, (2) training-based channel estimation, (3) known channel. Equal-power QPSK users impinge on a two-element antenna. Angle-of-arrival of the users are: $d = 3, [0^\circ, 10^\circ, 20^\circ]$; $d = 4, [0^\circ, 10^\circ, 20^\circ, 30^\circ]$; $d = 5, [0^\circ, 10^\circ, 20^\circ, 30^\circ, 40^\circ]$. Performance of ILSE in all three cases is very similar for the same number of user environment. Performance degrades gracefully as the number of users increase.....	77
Figure 6.1: Illustration of 2 asynchronous BPSK user sequences	80
Figure 6.2: MLSE used as a joint detector. In this example, detection of 2 asynchronous BPSK users requires a joint detection trellis due to the 2-symbols of ISI (time misalignment as shown in figure 6.1).	81
Figure 6.3: Proposed PSP based channel estimation algorithm that incorporates time-delay estimation algorithm. Each user's time delay as well as symbol sequence are estimated at each state of the PSP trellis. These estimates are updated in the following stages until the trellis is terminated.....	81
Figure 6.4: Conceptual data-aided time delay estimation algorithm to be used within the PSP trellis.....	82
Figure 6.5: Roadmap of Multi-user time delay estimation.....	83
Figure 6.6: Discrete equivalent channel model used in the analysis.	84
Figure 6.7: Joint multi-user delay estimation error surface. (a) Delays are not separable for short data blocks, e.g. $N_{pkt} = 10$ symbols. τ_1 cannot be reliably estimated given that τ_2 is perfectly known, and vice versa. This is depicted in the two checkerboard plots. (b) Delays become separable for longer data blocks, e.g. $N_{pkt} = 30$ symbols.	87
Figure 6.8: Results for estimating the delay of SOI given that the delays of CCI are perfectly known. Lower bounds on joint delay estimation for different block sizes and different number of users. Delay estimation error has a Gaussian distribution with zero mean, therefore standard deviation of the error estimate in T_{sym} is plotted against SNR.	88

Figure 6.9: Single user delay estimation. Case (1): ignore the interference and treat it as AWGN. Case(2): account for the interference in the ML function formulation.	89
Figure 6.10: Comparison of case (1) and case (2) results with lower bound results.	90
Figure 6.11: Cholesky factor of Φ_m^{-1} is a block Toeplitz matrix \mathbf{F} . This matrix can be used as a linear pre-filter for interference rejection (noise whitening).	91
Figure 6.12: Possible multi-user time delay estimator structure. Received signal (SOI + CCI+AWGN) is first pre-filtered with an adaptive linear filter, \mathbf{F} . Then SOI's time delay is estimated by a low-complexity data-aided time delay estimation algorithm. The coefficients of the adaptive filter can be updated using either LMS or RLS algorithms.	91
Figure 6.13: Block Diagram of General DLL architecture	93
Figure 6.14: Proposed DLL block diagram. m_k : basepoint sample out of Q_o samples per symbol, μ_k : fractional timing offset	94
Figure 6.15: Linear Interpolation used in the synchronization scheme	95
Figure 6.16: Cubic Interpolator based on Farrow structure	95
Figure 6.17: Sliding correlator output is symmetric at ideal sampling. Early-late detector produces zero output due to perfect match.	96
Figure 6.18: SINR Estimator Criteria to determine the threshold for the “freeze” loop mechanism. Peak/Second Peak criterion gives a more distinct threshold than the Correlator Peak Error criterion.	98
Figure 6.19: μ_k - searcher output. $\mu_{k,res} = 0.2$ of a sample. Quantized μ_k hypothesis	99
Figure 6.20: S-curves for TED_1 and TED_2 . TED_1 has a lower range of operation due to the ambiguous regions in mapping $f(\tau_{du})$ to a estimate of τ_{du}	100
Figure 6.21: MSE of TED output for $\tau = 0.4$ samples. TED output MSE decreases with increasing SNR. Cubic interpolator with $Q_o = 2$ samples per symbol. Completely compensates for 0.4 fractional delay. Error floor for no interpolator case can be seen in the zoomed version of the figure.	103
Figure 6.22: Correlator Peak Error MSE for $\tau = 0.4$ samples. For $SNR > -10dB$, $MSE < 0.1$ (for all 6 cases). Peak is close to 1. Cubic interpolator gives the lowest MSE.	104
Figure 6.23: MSE of TED output for delay of -0.48 samples. Interpolator performance is limited by the ' $\mu_{k,res}$ '. Cubic interpolator still gives the best 'fine tuning'	104
Figure 6.24: Transient behavior of the DLL. For $SNR \geq -5dB$ & $NOB > 7$ blocks: $ \tau - \tau_{est} < 0.5$ samples.....	105
Figure 6.25: Possible multi-user delay estimation algorithm structure 1. Parallel bank of Du DLL structures that simultaneously estimates the time delays of Du user signals. This scheme is expected to work well given that the known symbol sequences of Du users have good correlation properties.	107
Figure 6.26: Possible multi-user delay estimation algorithm structure 2. Parallel bank of Du DLL + Du adaptive pre-filter structure. Adaptive filter suppresses the interference at each bank and “clean” signal is then operated by the DLL to estimate the delay.	108
Figure 6.27: Proposed Multi-user Synchronization Scheme for CDMA receivers.	109
Figure 6.28: Comparison of 4 different DLL structures in multi-user synchronization scheme. Averaged timing error in T_c (users = 6, spreading gain = 31, $\tau_{du} = 0.4 T_s$).....	110
Figure 6.29: The effect of Multiple Access Interference (MAI) on the performance of the proposed multi-user DLL scheme for CDMA systems.	111

Figure 6.30: Simultaneous time delay estimation of 6 users' timing ($\tau = [-1, -0.6, -0.2, 0.2, 0.6, 1]$
 T_c) with the selected configuration of $Q_o = 2$ with a cubic interpolator 112

CHAPTER 1: INTRODUCTION

In today's Time Division Multiple Access (TDMA) cellular systems, co-channel interference is the major impairment for the system capacity and link quality. The interference environment affects the optimal design of the receiver. In terrestrial cellular systems, careful site planning coupled with multiple sectorized antennas located at the base stations can successfully reduce the number of simultaneous Co-Channel Interferers (CCIs). However, for airborne cellular communication applications, such as *airborne repeaters*, the receiver is subject to many CCIs mainly due to its high altitude and wide range of view. One could easily expect the number of high-power incoming signals to exceed the repeater's array size. This results in an *overloaded environment*.

The goal of an airborne receiver is to extract Signals of Interest (SOIs) out of such harsh interference environment. This necessitates the use of so-called *overloaded array processing* algorithms. Overloaded array processing is a much bigger challenge for narrowband TDMA type signals than for CDMA type signals. In CDMA, one can exploit the spreading gain as well as the excess bandwidth to extract more signals than antenna elements. However, narrowband TDMA systems do not have this freedom.

Natural question may arise: why is overloaded array processing important, and what are the benefits of using sophisticated signal processing algorithms? In the context of airborne communication systems, the need for cost-effective RF front end as well as the space limitations on the surface of the aircraft are the major driving forces for pursuing overloaded array processing. The processors are getting faster and cheaper and therefore, powerful signal processing techniques could enable the recovery of many user signals with a few antenna elements thus greatly reducing the implementation costs.

There are two fundamental approaches for extracting desired signals out of an interference environment: interference rejection and joint detection (or multi-user detection). In the former, the processor treats interference as background noise (either colored or white) and tries to strip out the desired user signals by suppressing the interference. On the other hand, a joint detection receiver tries to demodulate all the user (desired plus interference) signals simultaneously. Past

signal processing research has shown that joint detection outperforms interference rejection even when interference is not of direct interest. However, this performance advantage comes with the cost of higher computational complexity. This thesis provides the reader insight into the algorithm level research on both interference rejection and joint detection techniques for narrowband signals.

Chapter 2 of this thesis discusses the airborne repeater system level interference environment analysis. This analysis shows a ‘hostile’ interference environment, which necessitates the use of sophisticated signal processing algorithms to extract desired user signals. Chapter 3 gives a brief overview of basic signal processing concepts that are used in the signal extraction literature. Chapter 4 consists of an extensive literature survey of narrowband signal extraction algorithms found in literature. Chapter 5 analyzes relative merits of three different joint detection techniques that were perceived as ‘promising’ approaches for overloaded array processing. All these algorithms are simulated assuming synchronous users as well as benign channel conditions, i.e., AWGN channel with no multipath. In chapter 6, we discuss the multi-user time delay estimation problem, which must be addressed when the user signals impinging on the receiver array are not time-aligned. Here, we first show the simulation results for a data-aided timing delay estimation and synchronization system for a single user case. We then extend the single user delay estimation / synchronization structure to multi-user case. We also propose a second multi-user delay estimation structure for future research. Finally, chapter 7 concludes the thesis with a summary and some recommendations for future work.

CHAPTER 2: SYSTEM ANALYSIS

2.1 INTRODUCTION TO THE OVERLOADED SIGNAL SCENARIO

The wireless industry, both commercial and military, has developed an interest in airborne applications for wireless systems. An Airborne Communications Node (ACN) is an airborne platform that provides a communication link to the desired mobile users by loitering at a high altitude. ACN can be used as a cellular base-station or as a cell-extender repeater. An airborne cell-extender repeater can be effective in extending the coverage in low-density regions. It provides ground-to-earth and earth-to-ground communication links between the mobile users in a highly rural or highly underdeveloped areas and far-off terrestrial base-stations. One commercial example of an airborne repeater system is the “base station in the sky system” offered by SkyStation International, which is expected to be deployed over every major city of the world by the year 2002. This repeater system employs an aerostat that hovers at an altitude of nearly 70,000 feet. The platform is equipped with a telecommunications payload providing high speed, high capacity cellular services and broadband services, such as T1/E1 services, to an area of approximately 19,000 square kilometers (7,500 square miles) [44]. Coverage can also be extended into rural areas outside this zone. This system is anticipated to provide an extensive cellular capacity increase in the deployment areas. Figure 2.1 depicts this airborne communication system. Airborne communication platforms, which fly in a certain loitering pattern at a specified altitude, offer a number of advantages that include significant range extension and reduction in handoffs for highly mobile users. These advantages are a direct consequence of the large field of view obtained from high loitering altitudes. Because of the large field of view, airborne communication nodes are susceptible to interference from a large number of sources within the field of view. Furthermore, since these sources have Line of Sight (LOS) with the repeater, their interference is significant. To complicate the matter, most airborne platforms are limited in size, which restricts that number of antennas and the array size that the platform can support. It is likely that the number of high-power, i.e, power levels well beyond the noise level, interfering sources exceeds the array size. We call such an interference environment the *overloaded array* environment. This environment is depicted in figure 2.2. The

receiver in the ACN has the great challenge of being able to extract the desired user signals from the hostile interference environment.



Figure 2.1: “Base station in the sky system” offered by SkyStation International

In the following sections, we will show a detailed system analysis of the interference environment, Doppler effects induced by the airborne node, link budget analysis using one-ray and two-ray propagation models. Finally, we will discuss the implications of the physical environment on signal processing algorithms.

2.2 SYSTEM LEVEL ANALYSIS

In this section, we first characterize the geometry of the interference environment for an airborne repeater operating in a TDMA/FDMA type cellular environment. This is accomplished by assuming a uniform hexagonal cell tessellation superimposed on a flat earth. This is a valid assumption when we consider the altitude of the airborne platform (on the order of several miles above the earth surface) compared with the earth radius (3963.35 miles). In our analysis, we

focus on the physical environment as perceived by the airborne repeater system at a particular point in time. This analysis provides us with a rough approximation of the number of CCI cells within the airborne node's field of view. Secondly, we analyze the effects of Doppler shift induced by the ACN and its implications on signal processing algorithms. Finally, we provide a link budget analysis using a one-ray and a two-ray propagation models.

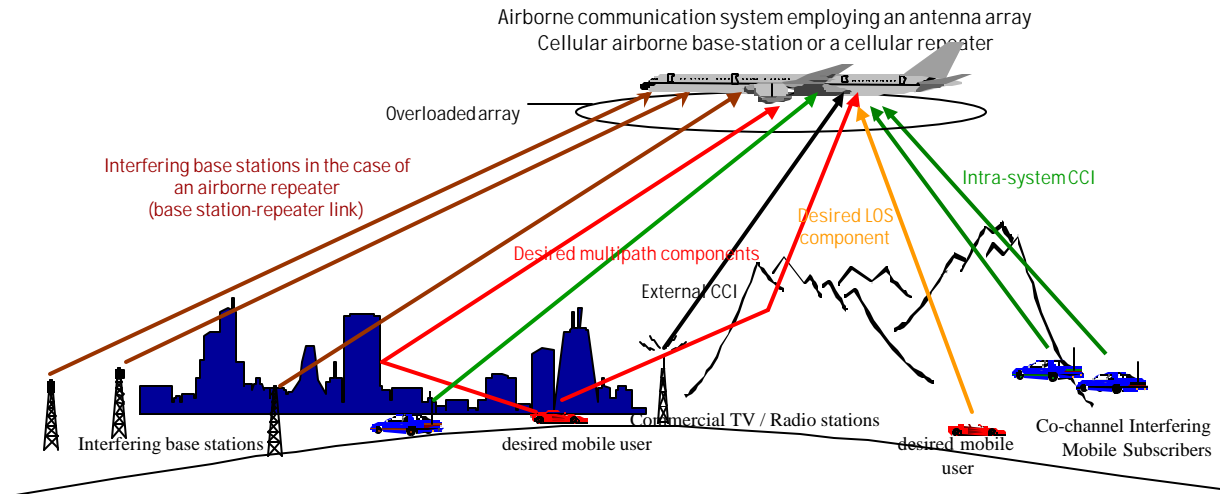


Figure 2.2: A typical overloaded co-channel interference environment experienced by an airborne cellular repeater / airborne base-station.

2.2.1 GEOMETRY OF THE INTERFERENCE ENVIRONMENT

An airborne repeater loitering in the sky at a specified altitude overlooks a vast area covered with uniformly tessellated cell sites. A simplified aerial view of the repeater looks like an *annulus* superimposed on a horizontal plane, which is depicted in figure 2.3. The repeater can experience interference from any part of the annulus. The inner radius, d_{min} , is determined by the distance associated with the largest allowable elevation angle of the mobile users. Here, we are assuming that the antenna array mounted on the repeater has a certain downward tilt that nulls out any user signal impinging on the array from an elevation angle exceeding a specific value. In our system analysis, we set the maximum elevation angle to 10° . The outer radius, d_{max} , is defined as the horizon distance. The *region of interest* is the wedge of the annulus that contains the desired user. For simplicity sake, we assume only a single desired user in the interference environment.

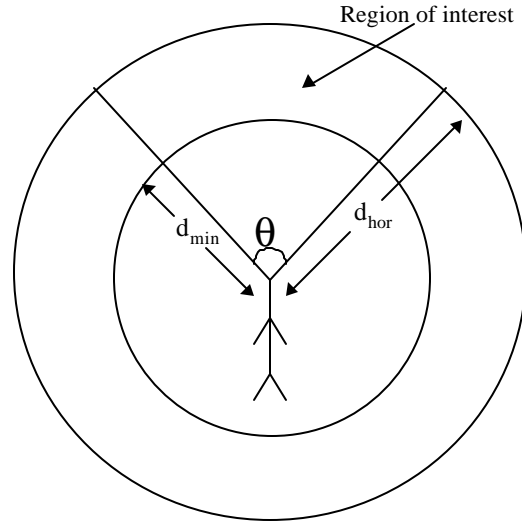


Figure 2.3: Aerial view of the interference environment. The region of interest includes the desired user plus all the cochannel interferers. This region of interest is defined by the angle, θ , which can range between 0° (a rather uninteresting case) and 180° . The actual value of θ will depend on the specific nature of the application. However, in our analysis we consider the whole annulus ($0 < \theta \leq 360^\circ$) as a potential source of interferers.

2.2.2 PRELIMINARY SYSTEM ANALYSIS

Using the above model, we conducted an analysis in order to establish scenario driven parameters such as area in view, area of interest, and the total number of co-channels cells for a given cell radius and frequency reuse factor. Details of these preliminary system analysis can be found in Appendix A. Table 2.1 shows results for the case where the sector angle and the maximum elevation angle are taken as 360° and 10° , respectively.

Table 2-1: Worst-case co-channel environment calculations for the case where the frequency reuse factor is 7 and a cell radius is 6.21 miles.

Altitude range(ft)	d_{min} range (miles)	d_{max} range (miles)	Max. area range (miles ²)	Max. number of co-channel cells
30,000 - 40,000	32 - 43	212 - 245	139,000-184,000	197-261

As expected, the number of cochannel cells is inversely proportional to the reuse factor, cell radius and repeater altitude.

2.2.3 LINK BUDGETS

In this section, we analyze the interference environment assuming a one-ray propagation model as well as a more complicated two-ray propagation model. The one-ray model assumes a single LOS path between the mobile units and the airborne repeater. This model results in a very

simple link budget analysis. However, one-ray model may not be a very accurate realization of the real propagation channel since it neglects the ground reflections due to the earth's surface. A more realistic model is the two-ray model, which considers both the direct path and a ground reflected propagation path between the transmitter and the receiver. Figure 2.4 depicts the Two-ray model geometry.

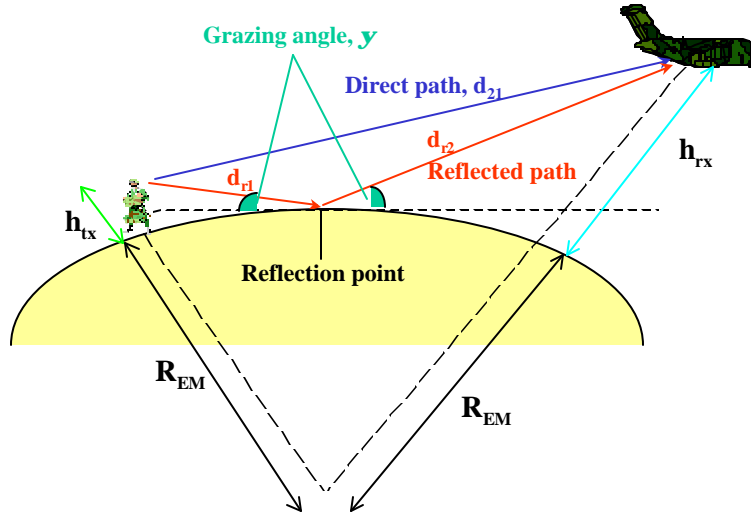


Figure 2.4: Two-ray propagation model geometry. Transmitting mobile signals reach the receiver at the ACN through two paths: Direct LOS path and the ground reflected path.

Since earth is neither a perfect conductor nor a perfect dielectric, the reflection coefficients (both horizontally and vertically polarized) depend on ground-constants, namely the conductivity, σ , and dielectric constant, ϵ . The reflection coefficients along the horizontal and vertical polarization are denoted by Γ_h and Γ_v , respectively. These coefficients are given by the following formulas [50]:

$$\Gamma_h = \frac{\sin y - \sqrt{(e/e_0 - j s / w e_0) - \cos^2 y}}{\sin y + \sqrt{(e/e_0 - j s / w e_0) - \cos^2 y}} \quad (2.1)$$

$$\Gamma_v = \frac{(e_r - j s / w e_0) \sin y - \sqrt{(e_r - j s / w e_0) - \cos^2 y}}{(e_r - j s / w e_0) \sin y + \sqrt{(e_r - j s / w e_0) - \cos^2 y}} \quad (2.2)$$

where ω is the angular frequency of transmission, θ is the angle of incidence and ϵ_0 is the dielectric constant of free space.

Equations (2.1) and (2.2) assume a smooth, spherical earth. However, in practice this is not a very accurate assumption. Therefore, the roughness of the earth surface is also included in the Two-Ray model. When a radio wave impinges on a rough surface, the reflected energy is spread out in all directions due to scattering. This effect can be accurately modeled by modifying the reflection coefficients with a scattering factor, called *terrain standard deviation*, σ_h . Boithias [51] developed the following formula to account for the scattering loss due to the terrain effects:

$$r_s = \exp \left[-8 \left(\frac{ps_h \sin \theta}{l} \right)^2 \right] I_0 \left[8 \left(\frac{ps_h \sin \theta}{l} \right)^2 \right] \quad (2.3)$$

where I_0 is the Bessel function of the first kind and zero order.

The modified reflection coefficient is then given by [51] as

$$\Gamma_{rough} = r_s \Gamma_{smooth} \quad (2.4)$$

The ground reflection point and the grazing angle are approximated using Newton-Raphson recursion. After the true grazing angle is found, the slant distances d_{21} (slant distance between the two nodes) and d_{rm} (slant distance between the ground reflection point and the m^{th} node) are calculated using simple geometry. Appendix B shows an extensive analysis of these calculations. The two-ray path losses for both vertical and horizontal polarization are then given by

$$PL_{21} = -20 \log_{10} \left(|\mathbf{a}_{21}|^2 \right) \quad (2.5a)$$

where the complex path gain (for either vertical or horizontal polarization) and the path difference are given by:

$$\mathbf{a}_{21} = \left(1 + \Gamma e^{-j2p\Delta_{21}/l} \right) \left(\frac{l}{4pd_{21}} \right) e^{-j2pd_{21}/l} \quad (2.5b)$$

$$\Delta_{21} = (d_{r2} + d_{r1}) - d_{21} \quad (2.5c)$$

2.2.4 SYSTEM ANALYSIS RESULTS

The purpose of this system analysis is to get a rough idea about the interference environment in terms of total number co-channel users, and their relative power levels. The results of this analysis are needed to assess feasible types of processing techniques for signal extraction in overloaded array scenarios. Table 2.2 summarizes the parameters used in this analysis. A user with an elevation angle of 7° is subject to 399 co-channel users within the repeater's field of view. Earth radius is taken to be $4/3$ of the physical earth radius, which is known as the *electromagnetic (EM) earth radius*, i.e. $R_{EM} = 5284.5$ miles. As expected, using the EM earth radius rather than the physical earth radius (3963.35 miles) increases the number of interferers in the aircraft's field of view. Similarly, the number of interferers increases with increasing repeater altitude since the ACN has a wider range of view of the co-channel cells.

Table 2-2: Interference environment parameters

Desired user elevation	Sector angle	Carrier Frequency	Repeater Altitude	Mobile User Height	Cell Radius	Horizon distance
7°	360°	900 MHz	45,000 ft	2 m	6.21 miles	300 miles

The Two-ray model uses several earth constants as given by Table 2.3. Both the transmitter and receiver antennas are assumed to be omnidirectional. The minimum distance is taken to be the distance to the inner radius of the annulus (shown in figure 2.5), which turns out to be 53.705 miles. The max distance is taken to be the horizon distance, approximately 300 miles.

Table 2-3: Two-ray Model Parameters

Transmitter antenna gain	Receiver antenna gain	Transmitter power level	Conductivity of ground, σ	Relative permittivity of ground, ϵ_r	terrain standard deviation, σ_h
0 dB	$10\log(\# \text{ of elements})$	2 W	0.01F/m Fertile soil	15 Fertile soil	2 m

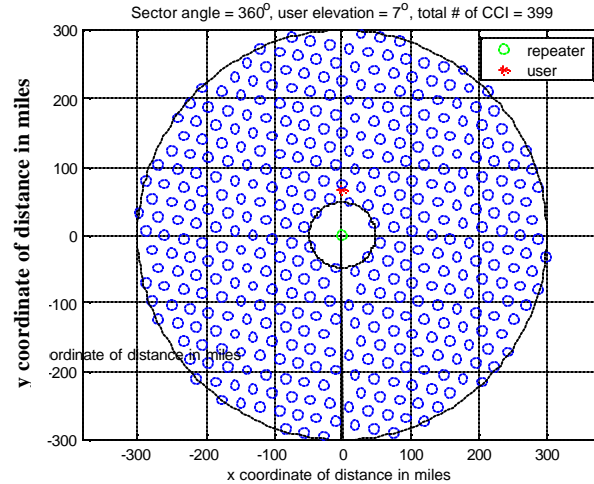


Figure 2.5: A snapshot of the interference environment. Repeater flying at an altitude of 45,000ft has a view of a total of 400 co-channel uniformly distributed cells. The desired user has an elevation angle of 7° .

Figure 2.6 depicts the pathloss variation with continuous distance from the repeater. As expected from the Frii's equation, the Free-space pathloss curve increases monotonically with distance. However, two-ray pathloss curve has several ripples. For certain distance ranges, two-ray pathloss is constructive (less than the Free Space pathloss). As we approach the horizon, two-ray pathloss increases exponentially and becomes highly destructive. This implies that the interfering signals coming from far distances are likely to be highly attenuated. In fact, figure 2.7 shows that at distances where the Two-ray model is destructive e.g. towards the horizon, the SNR of the users become insignificant, e.g. $\text{SNR} < 0$ dB. However, in the Free-space model SNR of the CCIs are significant, e.g. $\text{min SNR}_{\text{CCI}} \approx 7.1$ dB. The two-Ray model results in a more favorable SNR distribution, i.e. the average SNRs of the CCI cells are less than those obtained in the free-space model. For example, at a repeater loitering at an altitude of 45,000 ft can see a total of 399 CCIs. However, according to the link budget analysis using the Two-ray model, 84 of these CCIs have almost negligible power levels. Therefore, these weak CCIs can be treated as additive noise instead of interference.

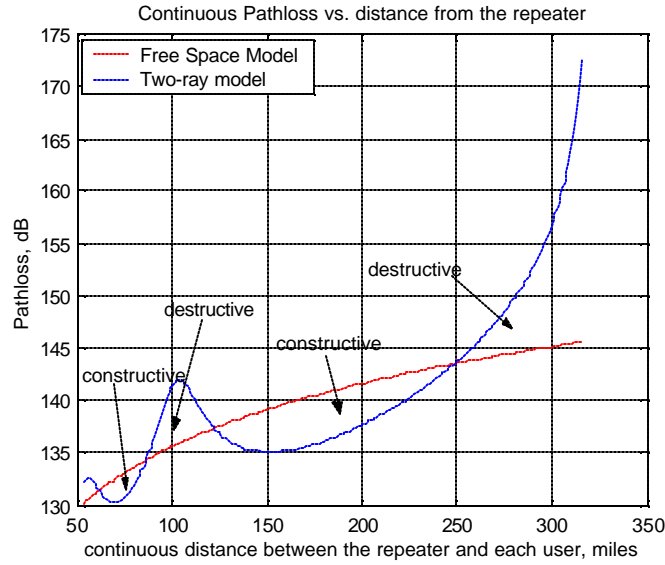


Figure 2.6: Pathloss variation with continuous distance from the repeater. Free-space pathloss curve increases monotonically with distance. However, Two-ray pathloss curve has several ripples. For certain distance ranges, Two-ray pathloss is constructive (less than the Free Space pathloss). As we approach the horizon, Two-ray pathloss shoots up and becomes highly destructive.

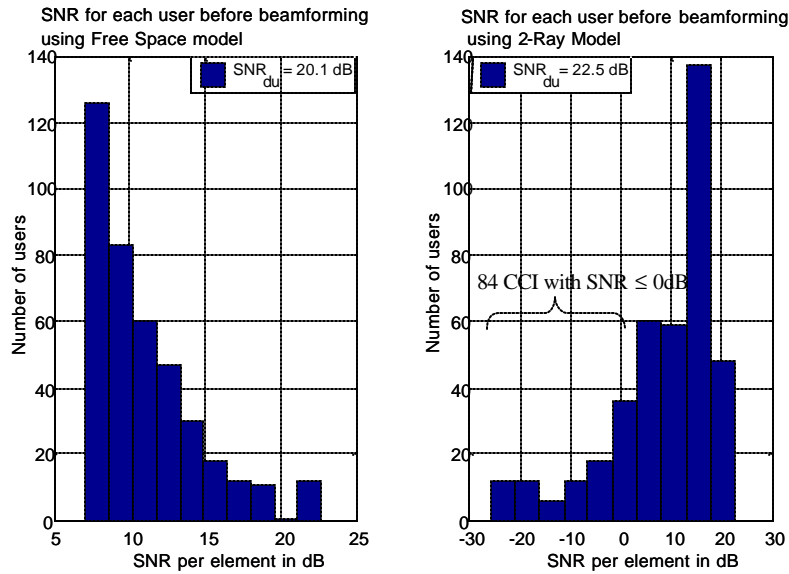


Figure 2.7: Comparison of the SNRs per element for each user before beamforming. At distances where the Two-ray pathloss is destructive e.g. towards the horizon, the SNR of the users become insignificant, e.g. $SNR < 0dB$. Two-ray model produces a more favorable interference scenario, i.e. there are 144 CCIs with SNRs $< 7dB$ whereas in the free-space model all the CCIs have SNRs $> 7dB$. In the 2-Ray Model, we see that approximately 84 CCIs have negative SNRs and therefore can be treated as additive noise rather than interference.

In an attempt to come up with a suitable processor type that would be utilized in this interference environment, we can analyze the effect of an optimum SINR beamformer followed by a joint

detector by employing the Two-ray model in the link budget calculations. We assume that the beamformer has an a priori knowledge of the N_j users out of N users that are perfectly demodulated by the joint-detector. Then the optimum SINR beamformer tries to reject the remaining $N-N_j$ users. The N_j jointly detected users are chosen according to a specific sorting criterion, which is the interfering user SNRs (before beamforming) are sorted in an ascending order as shown in figure 2.8. The reported SINR values in figure 2.9 represent the SINR obtained after forming an optimal SINR beam in the direction of each one of the $N-N_j$ remaining users. Non-uniform step sizes in the graph are due to the different received power levels of the CCI. The SINR plots are concave up because when $N-N_j$ is large, taking one user out of the interference environment does not significantly change the total SINR. However, when N_j is large, a single interfering signal represents a significant portion of the remaining interference power. The maximum SINR is equal to the SNR of the desired user after beamforming, i.e. $\text{SNR}_{\text{du}} = \text{SNR}_{\text{du}}(\text{per element}) + G_{\text{rec}}$ where $G_{\text{rec}} = 10\log_{10}(\text{number of elements})$. For example, for an 8-element array, the maximum SINR for the Two-ray model becomes $\text{SINR} = \text{SNR}_{\text{du}} = 22.5 \text{ dB} + 10\log_{10}(8) \approx 31.56 \text{ dB}$. Figure 2.9 also shows that the Two-ray model results in a more friendly interference environment than the free-space model. Assume our receiver needs a total SINR of 10dB in order to achieve an acceptable error rate. According to figure 2.9, we see that using the free-space model we need to jointly demodulate a total of 384 CCI users and null out the remaining 15 CCI using linear processing. On the other hand, using a Two-ray model we only need to jointly demodulate 337 CCIs and the remaining 62 CCIs can be processed linearly by an optimum SINR beamformer.

Even though the Two-ray model improves the interference environment, the number of co-channel users that needs to be jointly detected is still in the order of hundreds. Therefore, the hostile interference environment still remains to be a major challenge in our signal extraction research effort. The remaining chapters of the thesis will focus on the signal processing aspects of spatial, temporal and spatio-temporal signal extraction algorithms.

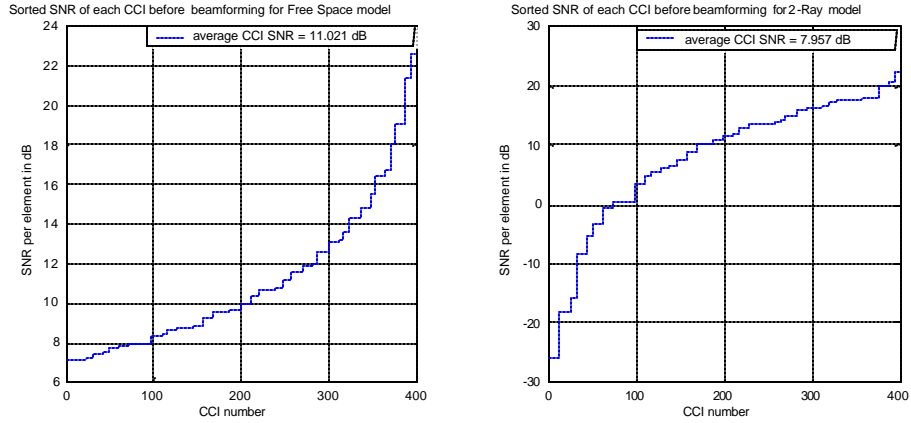


Figure 2.8: Comparison of the sorted SNRs per element for each CCI before beamforming. Two-ray model results in a scenario where a collection of CCIs has almost negligible power levels, i.e. SNR < 0dB. The average SNR of all 399 CCIs is 7.9567dB for Two-ray model whereas that for the free-space model is 11.021dB.

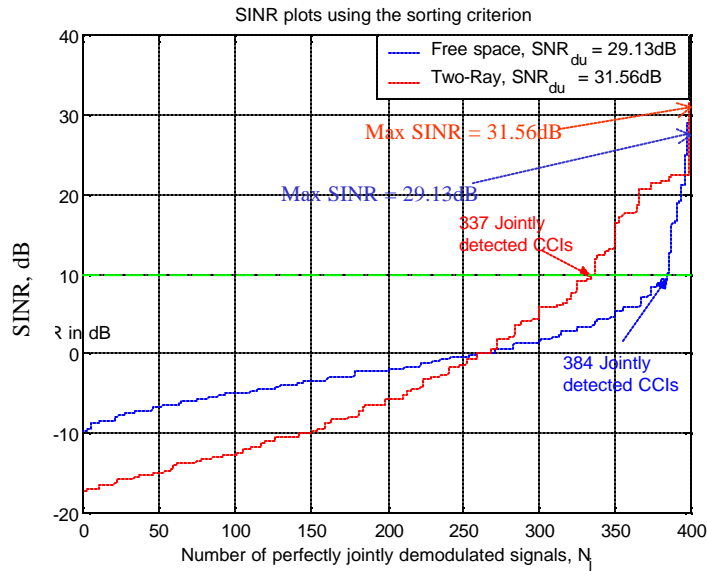


Figure 2.9: SINR plots for both propagation models. Suppose that the ACN employs a processor that is a concatenated version of a beamformer followed by a joint detector. The Two-ray model needs less number of CCI to be jointly detected in order to achieve a reasonable SINR using linear beamforming.

CHAPTER 3: BACKGROUND

3.1 SIGNAL MODELS

In this section, we present models for the transmitted signal, the specular multipath radio channel, and the received signal. The main purpose is to give the reader an overview of the generic signal models used in the different signal extraction techniques, which is the topic of Chapter 4.

3.1.1 TRANSMITTED SIGNAL MODEL

In this section we present models for the signals that are typically used in cellular and PCS applications. Accordingly, we will limit our discussion to Frequency Modulated (FM) signals and conventional digital signals. The discussion will focus on the structure and property of each modulation that one can exploit for signal extraction purposes.

In general, the transmitted signal may be expressed as follows

$$s(t) = \text{Re} \left\{ x(t) e^{j2\pi f_c t} \right\} \quad (3.1)$$

where f_c is the carrier frequency and $x(t)$ is the baseband representation of the transmitted signal that also contains the information to be communicated. The baseband signal, $x(t)$, is modeled as follows

$$x(t) = A(t) e^{j\Phi(t)} \quad (3.2)$$

where $A(t)$ is the amplitude signal and $\Phi(t)$ is the phase signal. Communications signals transmit information by modulating either or both of these signals.

3.1.1.1 FREQUENCY MODULATED SIGNALS

FM signals transmit information by modulating the phase signal, $\Phi(t)$, as follows:

$$\Phi(t) = 2\pi h \int_{-\infty}^t \Psi(\tau) d\tau \quad (3.3)$$

In (3.3), h is the modulation index and $\Psi(t)$ is the information source. $\Psi(t)$ can be an analog signal, such as a voice grade signal, or a digital signal. The amplitude signal, $A(t)$, is fixed to a constant value. Accordingly, the baseband representation of an FM signal is the following

$$x_{FM}(t) = A \exp \left\{ j 2\pi h \int_{-\infty}^t \Psi(\tau) d\tau \right\} \quad (3.4)$$

Note that the instantaneous frequency of $x_{FM}(t)$ is

$$f_i(t) = \frac{1}{2\pi} \frac{d\Phi(t)}{dt} = h\Psi(t) \quad (3.5)$$

As shown in (3.4), FM signals have two distinctive properties. The most common of these properties is the constant amplitude (or constant modulus) nature of the signal. Significant research has led to a class of signal extraction algorithms, called *Constant Modulus Algorithms (CMA)*, which exploit this property.

The second property is the continuity of the signal phase as shown in (3.3). Sequence estimation via the Viterbi algorithm is a new, innovative technique that exploits the phase continuity property of FM signals for signal extraction purposes [6]. Here, the state of $x_{FM}(t)$ is defined by the second derivative of the instantaneous frequency, and the signal is extracted by searching through a trellis that contains the states of the SOI and the interfering signals, particularly if these interferers are also FM signals or other signals that lend itself to a state-driven structure.

3.1.1.2 DIGITAL COMMUNICATION SIGNALS

The digital communication signals used in mobile wireless applications employ some form of phase modulation technique. These techniques may be partitioned into two groups, namely: Phase Shift Keying (PSK) and Continuous Phase Modulated (CPM). Each of these groups has unique properties that one can exploit for signal extraction purposes PSK signals have the following structure

$$x_{PSK}(t) = \sum_{n=-\infty}^{\infty} s_n g(t - nT_s) \quad (3.6)$$

where T_s is the symbol period, $g(t)$ is a pulse shaping function, and $s_n = e^{j\mathbf{f}_n}$ is a complex valued symbol that is taken from a finite alphabet of size \mathbf{J} . For example, in $\pi/4$ -DQPSK, \mathbf{J} contains 8 possible differential phase values and \mathbf{f}_n can take on any *one* of these values. Since \mathbf{f}_n can take on exactly one of a finite number of values, we say that $x_{PSK}(t)$ has a *Finite Alphabet (FA)* property.

One can exploit this FA property to extract PSK signals from a high interference environment. The optimal extraction algorithm is the Maximum Likelihood Sequence Estimator (MLSE), which performs well provided that the interference environment is known or can be modeled in the form of a state diagram or trellis. The main shortcoming of this approach is the computational complexity commonly associated with traditional sequence estimation techniques. Accordingly, much of the research has focused on near-optimal techniques that involve combinations of *Reduced State Sequence Estimation (RSSE)* [172], equalization or adaptive filtering techniques, and combination of these techniques.

CPM signals have the following structure

$$x_{CPM}(t) = Ae^{j\Phi(t)} \quad (3.7)$$

where

$$\Phi(t) = 2\pi h \int_{-\infty}^t \sum_{n=-\infty}^{\infty} a_n g(\tau - nT_s) d\tau \quad (3.8)$$

In (3.8), T_s is the symbol duration, h is the modulation index, $g(t)$ is a pulse shaping function, and a_n is a value taken from a finite alphabet of values.

GMSK is an example of a CPM waveform that is commonly used in second-generation wireless systems that employ the GSM and PCS-1900 air interface standards. GMSK uses a Gaussian pulse shaping function whose duration exceeds T_s (called *partial response* shaping function). This pulse shaping gives GMSK excellent bandwidth efficiency characteristics, however it also introduces three symbols of ISI. Accordingly, the optimal detector for GMSK in a white noise channel is a sequence estimator, which can be implemented in an 8-state Viterbi algorithm.

Note that like PSK signals, CPM signals have a FA property. Hence, the optimal extraction algorithm in an interference environment is also a Maximum Likelihood Sequence Estimation (MLSE), provided that the interfering signals can be modeled in the form of a state diagram or trellis. However, CPM signals also have a CM property. Therefore, spatially based, temporally based, or space-time CMA algorithms can also be used to extract CPM signals in an interference environment. Further, these CMA algorithms can be combined with MLSE techniques to boost performance. These techniques will be discussed in some detail in Chapter 4.

3.1.1.3 CYCLOSTATIONARY PROPERTIES OF BOTH FM AND DIGITAL COMMUNICATION SIGNALS

In addition to their FA and CM properties, most man-made communication signals exhibit *spectral redundancy* (i.e. nonzero correlation between some frequency-shifted versions of the signal). When multiple signals (desired and interfering signals) overlap both in time and frequency, their time varying statistics may be distinct. This *spectral correlation* property of cyclostationary signals enables blind signal extraction in interference environments.

A stochastic process $x(t)$ is cyclostationary if its mean and autocorrelation are periodic with some period T , i.e., $E[x(t)] = \mu_x(t) = \mu_x(t+T)$, and $E[x(t_1)x(t_2)] = R_{xx}(t_1, t_2) = R_{xx}(t_1+T, t_2+T)$ for all t_1 and t_2 .

The cyclic autocorrelation of $x(t)$ is given by

$$R_{xx}^a(\mathbf{t}) = \lim_{T \rightarrow \infty} \frac{1}{T} \int_{-T/2}^{T/2} x\left(t + \frac{\mathbf{t}}{2}\right) x^*\left(t - \frac{\mathbf{t}}{2}\right) e^{-j2p\mathbf{a}t} dt.$$

Its Fourier Transform is a measure of spectral redundancy [57]. A signal $x(t)$ is said to exhibit cyclostationarity at cycle frequency, α_c if $R_{xx}^a(\mathbf{t}) \neq 0$. An excellent tutorial on cyclostationarity and its applications can be found in the works of W.A. Gardner [57, 141]. Many signal extraction algorithms exploit the cyclostationary property of the incident signal waveforms for interference rejection, direction finding etc. A survey of these algorithms is given in Chapter 4.

3.1.2 MOBILE RADIO CHANNEL MODEL

Many of the signal extraction algorithms in the literature model the channel as a time variant, specular multipath fading channel. The time varying nature of the channel is generally attributed to the relative motion of the mobile terminals and scatters throughout the environment. For the general case where the receiver employs an array of antenna elements, a vector channel model is used. The channel model contains both the temporal and spatial characteristics of the channel, as seen by the given antenna array.

Figure 3.1 illustrates an arbitrary array geometry. Here, the m^{th} element is placed at coordinates (x_m, y_m, z_m) with respect to the reference element at the origin. In this model, the ground plane lies on the x - y principal plane. Further, we assume that all incoming waves arrive with an elevation angle of $\mathbf{q}=90^\circ$. This allows us to simplify the model and only consider the azimuthal

coordinate, \mathbf{f} . We also assume that all incoming signals are *narrowband with respect to the array*. This implies that the envelope of the signal will remain constant as the wave propagates across the array aperture. Only the phase of the signal will change as the wave propagates across the array aperture.

The response of an M -element array to a single plane wave is given by the *array steering vector*, $\mathbf{a}(\phi)$, where

$$\mathbf{a}(\mathbf{f}) = [a_0(\mathbf{f}) \ a_1(\mathbf{f}) \ \cdots \ a_{M-1}(\mathbf{f})]^T \quad (3.9)$$

Each element in this vector, $a_m(\mathbf{f})$, is defined to be the ratio of the response of the m^{th} element to the response of the reference element, which is typically labeled as the 0^{th} element. Accordingly, $a_0(\mathbf{f})=1$, and

$$a_m(\phi) = e^{-j\frac{2\pi}{\lambda}[(x_m - x_0)\cos\phi + (y_m - y_0)\sin\phi]} \quad (3.10)$$

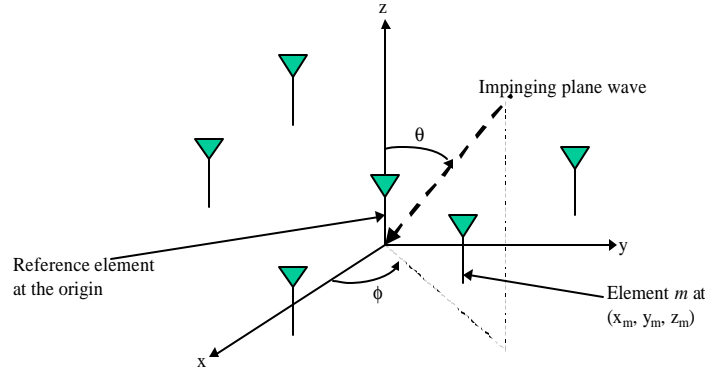


Figure 3.1: Geometry of an arbitrary antenna array

Therefore, the channel impulse response at the output of the m^{th} antenna in the array is modeled as follows

$$h_m(t; \mathbf{t}) = \sum_{i=0}^{K-1} a_m(\mathbf{f}_i(t)) \mathbf{a}_i(t) \mathbf{d}(\mathbf{t} - \mathbf{t}_i(t)) \quad (3.11)$$

where K is number of multipath components, $\mathbf{f}_i(t)$ is the slowly, time varying, angle of arrival of the i^{th} multipath component, $\mathbf{t}_i(t)$ is the excess delay associated with the i^{th} multipath component at time t , and $\mathbf{a}_i(t)$ is the complex channel gain associated with the i^{th} multipath component at time t . The independent variable, t , in the $\mathbf{t}_i(\mathbf{x})$ and $\mathbf{a}_i(\mathbf{x})$ accounts for the Doppler spreading

induced by the motion of the mobile unit and any moving scatterers that happen to be in the area. The amplitude of the complex channel gain is modeled as a zero mean Gaussian process whereas the phase has a uniform distribution.

The vector channel impulse response is therefore

$$\mathbf{h}(t; \mathbf{t}) = [h_0(t; \mathbf{t}) h_1(t; \mathbf{t}) \cdots h_{M-1}(t; \mathbf{t})]^T = \sum_{i=0}^{M-1} \mathbf{a}(\mathbf{f}_i(t)) \mathbf{a}_i(t) \mathbf{d}(\mathbf{t} - \mathbf{t}_i(t)) \quad (3.12)$$

Equations (3.10) and (3.12) model the wireless channel for *ideal* antenna elements. However, in practical systems, cross-sensor phase mismatches, near-field multipath and mutual coupling between array elements result in non-ideal array response vectors. An array with the response of (3.9) and (3.10) are called *calibrated arrays*. Otherwise, $\mathbf{a}(\mathbf{f})$ can be any complex vector. Array calibration is a very expensive procedure and usually is not affordable in commercial cellular systems. Note that the mere distinction between a scalar channel model (single antenna element at the receiver) and a vector channel model (array of antennas at the receiver) is the factor $a_m(\mathbf{f}_i(t))$, which contains the spatial information associated with the i^{th} multipath component in the case of multiple antennas. In a scalar channel model, $a_m(\mathbf{f}_i(t)) = 1$ and $m = 1$.

3.1.3 RECEIVED SIGNAL MODEL

The receiver signal vector is modeled as follows

$$\mathbf{x}(t) = s_1(t) * \mathbf{h}_1(t; \mathbf{t}) + \sum_{d=2}^D s_d(t) * \mathbf{h}_d(t; \mathbf{t}) + \mathbf{n}(t) \quad (3.13)$$

where:

- $s_1(t)$ is the signal of interest.
- $\{s_d(t)\}_{d=2}^D$ are cochannel interferers that employ the same modulation scheme.
- $\mathbf{n}(t)$ are spatially and temporally uncorrelated noise and interference sources that are modeled as a zero-mean, white Gaussian vector process.
- $\{\mathbf{h}_d(t; \mathbf{t})\}_{d=1}^D$ are the vector channel impulse responses associated with the d^{th} signal.

The objective of the receiver is to extract $s_1(t)$ from the above interference environment. For single-antenna (scalar) receivers, only temporal processing techniques are available.

Accordingly, the receiver can only exploit the temporal properties of the signal of interest, such as constant modulus, finite alphabet structure, etc.

If the received signal is filtered at the receiver and sampled at the baud rate then the resulting signal can be modeled with a digital equivalent channel model

$$\mathbf{x}(n) = \mathbf{x}(nT_s) = s_0(n) * \mathbf{h}_0(n;k) + \sum_{d=1}^D s_d(n) * \mathbf{h}_d(n;k) + \mathbf{n}(n) \quad (3.14)$$

Here, $s_d(n)$ is a sequence of symbols transmitted by the d^{th} user and $\mathbf{n}(n)$ is the filtered and sampled noise process. The quantity, $\mathbf{h}_d(n;k)$ is the time varying digital equivalent channel model for d^{th} user and accounts for the channel, impulse response, and receiver's front end filter.

On the other hand, vector receivers can employ combinations of spatial and temporal processing techniques. The digital equivalent channel model can be reduced to the following system of linear equations:

$$\mathbf{X}_{M \times N} = \mathbf{H}_{M \times L} \mathbf{S}_{L \times N} + \sum_{d=2}^D \mathbf{H}_d_{M \times L} \mathbf{I}_d_{L \times N} + \mathbf{N}_{M \times N} \quad (3.15)$$

Here, M is the number of antenna elements, L is the memory length of the time-varying channels, N is the number of collected data samples for each signal and D is the number of interfering signals. The matrices in (3.15) can be described as the following:

\mathbf{H} , \mathbf{H}_i are the channel response matrices for the desired signal and d^{th} interferer respectively. $\mathbf{S} = [s(n), s(n+1), \dots, s(n+N-1)]$ is the desired signal data matrix where $s(n) = [s_n, \dots, s_{n-L+1}]^T$. Similarly, \mathbf{I}_d is the signal data matrix for the d^{th} interferer, and finally \mathbf{N} is the noise matrix with complex Gaussian random variables.

Many algorithms in the literature, lump interference and noise into one *channel impairment* matrix, \mathbf{Z} .

$$\mathbf{Z} = \sum_{d=2}^D \mathbf{H}_d_{M \times L} \mathbf{I}_d_{L \times N} + \mathbf{N}_{M \times N} \quad (3.16)$$

This impairment process is spatially and temporally correlated therefore it is also called *colored noise*.

To date, a vector receiver that exploit the spatial coherence properties of the interfering signals can only extract the signal of interest if (1) the angular separation of $x_0(t)$ and each of the interferers exceeds the Rayleigh resolution limit of the array and (2) the total number of signals, D is less than the total number of array elements, M . In this thesis, we show that through the careful combination of spatial and temporal processing techniques, one could extract the signal of interest even *in overloaded array environments* i.e., when the total number of signals exceeds M .

3.2 INTRODUCTION TO THE SIGNAL EXTRACTION TECHNIQUES

This section is intended to give the reader a concise overview of some of the commonly used terminology in the survey section of the thesis. For those who are familiar with equalization, but not array processing, we define an analogy between temporal and spatial filtering. Several standard algorithms are referred to throughout this tutorial. This survey will rely on some background in adaptive filtering, maximum likelihood sequence estimation (MLSE), and fractionally spaced processing. However, detailed knowledge of each topic will not be required. We first review four adaptive algorithms commonly used for linear adaptive processing and channel estimation. Secondly, we define a nomenclature for multi-channel filtering. Finally, we review some non-linear processing techniques, namely MLSE.

3.2.1 ANALOGY BETWEEN LINEAR ARRAY PROCESSING AND TEMPORAL EQUALIZATION

Linear processing with antenna arrays is a signal processing technique called spatial filtering or *beamforming*. A beamformer uses the array of antenna elements to exploit the spatial separation of impinging signals that have overlapping frequency content. This spatial filtering process enables the beamformer to separate the desired signals from the interfering signals by adaptively updating its weights and steering beams towards the desired users.

Spatial filtering and temporal filtering (i.e. equalization) have similar principles. Figure 3.2 depicts spatial filtering where spatially sampled time series, $x_m(k)$, are combined from the m^{th} sensor and weights are updated using adaptive algorithms to obtain a scalar output, $y(k)$. Similarly, in adaptive equalization techniques, the filter taps are adaptively updated to result in a scalar output as shown in figure 3.3. Many weight adaptation algorithms exist in the signal processing literature. These algorithms find applications in both spatial processing and temporal

processing. We will introduce three most commonly used adaptation techniques namely the *Least Means Squares (LMS)*, *Direct Matrix Inversion (DMI)* and *Recursive Least Squares (RLS)*.

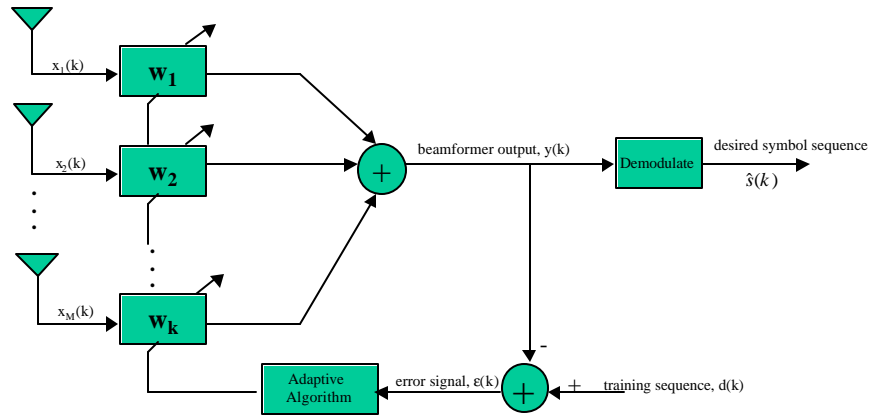


Figure 3.2: Linear beamformer for single user interference rejection. Complex antenna weights, w , are updated by using an adaptive algorithm. The beamformer output is a linear combination of the received signal with the complex weights.

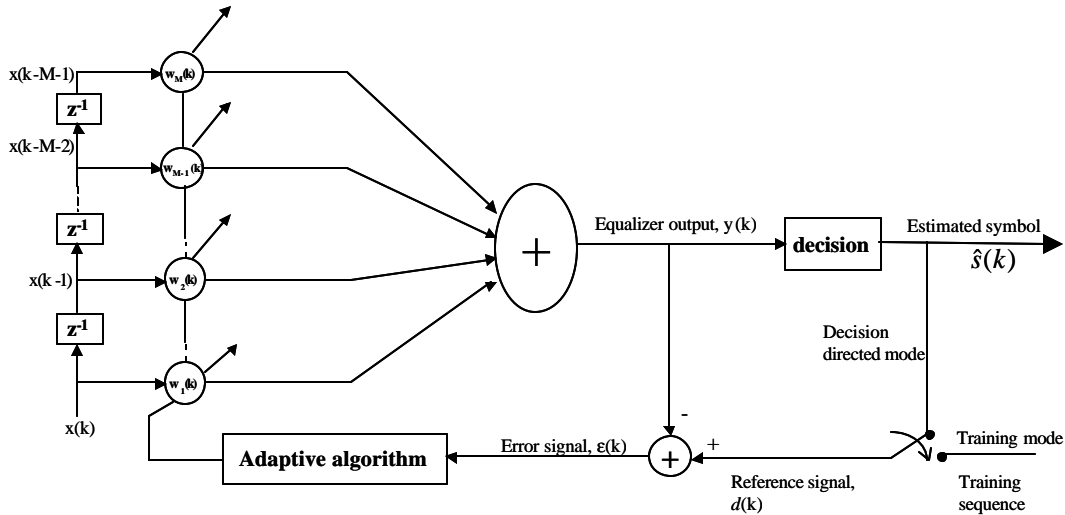


Figure 3.3: Linear equalizer using an adaptive algorithm to adapt the complex taps, w .

3.2.2 COMMON ADAPTATION TECHNIQUES

The main goal of the adaptive algorithms used in spatial and temporal processing is to maximize the output signal-to-interference-plus-noise ratio (SINR). This is accomplished by minimizing the cost functions associated with various criteria, e.g., *Minimum Mean Squared Error (MMSE)*

and *Least Squares*(*LS*) criteria. In this section, we will define four algorithms for adaptively updating an FIR filter (spatial or temporal). These techniques can also easily be extended to perform channel estimation.

The signal estimate $y(k)$ is assumed to be estimated from a finite collection of received data samples, $\mathbf{x}(k)$ with an FIR filter, or weight vector, \mathbf{w} . This can be expressed with the following equation:

$$y(k) = \mathbf{w}^H \mathbf{x}(k) \quad (3.17a)$$

where \mathbf{w}^H is the complex conjugate transpose of the weight. The vector $\mathbf{x}(k)$, can be a collection of past time samples, in the case of temporal filtering, or a collection of antenna outputs, in the case of spatial filtering.

The cost function for the MMSE criterion (3.17b) is the expected value of the square error between the beamformer (or equalizer) output and the desired version of that signal:

$$J(\mathbf{w}) = E \left[|y(k) - d(k)|^2 \right] \quad (3.17b)$$

where $d(k)$ is the desired version of the signal [138].

The optimal solution for the weights can be found by $\mathbf{w}_{opt} = \mathbf{R}_{xx}^{-1} \mathbf{p}$ where

$$\mathbf{R}_{xx} = E \left[\mathbf{x}(k) \mathbf{x}^H(k) \right] \quad (3.18a)$$

$$\mathbf{p} = E \left[\mathbf{x}(k) d^*(k) \right] \quad (3.18b)$$

The well known Least Means Squares (LMS) algorithm is a Stochastic Gradient technique that attempts to minimize the MMSE cost function. LMS updates the weights with the following update formula:

$$\mathbf{w}(k+1) = \mathbf{w}(k) + m \mathbf{x}^* \mathbf{e}(k) \quad (3.19)$$

where m is a constant step size and the error signal, $\mathbf{e}(k)$, is given by

$$\mathbf{e}(k) = d(k) - y(k). \quad (3.20)$$

LMS is a computationally simple algorithm. Its complexity grows linearly with M (number of filter taps or number of antenna elements). However it suffers from slow convergence due to the statistical averaging [137].

Unlike the MMSE criterion, the LS criterion tries to minimize the *time-average* error between the linear processor output and a desired response over a *finite* number of time samples instead of the *ensemble* average [138]:

$$J(\mathbf{w}) = \left| \sum_{q=1}^Q \mathbf{w}^H \mathbf{x}_q - d_q(k) \right|^2 \quad (3.21)$$

where \mathbf{x}_q is the q^{th} received data vector, $d_q(k)$ is the q^{th} desired signal at time k , and Q is the number of snapshots of the data vector.

The optimal weight vector that forces the LS gradient function to zero is given by:

$$\mathbf{w} = (\mathbf{X}^H \mathbf{X})^{-1} \mathbf{X}^H \mathbf{d}(k) \quad (3.22)$$

where $\mathbf{X} = [\mathbf{x}_1, \mathbf{x}_2, \dots, \mathbf{x}_Q]$ is the received data matrix and $\mathbf{d}(k) = [d_1(k), d_2(k), \dots, d_Q(k)]$ is the desired signal vector.

Two adaptation algorithms evolve from the LS criterion. The first one is the Direct Matrix Inversion (DMI) algorithm that uses the following solution for the optimum weight vectors:

$$\mathbf{w}_{opt} = \hat{\mathbf{R}}_{xx}^{-1} \hat{\mathbf{r}}_{xd} \quad (3.23)$$

where estimated receive signal correlation matrix $\hat{\mathbf{R}}_{xx}$, and estimated reference signal vector $\hat{\mathbf{r}}_{xd}$ are given by:

$$\hat{\mathbf{R}}_{xx} = \frac{1}{Q} \sum_{j=1}^Q \mathbf{x}_j^* \mathbf{x}_j^T \quad (3.24a)$$

$$\hat{\mathbf{r}}_{xd} = \frac{1}{Q} \sum_{j=1}^Q \mathbf{x}_j^* d_j \quad (3.24b)$$

The DMI algorithm attempts to find the optimum weight vector (3.23) after adapting $\hat{\mathbf{R}}_{xx}^{-1}$ and $\hat{\mathbf{r}}_{xd}$ using:

$$\hat{\mathbf{R}}_{xx}(k+1) = \lambda \hat{\mathbf{R}}_{xx}(k) + \mathbf{x}^*(k) \mathbf{x}^T(k) \quad (3.25a)$$

$$\hat{\mathbf{r}}_{xd}(k+1) = \lambda \hat{\mathbf{r}}_{xd}(k) + \mathbf{x}^*(k) d(k) \quad (3.25b)$$

where λ is the forgetting factor.

Although DMI algorithm has a faster convergence rate than the LMS method, it requires a matrix inversion process which can be computationally undesirable, i.e. complexity grows with M^3 . Therefore, a recursive algorithm, called Recursive Least Squares (RLS) algorithm, is widely used in practice as a computationally efficient alternative to the DMI by recursively updating the weights and the computation of the $\hat{\mathbf{R}}_{xx}^{-1}$:

$$\mathbf{w}(k) = \mathbf{w}(k-1) + \mathbf{u}(k) \mathbf{e}^*(k) \quad (3.26a)$$

$$\mathbf{R}_{xx}^{-1}(k) = \frac{1}{\lambda} \left[\mathbf{R}_{xx}^{-1}(k-1) - \mathbf{u}(k) \mathbf{x}^H(k) \mathbf{R}_{xx}^{-1}(k-1) \right] \quad (3.26b)$$

where $\mathbf{u}(k)$ and $\mathbf{e}(k)$ are given by

$$\mathbf{e}(k) = d(k) - \mathbf{w}^H(k-1) \mathbf{x}(k) \quad (3.27c)$$

$$\mathbf{u}(k) = \frac{\mathbf{R}_{xx}^{-1}(k-1) \mathbf{x}(k)}{\lambda + \mathbf{x}^H(k) \mathbf{R}_{xx}^{-1}(k-1) \mathbf{x}(k)} \quad (3.27d)$$

The recursive update for $\hat{\mathbf{R}}_{xx}^{-1}$ is derived from the *matrix inversion lemma* [198]. The computational complexity of the RLS algorithm grows with M^2 . However, its convergence is much faster than the LMS algorithm since the error measures are expressed in terms of a time average of the actual received signal instead of a statistical average [136].

The above mentioned algorithms require a reference signal, e.g. training sequence, in order to compute the optimum weight vector. There is another class of algorithms which requires neither training sequences nor estimate of the desired signal. These algorithms are classified as *blind* algorithms. Blind adaptation techniques attempt to restore some known property to the received signal. Among the most widely used blind techniques is the class of Constant Modulus Algorithms (CMA), where the optimum weights try to derive the antenna array output (or

equalizer output) to have a constant modulus with a specific amplitude, \mathbf{a} . The generic CMA cost function is given by

$$J(\mathbf{w}) = E \left[\left| |y(k)|^p - |\mathbf{a}|^p \right|^q \right] \quad (3.28a)$$

where p and q are either 1 or 2.

The weight update equation can then be written as

$$\mathbf{w}(k+1) = \mathbf{w}(k) - \mu \mathbf{x} \mathbf{e}^*(k) \quad (3.28b)$$

$$\mathbf{e}(k) = 2 \left(y(k) - \frac{y(k)}{|y(k)|} \right) \quad (3.28c)$$

As can be seen from (3.28c), the error merely depends on the CM characteristics of the processor output, $y(k)$. CMA-based signal extraction algorithms are widespread in the literature and thus are dealt in some detail in Chapter 4 of the thesis.

3.2.3 MIMO FILTERING VS. MISO FILTERING

A multiple input single output (MISO) linear processor was shown in figure 3.2. The linear beamformer extracts a single desired user at a time from the linear combination of the signals impinging on the array. This is an example of a MISO spatial filtering. In a multiple-input multiple-output (MIMO) system, a linear beamformer extracts multiple signals simultaneously as shown in figure 3.4. Two important issues arise with a MIMO beamformer. The first issue is the generation of different weight vectors in each port. Each of the D weight vectors should converge to D distinct spatial response. In non-blind techniques, different training sequences are used for different ports to ensure distinct beamformer responses. However, blind MIMO beamformers must employ some additional procedures to cope with this problem. In fact, a very efficient blind beamforming algorithm, *Multi-Target LS-CMA* [152] proposes a solution and it is discussed in Chapter 4. The second important issue associated with a blind MIMO beamformer is that a given desired signal can be extracted from any one of the D ports. This uncertainty is referred to as the *port shuffle* problem and it is pertinent only to blind techniques. More elaboration on this concept as well as on the algorithms that attempt to solve this problem are given in Chapter 4.

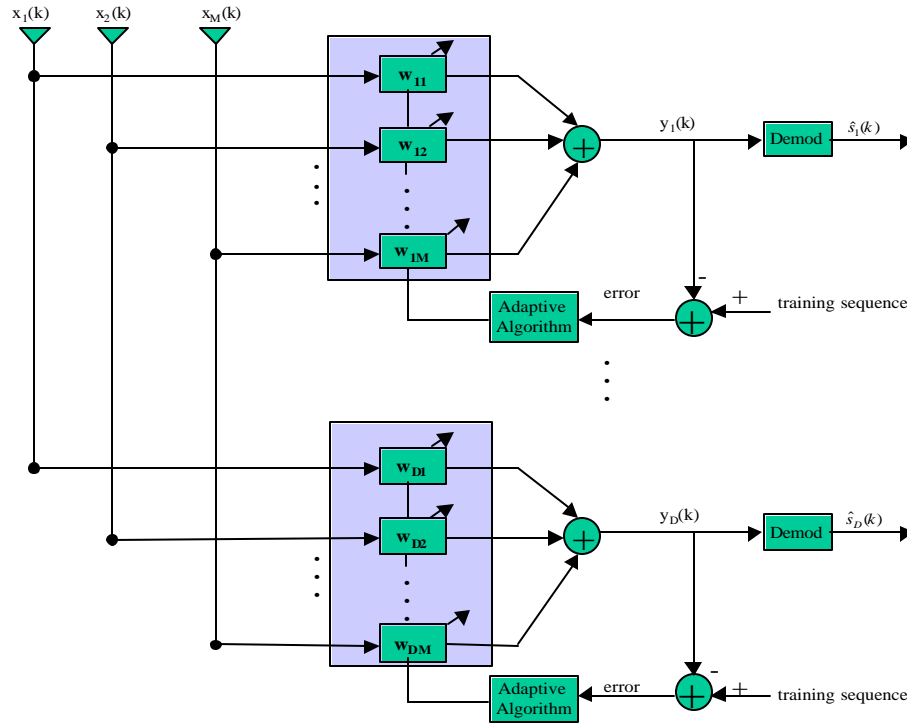


Figure 3.4: MIMO Beamformer. Multi-user linear beamformer is a multiple input multiple output linear system where each user is beamformed and demodulated simultaneously.

3.2.4 NON-LINEAR PROCESSING

Non-linear processing is a powerful technique for separating interfering users. Two major non-linear processor structures used for multipath equalization as well as joint detection are Decision Feedback Equalizer (DFE) and Maximum Likelihood Sequence Estimator (MLSE). Well known single-user DFE structure can be modified into a multi-user DFE structure by incorporating MIMO feedforward and MIMO feedback filters. The resulting MU-DFE structure is shown to jointly detect symbols from multiple users (via the MIMO feedforward filter) as well as canceling the ISI for each user symbol simultaneously (via the MIMO feedback filter). An extensive analysis of this structure is presented in Chapter 5 of the thesis.

It is well known that an MLSE detector provides the minimum error probability, by minimizing the maximum likelihood function, in a channel with memory and additive white Gaussian noise. In research community, MLSE has taken two slightly different forms in terms of its use, i.e., it can be used as a joint detection technique for signal extraction or it can be used as an equalizer to mitigate ISI. The literature survey in Chapter 4 contains algorithms based on these variations of MLSE detection.

MLSE used as a joint detector for signal separation

MLSE can be used to carry out joint demodulation of all the users impinging on an antenna or an antenna array. This technique can be implemented in two ways depending on the channel assumptions:

1. **ML symbol-by-symbol joint detector:** MLSE boils down to a symbol-by-symbol joint detector if all the user symbols are perfectly synchronized and if there is no ISI in the channel. This is a brute-force search to find the ML path that gives the minimum probability of error. MLSE is an example for this type of joint detector and relative features of this algorithm is extensively studied in Chapter 5.
2. **ML Joint detection trellis:** In the case when users are asynchronous or when ISI is present, the optimum choice of any given symbol is dependent on previous symbols. Such a joint detection scheme has memory which can be represented by a trellis. Hence, Viterbi Algorithm [173] is utilized to find the ML path through the trellis and jointly separate the user symbols.

MLSE used as an equalizer for ISI mitigation

MLSE can be used to mitigate the ISI induced by the frequency-selective channel. Again, Viterbi Algorithm is used to cancel the ISI and therefore MLSE acts as an equalizer. The states are determined by current and previous transmitted symbols of a user, and VA tries to find the ML path to decode the original transmitted sequence. The original papers on MLSE as an equalizer can be found in [54, 55].

As mentioned above, whether used as an equalizer or joint detector for asynchronous multi-user symbols, MLSE structure always requires the use of Viterbi Algorithm if the channel has some memory (due to ISI and/or asynchronicity among multiple user symbols). Therefore, the purpose of this section is to give a general overview of the Viterbi Equalization since many of the papers in our literature survey utilize some form of ML joint detection and/or MLSE equalization.

The Viterbi Algorithm efficiently performs MLSE in channels with memory. Channel memory models the fact that in many wireless channels, a given received sample is a function of previously transmitted symbols. In the case of a multipath channel, memory is imposed by inter-symbol interference (ISI). This is illustrated in figure 3.5. The channel state $\mathbf{s}[k]$, is the previous two transmitted BPSK symbols: $\mathbf{s}[k] = (s[k-1], s[k-2])$. Thus the channel is said to have 2 symbols of ISI, which defines the channel length, L .

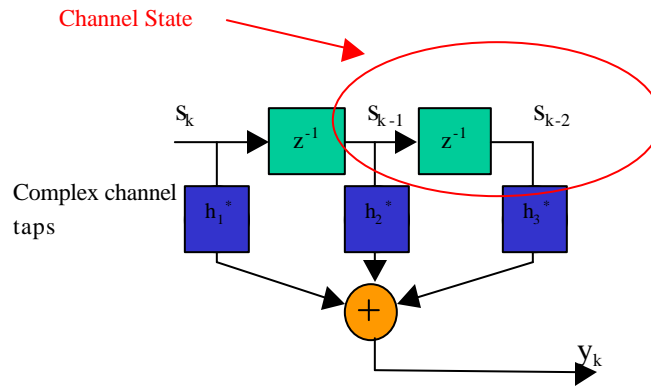


Figure 3.5: FIR digital equivalent channel model: binary BPSK symbols $\in \{-1,1\}$ are shifted into a shift register. The current output is a linear combination of the current and previous symbols.

A trellis is a way of visualizing all possible state sequences of a certain length. Figure 3.6 shows the full trellis for the case where a block of N BPSK symbols passes through a frequency-selective channel of length, $L = 3$. The entire trellis is constructed by concatenating the 0^{th} stage, with the 1^{st} stage, the 2^{nd} , stage, and so on. Note that the state at the 0^{th} stage is assumed to be known and the trellis is forced back to this known state (in figure 3.6, ‘all ones’ state) at the end of N^{th} stage. Total number of states at each stage is given by J^{L-1} where J is the alphabet size ($J = 2$ for BPSK).

Figure 3.7 illustrates the zoomed in version of the k^{th} stage of the trellis of figure 3.6. This figure illustrates the fact that only certain transitions from one channel state to the next are possible. At stage k , each transition from state i to state j has a corresponding error metric denoted by $e_{ij}[k]$. This error metric depends on the difference between the actual received signal sample corrupted with noise and candidate received sample (for equalization, candidate received sample is obtained from convolving the candidate symbols with the channel coefficients). It can be shown that maximum likelihood sequence estimation is equivalent to minimizing a path through the

trellis. A brute force method of minimizing a path through a trellis is to enumerate through all possible paths ($\sim \mathcal{J}^{(L-1)N}$ paths), picking the one with the least cost. However, the Viterbi algorithm reduces the complexity of the search by culling candidate paths with the least accumulated error at each stage of the trellis. After paths are culled at each stage, the remaining candidates are called survivors. The expression for the survivor path at the j^{th} state of the k^{th} stage is given by;

$$i_s^j[k] = \underset{i}{\operatorname{argmin}} \{ \mathbf{x}^{(i)}[k-1] + e^{(i,j)}[k] \} \quad (3.29)$$

where $\mathbf{x}^{(i)}[k-1]$ is the accumulated error at the i^{th} state of the $k-1^{\text{th}}$ stage and $e^{(i,j)}[k]$ is the cost of transition from i^{th} to j^{th} state at stage k .

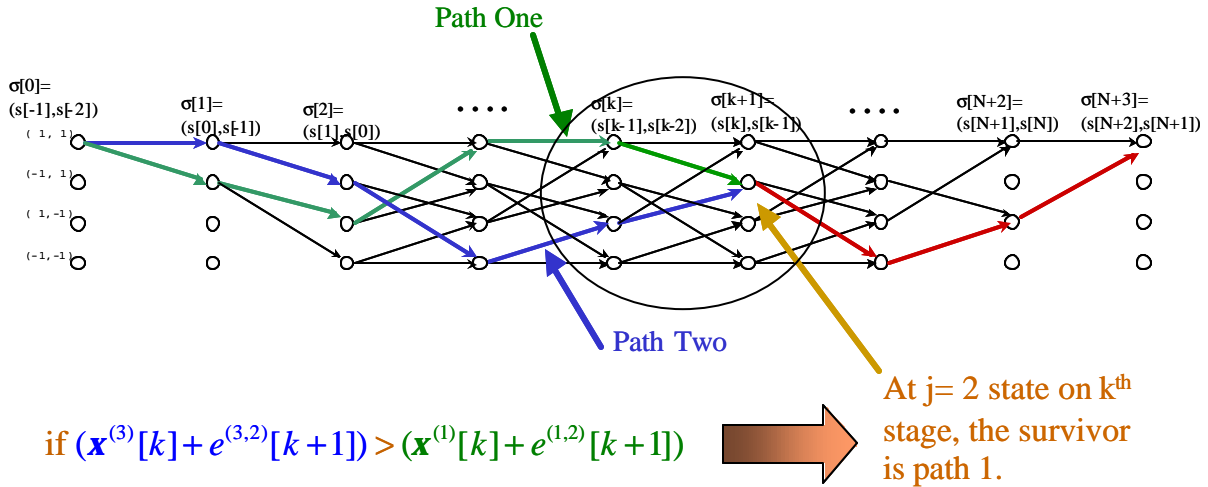


Figure 3.6: Full trellis structure. BPSK symbols pass through a frequency-selective multipath channel (modeled as FIR filter) with 3 symbols of ISI (i.e., $L = 3$)

Transition at k^{th} stage:

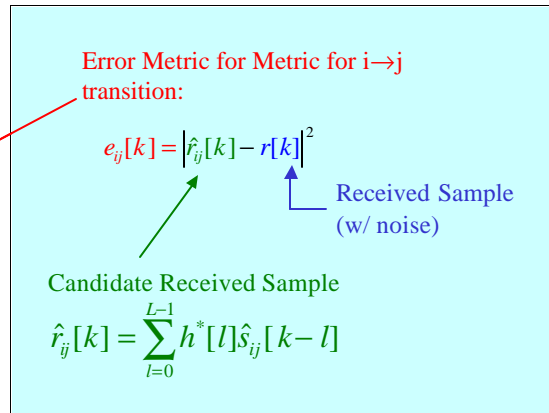
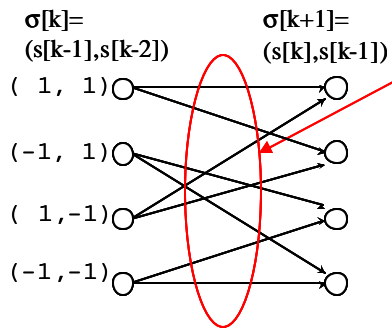


Figure 3.7: Zooming in the transition at the k^{th} stage. Equation for calculating the error metric for the $i \rightarrow j$ transition is also given here.

CHAPTER 4: SURVEY OF NARROWBAND SIGNAL EXTRACTION ALGORITHMS

In Chapter 1, we have introduced the importance of overloaded array processing in airborne communication systems such as airborne repeaters. We have also mentioned that overloaded array processing is a very challenging issue especially for narrowband TDMA/FDMA type systems since narrowband signals do not have the luxury of spreading gain.

In our algorithm-level research, we have focused on two major types of signal extraction techniques: interference rejection and joint detection (or multi-user detection). The differences between these two approaches were briefly mentioned in Chapter 1.

The purpose of this chapter is to give the reader an extensive survey of many different types of narrowband signal extraction techniques, some of which are found to be applicable to overloaded array processing. The algorithms are divided into two major parts. Firstly, we give a survey of single channel signal extraction algorithms. All of these algorithms employ a single antenna receiver structure. In the second part of the survey, we focus on algorithms that exploit spatial diversity by using a receiver with an array of antennas at the front end. Both single-channel and multi-channel signal extraction algorithms are then subdivided into interference rejection (non-blind and blind) and joint detection algorithms. Non-blind and blind interference rejection techniques are further broken down into *linear* and *non-linear* techniques depending on the type of processor they use for signal extraction.

4.1 SINGLE-CHANNEL SIGNAL EXTRACTION ALGORITHMS

As mentioned before, single-channel signal extraction algorithms include *interference rejection* and *joint detection* techniques. In all these algorithms, only temporal processing is utilized since the receiver antenna at the base station contains only one element. Figure 4.1 shows the further breakdown of the algorithms.

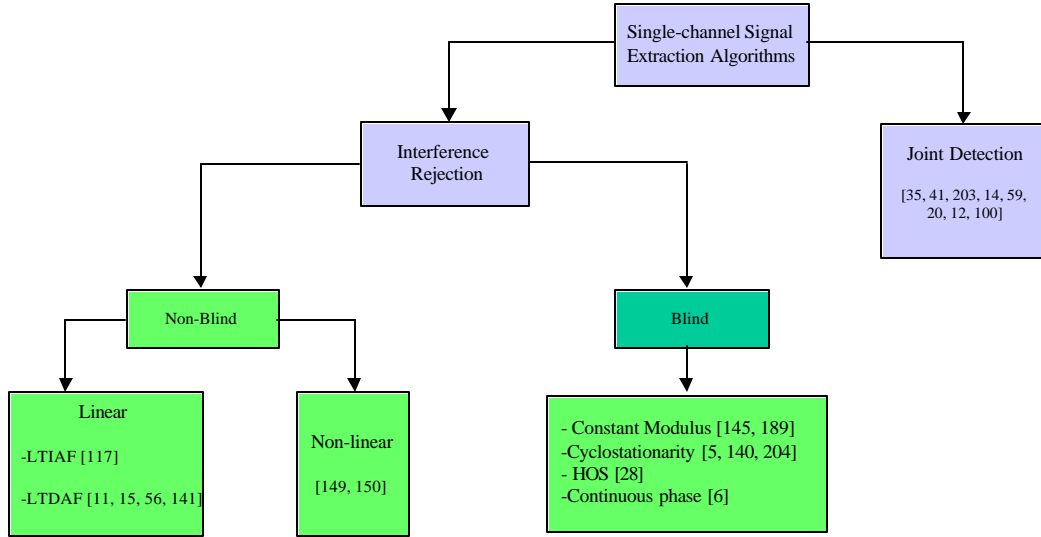


Figure 4.1: A breakdown of the single-channel signal extraction algorithms

4.1.1 INTERFERENCE REJECTION ALGORITHMS

This section is broken into non-blind and blind interference rejection techniques that only employ temporal processing. The non-blind techniques employ some sort of training to estimate channel and receiver parameters with adaptive processing. On the contrary, in blind techniques training sequences are not available and channel is estimated using some known structure of the signals. The survey in this section is not exhaustive and thus the reader is referred to [37] for a more detailed survey.

4.1.1.1 NON-BLIND TECHNIQUES

Non-blind adaptive processing can be broken into three main approaches: Linear Time-Independent Adaptive Filtering (LTIAF), Linear Time-dependent Adaptive Filtering (LTDAF), and non-linear adaptive processing using Decision Feedback Equalizer (DFE) and Maximum Likelihood Sequence Estimator (MLSE).

Strictly speaking, all adaptive algorithms are non-linear and time varying. However, the first two adaptive structures, LTIAF and LTDAF, have linear receiver architectures, i.e., FIR filter structure. Therefore, we can categorize all the adaptive algorithms that use LTIAF and LTDAF structures as *linear* non-blind techniques.

4.1.1.1.1 Linear Time-Independent Adaptive Filtering (LTIAF)

Linear time invariant filters may be used to equalize ISI but, to some degree, LTI filters can also perform interference cancellation. The reader is referred to [174] for a survey of adaptive equalization algorithms. An example of a LTIAF for equalization and interference cancellation is given in [117]. Here, the output of the equalizer is decomposed into a Wiener Filter (WF) term and a misadjustment filter (MF) term. Interference rejection is done by creating a notch in the frequency response of the WF. In spite of its low computational complexity, any LTIAF can at best cancel only a single narrow-band interferer and therefore is expected to fail in high interference environments.

4.1.1.1.2 Linear Time-Dependent Adaptive Filtering (LTDAF)

As previously mentioned, most digital waveforms and many analog waveforms can be classified as cyclostationary or conjugate cyclostationary. Interference rejection can be performed by exploiting the cyclostationary properties of the signal of interest and interfering signals. Gardner [141] has shown that the optimal filter for cyclostationary signals is a polyperiodic filter. This periodically time-varying filter exploits the spectral coherence of the signal of interest by linearly combining discrete frequency-shifted and filtered versions of the received signal. The optimal choice of the discrete frequency shifts has been shown to be the cyclic frequencies, α_k , of the signal of interest. There are many implementations of polyperiodic filters, and one simple structure is the so-called FREquency SHift (FRESH) filter. An LTDAF consists of a bank of such FRESH filters whose coefficients are updated using a host of adaptive algorithms e.g., RLS or LMS, in tandem with training sequences. General structure of a LTDAF is shown in figure 4.2. Several implementations of the TDAF are available such as the Time-Series-Representation TDAF (TSR TDAF), or the Frequency Domain TDAF (FD TDAF)[11]. All have identical optimal performance but exhibit different convergence properties [15].

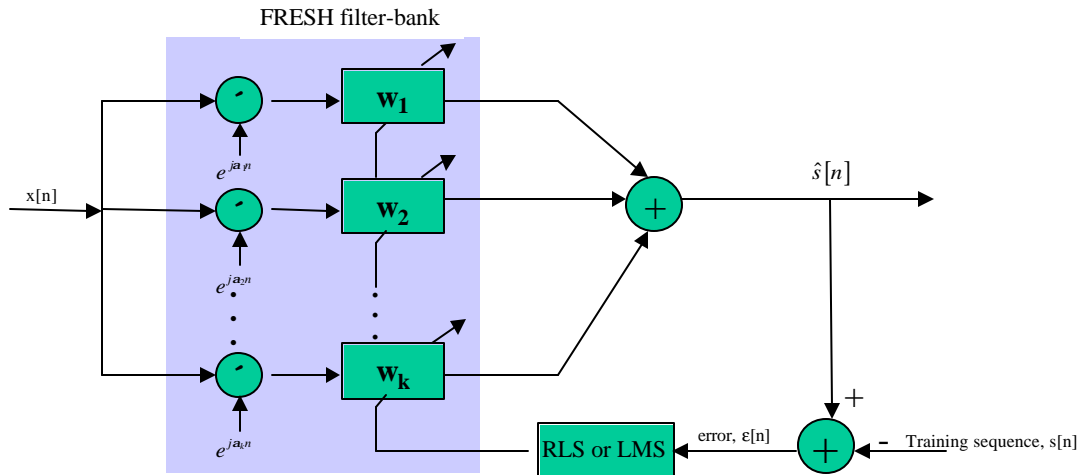


Figure 4.2: Linear Time-Dependent Adaptive Filter.

Reed *et al.*[56] has found that LTDAFs are effective in rejecting interference that exhibits different cyclostationary properties than the SOI. They specifically show that a LTDAF can separate two equal power, co-channel, square pulse shaped, PAM signals at an SNR of 30dB. However, the performance is found to be highly sensitive to the excess bandwidth of the SOI. Zero excess-bandwidth (e.g., $r = 0$ roll-off factor QPSK signals) cannot be effectively estimated directly with a TDAF.

4.1.1.1.3 Non-linear adaptive processing

Despite their low computational complexities and simple structures MMSE linear equalizers (LTDAF and LTIAF) are not very efficient on channels with deep spectral nulls in the passband. This is because the linear equalizer places high gain near the spectral null in order to compensate for the distortion and thereby enhances the noise present in those frequencies. Nonlinear methods do not suffer from this phenomenon. One of the most common forms of non-linear adaptive processor is the *Decision Feedback Equalizer (DFE)*.

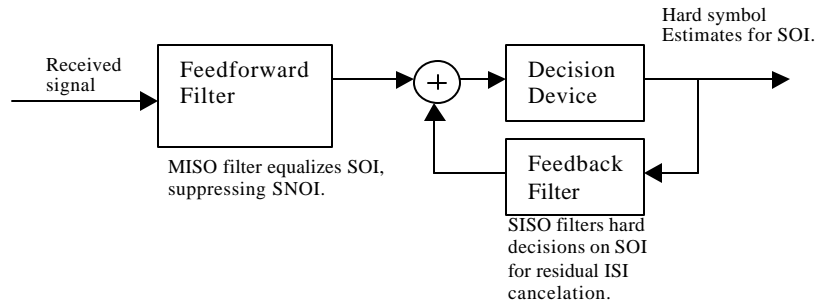


Figure 4.3: Application of a DFE to signal extraction. Both feedforward and feedback filters are realized as tapped delay lines. The feedforward filter acts as an interference canceller whereas the feedback filter cancels the ISI for the desired user. Generally, the filter weights are updated using either LMS or RLS algorithms.

DFE has been widely used as an equalizer to mitigate the ISI in the channel. Generic Multiple Input Single Output (MISO) DFE structure is shown in figure 4.3. The reader is referred to [136, 170, 174] for a detailed discussion. In addition to ISI mitigation, DFE can perform limited interference rejection. Lo *et al* [149, 150] proposes an adaptive, fractionally spaced DFE to cancel interference (both co-channel and adjacent channel) and suppress ISI in the presence of a single, dominant co-channel signal and uncorrelated, additive Gaussian noise.

4.1.1.2 BLIND TECHNIQUES

Blind algorithms must extract a signal by exploiting some other property of the modulated waveform. These properties may include but are not limited to the constant modulus property, the finite alphabet property, or cyclostationary properties.

In environments with multiple signals of the same type, many blind algorithms suffer from the signal capture problem. For instance, suppose a receiver attempts to extract a signal by restoring its modulus. Further, suppose that there are several CM signals in the environment. Then, there is no guarantee that the algorithm will extract the SOI. *Signal Capture* occurs when a blind algorithm extracts the wrong signal. This is illustrated in figure 4.4.

Constant modulus algorithms perform blind signal extraction by exploiting the constant modulation property of the SOI. The simplicity of constant modulus algorithms and their near optimal performance have made them a very popular blind family of algorithms.

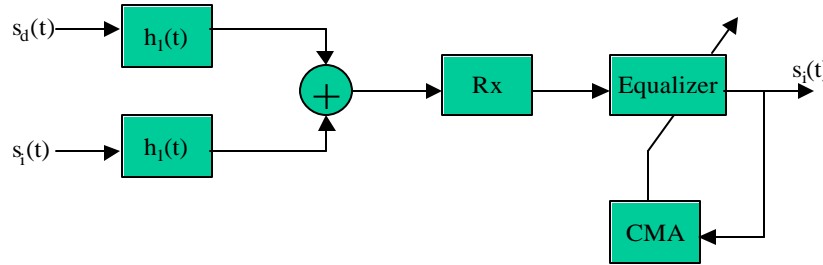


Figure 4.4: The signal capture problem: CMA captures the interfering signal, $s_i(t)$ instead of the desired signal, $s_d(t)$

However, CM algorithms have been observed to suffer from the signal capture problem. Rude and Griffiths developed Linearly Constrained Constant Modulus Algorithm (LCCM) that incorporate *a priori* knowledge about the signal of interest, e.g. known pulse shape, into the CMA filter and thus mitigate the signal capture problem [189]. The same authors apply the LCCM algorithm to interference cancellation by using it as an untrained (blind) start-up equalizer for a conventional DFE [145]. The LCCM, in a sense, initializes the DFE by acquiring the SOI and placing a null on the narrowband co-channel interferer.

Original LTDAF algorithms require training sequences. However, blind TDAF algorithms have also been presented in the literature. Two blind TDAF algorithms were developed in [204] which are both shown to discriminate between two equal-power QPSK and BPSK signals, closely spaced in carrier frequency. A blind adaptive FRESH filter and its convergence properties are described in [140]. A similar implementation [5] discussed an application for AMPS cellular signals which exploits the cyclostationarity induced in an FM modulated voice signal by a supervisory audio tone (SAT). A two stage TDAF was able to separate two co-channel equal power interferers with an output voice SNR of 30 dB.

As explained in Chapter 3, FM signals have continuous phase property that can be exploited for signal extraction using a sequence estimator. This novel technique is analyzed by Hamkins [6]. The author developed a blind technique to separate co-channel FM signals by exploiting the *temporal correlation* of the modulated speech signal. The technique quantizes the slope of the message signal for all CCIs. The Viterbi Algorithm then attempts to find the maximum

likelihood estimate of a sequence of slopes. The algorithm has been found to successfully demodulate two equal-power, co-channel interfering signals. However, the resulting size of the trellis is 2^{3d} (d : the number of co-channels signals), which can be prohibitively complex for large number of interferers.

4.1.2 JOINT DETECTION AND ESTIMATION ALGORITHMS

The interference rejection techniques mentioned in Section 4.1.1 attempt to estimate interfering signals and then strip them from the total signal, leaving only the desired signal components plus noise. On the other hand, joint detection algorithms recover all the signals, desired and interfering, from the signal environment and then discard the latter. These algorithms are based on the *Maximum Likelihood (ML)* and *Maximum a Posteriori (MAP)* criteria for the joint recovery of the cochannel signals. These criteria are used to derive two important sequence estimation and symbol-by-symbol detection techniques, *Maximum Likelihood Sequence Estimation (MLSE)* and *Maximum a Posteriori Symbol Detection (MAPSD)* [171], respectively.

An example for computationally complex joint detector is the *Interference Canceling Equalizer (ICE)* [35, 203] whose structure is depicted in figure 4.5. ICE uses a reduced state ML sequence estimator, i.e. *Reduced State Sequence Estimation (RSSE)* algorithm [172]. For a single antenna, the algorithm successfully separates two equal-power co-channel QPSK users provided that the phases of interfering users do not coincide, i.e. there is no signal ambiguity. However, the complexity of the algorithm becomes prohibitively expensive for a large number of users as well as for large channel memory length (due to ISI and/or due to asynchronous user symbols). This is because the number of states of RSSE is $J^{D(L-1)}$, where J is the alphabet size, D is the number of users and L is the channel memory length.

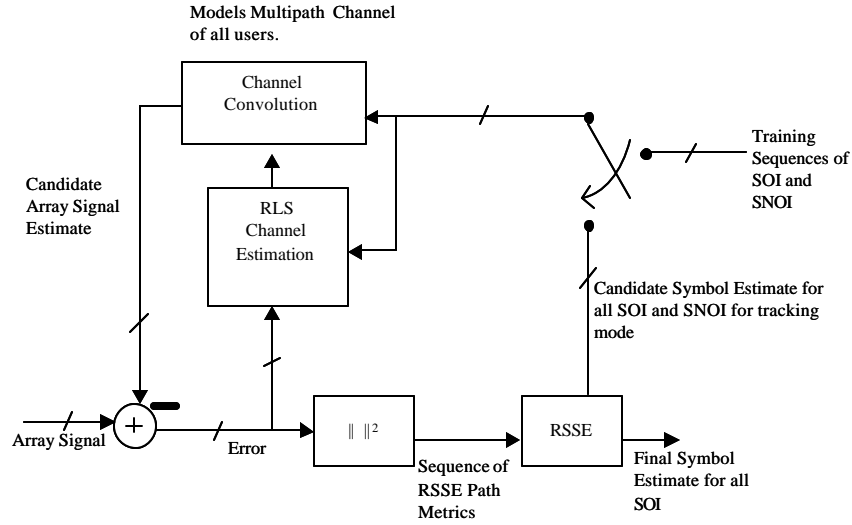


Figure 4.5: Block diagram of the ICE joint detector. The ICE uses a reduced state ML sequence estimator, RSSE, by accounting for ISI in the error metric of the Viterbi Algorithm. The channel is estimated from a set of training sequences with the RLS algorithm, and tracked with a decision feedback equalizer.

Gridhar *et. al* [14, 20, 59] extended the classical MLSE and MAPSD to *Joint MLSE (JMLSE)* and *Joint MAPSD (JMAPSD)* algorithms. The authors use a sub-optimal two-stage JMAPSD structure as shown in figure 4.6 to successfully demodulate two cochannel sources at low SNRs.

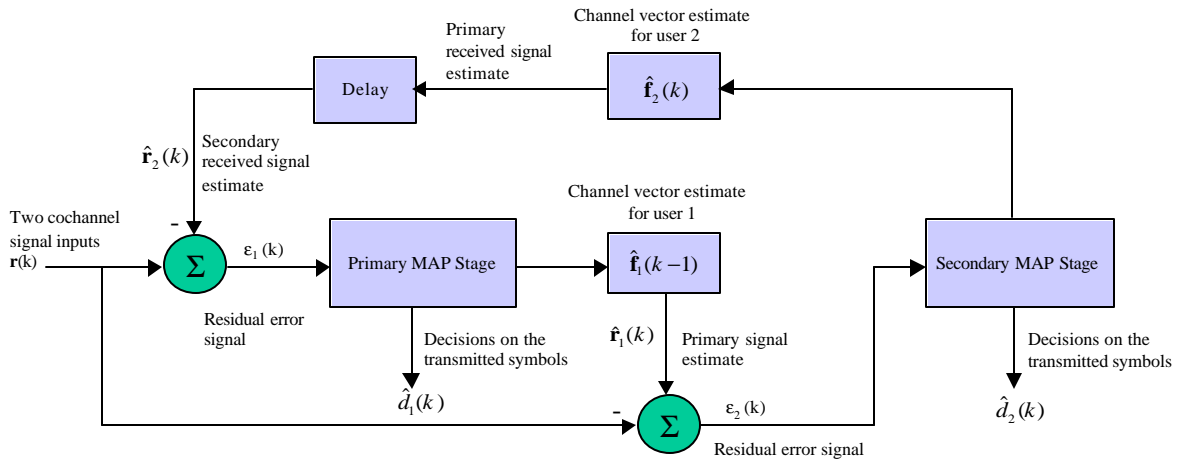


Figure 4.6: Two-Stage JMAPSD Algorithm

Ranta *et. al* [12] describe a joint detection technique for GSM signals using a joint channel estimator together with a JMLSE. The authors show that proposed receiver jointly detects the SOI and a single dominant CCI as long as the sum power of other interferers is 20dB lower than the strongest one.

4.2 MULTI-CHANNEL SIGNAL EXTRACTION ALGORITHMS

In a mobile communication system, multipath and interference are the major impairments to the signal quality and system capacity. Multipath propagation gives rise to fading and time dispersion. The time dispersion problem can be solved using linear equalizers or non-linear equalization techniques such as DFE and MLSE. Multipath fading can be mitigated by antenna diversity at the receiver. These multiple antennas collect more signal energy and diversity gain due to the spatial separation. When the antennas are spaced appropriately, there is a good chance that not all of them will fade at the same time. Moreover, multiple antennas can be used to combine multiple copies of both desired and interfering signals in such a way that, the desired signal components add constructively whereas the interfering signals add destructively. This process of exploiting spatial diversity is called *spatial equalization*. Space-Time Adaptive Processing (STAP) receivers combine spatial and temporal equalization in order to provide better interference rejection performance as well as better ISI reduction than single antenna receivers. Similar to single antenna array processing techniques, STAP algorithms can be classified according to how they treat interference: interference rejection or joint detection.

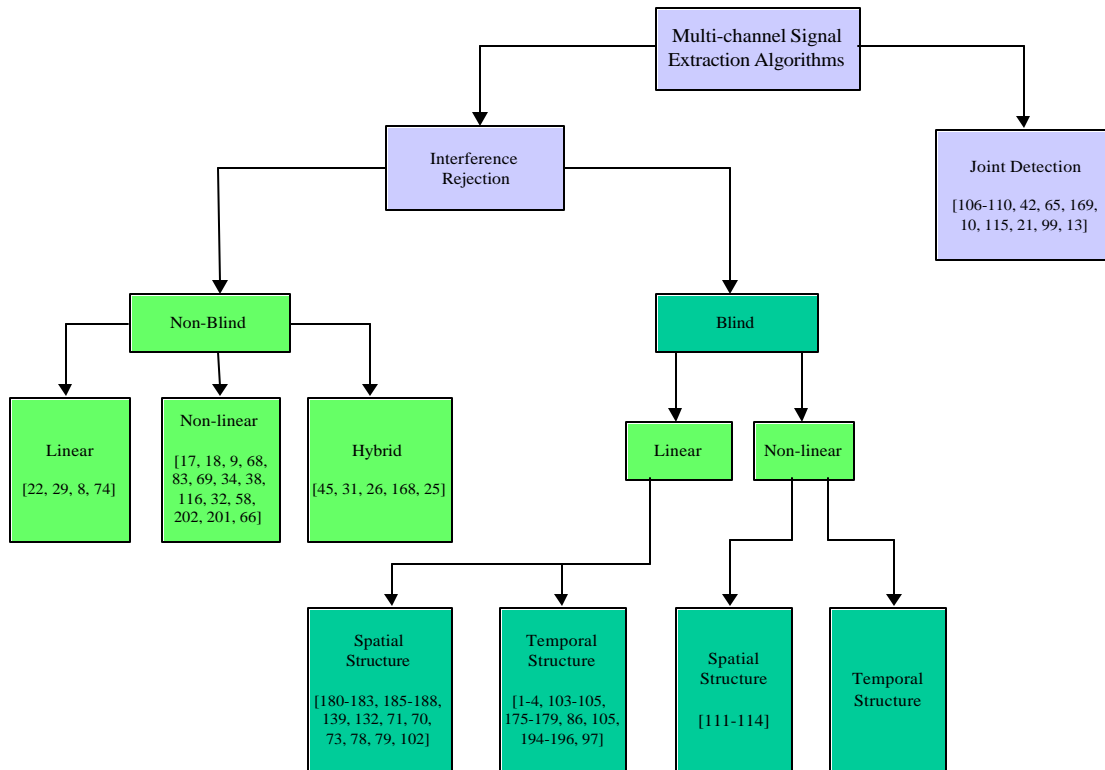


Figure 4.7: Chart showing the breakdown of the multi-channel signal extraction algorithms.

4.2.1 INTERFERENCE REJECTION TECHNIQUES

4.2.1.1 NON-BLIND TECHNIQUES

Non-blind algorithms require the use of training sequences to estimate the channel. Although the use of training sequences greatly simplifies the channel estimation problem, exploiting them can be difficult when interfering users transmit asynchronously. Non-blind interference rejection techniques are broken into linear, non-linear, and hybrid categories. Linear interference rejection tends to break down in overloaded environments. In the literature, several complete solutions for contemporary cellular systems have been reported that account for difficult problems such as synchronization. Non-linear interference rejection algorithms have not been applied to space division multiple access (SDMA) systems. However, they do provide a means for reducing interference from adjacent cells. Hybrid linear/nonlinear techniques have been proposed that try to exploit the strengths of each approach.

4.2.1.1.1 Linear Techniques

In the literature, linear signal extraction techniques can be classified as space-only processing techniques and spatio-temporal techniques where the antenna weights are optimized using MMSE criterion. The goal is to maximize the output signal-to-interference-plus-noise ratio (SINR).

Winters [22] proposes an adaptive beamforming algorithm for signal acquisition in IS-54 digital radio systems. The author shows that the DMI adaptive algorithm has a much faster convergence and better interference suppression capabilities than the LMS algorithm.

The authors of [29] studied the suppression of ACI, CCI and ISI from using linear zero-forcing equalizers/combiners that use antenna arrays with T_s -spaced tapped delay lines where T_s is the symbol period. The linear equalizer puts T_s -spaced zero crossings in the time-domain to reject ISI at the sampling instances, and the linear beamformer steers nulls in the direction of the interfering signals.

Separation of cochannel IS-54/136 signals using beamforming and linear equalization is considered in [8, 74]. Unlike many other algorithms in literature, these papers put emphasis on *asynchronous* TDMA frames. The authors show that, in a bursty TDMA format, the frames of the users are not perfectly aligned. As a consequence, interference may not overlap the training

sequence of the current slot, and thus the optimal beamformer solution is no longer valid for that particular interferer. The authors propose a frame synchronization procedure followed by a *sequential* separation algorithm where the sources are captured and removed sequentially via several stages of partial beamforming and signal cancellation. Frame synchronization is achieved by locating the peaks in the cross correlation of the beamformer outputs with *modified* training sequences. The beamformer weights are updated using LS criterion, and ISI equalization is carried out using a fractionally spaced linear equalizer. The algorithm can effectively separate several users however its performance is limited by the linear beamformer, i.e., as long as the number of cochannel users does not exceed the number of antenna elements since a linear beamformer (M element array) can null out up to $M-1$ users.

4.2.1.1.2 Nonlinear Techniques

Many signal extraction algorithms concatenate linear array processing with nonlinear temporal processing such as DFE and MLSE. In general, nonlinear adaptive array processing techniques perform better than the aforementioned linear techniques, especially in severe multipath fading environments.

Lindskog *et. al* investigate the use of spatial and temporal equalization in the presence of multipath and co-channel interference using multiple beamformers followed by a DFE [17, 18]. Simulations show that this equalizer has good interference cancellation properties given a large number of antenna elements.

In [9], Lee *et. al* provide a complete solution to the frame synchronization problem in GSM slot structure as well as formulating a co-channel signal separation algorithm similar to [8, 74]. After frame synchronization is achieved, co-channel signals are separated using successive beamforming and signal cancellation. DFE is then used to suppress the *induced* ISI (Gaussian pulse shape in the GMSK modulator) and to demodulate the data. The number of separated users is again limited by the array size due to the linear beamforming operation.

MLSE based adaptive antenna array processing algorithms attempt to estimate the channel response for each signal as well as the covariance matrix of the impairment. They then use these estimates in its branch metric to search for the most likely desired transmitted sequence. Several authors have investigated the use of MLSE for interference rejection [16, 32, 34, 38, 68, 69, 83, 116, 202]. They differ in both their assumed operating environment and the calculation of the

path metric for the Viterbi algorithm. In all MLSE approaches, interference is treated as additive Gaussian noise. In such scenarios the MLSE algorithm tries to reject interference and demodulate the SOI.

MLSE techniques can be broken into two major approaches in calculating the path metric: metric combining (MC), and interference rejection combining (IRC). MC assumes that the interference is spatially uncorrelated (i.e., the interfering signals come from any direction). In such an environment, the branch metric for the Viterbi Algorithm is just the sum of the branch metric for each antenna. IRC makes no spatial assumption about the interference environment. Hence, the impairment (CCI + AWGN) covariance matrix must be estimated along with the SOI's channel.

Metric combining is treated in [68, 69, 83]. Metric combining performs well when different antennas experience different fading processes but there is no interference present. Interference Rejection Combining, described in [34], [38], and [116], was developed for the current US Digital standard employing $\pi/4$ -DQPSK. In [38, 39], only the temporal correlation of the interference over a symbol interval is accounted for. In [116] temporal correlation of the interference beyond a symbol interval is accounted for. In both, practical considerations including symbol, phase, and frequency synchronization are also accounted for. An example for the European digital standard, GSM, is provided in [58]. In [202], the authors compare several equivalent architectures for IRC. The performance of the multi-channel MLSE detection techniques requires very accurate channel estimation. In [32], Bottomley and Molnar develop a low-complexity approach to cancel interference *prior* to channel estimation. This *pre-cancellation approach* is obtained through a series of approximations of the Kalman filtering approach [174]. However, the performance of this algorithm is limited to very low Doppler spreads, e.g. less than 20-Hz Doppler spreads.

Any MLSE technique is susceptible to errors in the channel state information (CSI). In [201], the authors show that imperfect CSI can create a floor in symbol error probability. Finally, in [66] Sheen and Stüber propose and analyze joint MLSE equalization and decoding of trellis-coded modulation employing a diversity array.

In [39, 116], neither MC nor IRC can reject more users than elements. This further supports the hypothesis that joint detection separates the SOI from interference better than interference rejection.

4.2.1.1.3 Hybrid

Interference-rejection MLSE processors treat CCI as either colored or spatially uncorrelated (white) Gaussian noise. The problem with treating CCI as AWGN is that MLSE performance becomes highly interference limited, i.e., the MLSE makes no use of the interference covariance properties by completely ignoring the temporal correlation properties of the CCI, which hampers the performance in high interference environment. On the other hand, some MLSE processors try to account for the correlation properties of the CCI by treating CCI as colored noise. This is done by incorporating the impairment covariance matrix within the Viterbi Algorithm. This approach is computationally complex since it requires matrix inversions at each state of the trellis. One solution to this problem is to cancel CCI before doing MLSE equalization, i.e., whiten the signal. Thus, many authors have proposed a hybrid approach: a linear space-time MMSE processor to cancel the CCI cascaded with a non-linear MLSE processor to mitigate ISI. This is illustrated in figure 4.8.

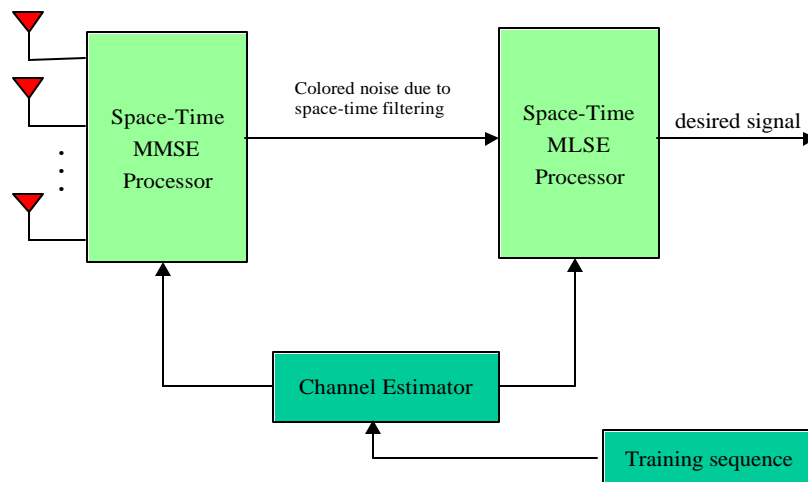


Figure 4.8: Linear ST-MMSE beamformer is concatenated with a nonlinear ST-MLSE processor. The linear beamformer attempts to cancel the interference whereas the following ST-MLSE processor gets rid of the ISI.

Liang and Paulraj developed a two stage CCI/ISI canceller for a frequency-selective Rayleigh fading GSM environment [45]. The first stage is the CCI canceller where antenna array weights are updated using the space-time MMSE criterion. The noise at the output of the first stage is spatially and temporally correlated. Therefore, the Viterbi Algorithm used in the second stage is sub-optimal. The channel is estimated with an RLS algorithm fed by a training sequence. The simulations are run for a two-element antenna array and a single CCI. The results show that the

two-stage canceller outperforms both the single-stage MLSE and single-stage MMSE even at very low carrier-to-interference ratios.

Another type of linear/non-linear array processing receiver is proposed in [31]. The authors develop a space-time MMSE equalizer that can perform burst-to-burst adaptive beamforming as well as equalizing the signal in a GSM system. Both the temporal taps (delay elements) and spatial taps (antenna weights) are optimized jointly by minimizing the MMSE cost function. The Viterbi Equalizer (non-linear equalizer) follows the space-time MMSE equalizer (linear equalizer) and it suppresses the ISI introduced by the GMSK modulation. The simulation results show the effectiveness of the algorithm in suppressing a single CCI signal that has a lower power than the desired signal. It is also shown that the performance of the algorithm degrades if the CCI and desired user have equal powers.

In space-time processing techniques for signal extraction, the MMSE type equalizer spatially and temporally whitens the CCI and then the following DFE or MLSE mitigates the ISI. However, in dispersive co-channel interference environments, the whitening filter requires an infinite span to achieve the optimum performance. Ariyavisitakul *et. al* [26] provide an extensive analysis on the required filter span to achieve near-optimum space-time receiver performance. Through z -transform analysis, they show that the required filter span is proportional to the number of interferers, channel dispersion length, and the input SNR.

A recent paper [25] proposes a joint equalization and interference suppression technique for EDGE systems that uses the concatenation of MMSE type diversity with MLSE equalization. Antenna diversity is used to suppress the co-channel interference in MMSE sense and the subsequent DDFSE [24] equalizer, consisting of a reduced-state Viterbi equalizer and decision feedback, is used to mitigate the ISI. This space-time equalizer provides a soft output to the channel decoder (Viterbi decoder) after deinterleaving. Using the unified infinite filter-length analysis given in [26], the authors show that, at very high SNRs, the optimum front-end filter for an MLSE receiver is equivalent to the optimum feedforward filter of a DFE receiver. Therefore, they train the space-time equalizer (antenna diversity plus the DDFSE equalizer) as if it was a DFE using the MMSE criterion. Weights are adaptively updated using the training sequences based on the RLS algorithm. The MMSE criterion reduces the complexity of the space-time equalizer training and guarantees convergence. The algorithm is tested with 2 antennas in the

presence of a single interferer and very low Doppler spread. The SNR and SIR performance of the receiver is shown to improve as the number of training symbols and the number of prefilter taps increase.

4.2.1.2 BLIND TECHNIQUES

Blind algorithms must extract a signal by exploiting properties that are specific to the SOI. These properties may include constant modulus properties, the finite alphabet properties, or cyclostationary properties.

In Section 4.1.1.2, we have already discussed the issue of signal capture with a blind processor. In Space Division Multiple Access (SDMA) systems, another issue arises. When a blind processor is trying to extract signals solely on their signal properties, there is no way to distinguish between signals of the same type. Hence, there is no guarantee that the j^{th} user will appear on the output of j^{th} output port of the signal processor. This is called the *port shuffle problem* [1, 106]. In digital systems, the port shuffle problem can often be solved by searching for some user id, e.g., CDVCC in a TDMA slot, in the demodulated data. No easy solution exists for analog modulated systems.

4.2.1.2.1 Linear Techniques

The majority of blind techniques in the literature are based on linear space-time filtering. Although the filter update algorithm is often highly non-linear, the filtering operation that estimates the signal, is itself, a linear operation. Regardless of the non-linear nature of the adaptive algorithm, if the end convergence is a linear time invariant space-time filter, the blind algorithm cannot perform any better than the optimum linear time invariant solution. Again, it is well known that a linear STAP breaks down in overloaded environments regardless of the adaptive algorithm used. Nevertheless, we include a description of a variety of blind techniques to illustrate how blind signal extraction is possible.

4.2.1.2.1.1 SPATIAL STRUCTURE

These techniques involve estimation of the direction-of-arrival (DOA) of the signals. When no training sequence is applied, the channel, which contains the array steering vector and multipath components, has to be estimated blindly. In the case of no multipath, array steering matrix that contains the DOA of all the incident signals is the quantity to be estimated. The estimated DOAs can then be fed into a beamformer or a signal canceller to extract the desired signals as shown in figure 4.9.

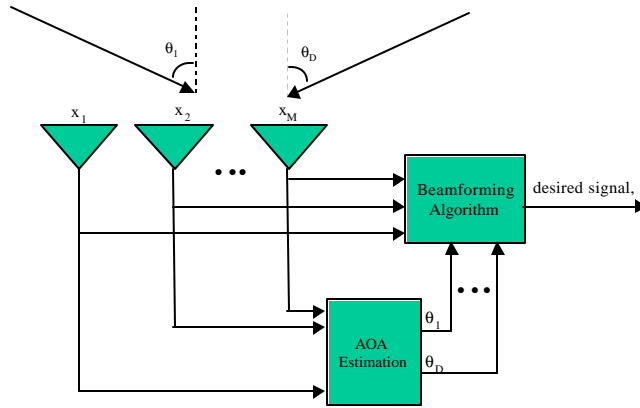


Figure 4.9: Application of DOA estimation to beamforming. The DOA estimator estimates the array steering vector of each incident signal waveform. The estimated DOAs are then used by the following beamformer or another type of signal canceller to extract the desired waveform.

The earlier *conventional methods* for DOA estimation developed by Capon [180, 181] exploit neither the nature of the received signal model nor the statistical model of the noise. However, these methods fail to estimate the DOAs of correlated signals.

Subspace methods on the other hand, exploit the structure of the noise and signals. These methods are based on the eigen-decomposition of the sample covariance matrix. The Multiple Signal Classification (MUSIC) algorithm and its derivatives [139, 182, 183] are widely used for DOA estimation in non-coherent signal environments. Some other modifications are proposed for the MUSIC algorithm in coherent signal environments. These techniques are called *spatial smoothing techniques* [185, 186, 187, 188]. The main drawback of MUSIC related algorithms is that they all require an exhaustive search through the entire array manifold to estimate the DOAs. Further, the array manifold must be known, thereby requiring accurate array calibration. The Estimation of Signal Parameters via Rotational Invariance Techniques (ESPRIT) algorithm greatly reduces the computation complexity of the MUSIC based algorithms [132]. ESPRIT gets

rid of the exhaustive search and it does not require precise array calibration. However, ESPRIT imposes some restrictions on array configuration. The reader is referred to Godara [70, 71] for an extensive tutorial and survey on different DOA estimation algorithms.

A recent approach in DOA estimation has been to exploit cyclostationarity properties of the incident signals. Different signals have different (conjugate) cyclic frequency sets $\{\mathbf{a}\}$ and by selecting an appropriate \mathbf{a} desired signals can be easily extracted from interfering signals and noise. In literature, we can find several papers that propose DOA estimation algorithms, which exploit the cyclostationarity properties of digital communication signals [73, 78, 79, 102]. These papers attempt to blindly estimate the number of signals-of-interest (SOIs) as well as their DOAs in the presence of *overloaded* array conditions. However, they all make several assumptions about the nature of the desired and interfering signals as well as the notion of overloaded environments:

- SOIs exhibit spectral coherence at *different* cyclic frequencies than the CCIs and noise.
- The SOIs' cyclic frequencies have to be either known *a priori* or estimated.
- The total number of SOIs should be less than the number of antenna elements (although the total number of interfering plus desired signals can be more than the antenna elements) in order to extract all the SOIs from the interference environment.
- Array geometry is restricted, i.e. usually applicable to uniform linear arrays (ULA).

Simulation results of these algorithms show that an M -element antenna array can extract the DOAs of d_s SOIs (assumed to exhibit cyclostationarity at *known* cyclic frequencies) in the presence of d_i interfering signals as long as $d_s < M$. The promising result is that, total number of incident signals ($d_s + d_i$) can be larger than M , which is an overloaded array situation. However, in the presence of interfering signals that have the same temporal characteristics as the desired signals, the above stated assumptions may not be applicable.

4.2.1.2.1.2 TEMPORAL STRUCTURE

4.2.1.2.1.2.1 CM PROPERTY

The most popular blind algorithm that exploits the constant modulus property of the incident signal waveforms is the classical CMA technique. However, classical CMA techniques use Stochastic Gradient-Descent approach to minimize the nonlinear cost function and therefore

suffer from slow convergence. Gradient-descent based CMA techniques are proposed in [104, 105, 175, 176] where a multiple-stage Constant Modulus (CM) array operates as a blind adaptive beamformer for signal extraction. Each stage consists of a weight-and-sum beamformer adapted by CMA and a signal canceller adapted by LMS algorithm. As with all beamforming algorithms, the signal extraction ability is limited by the number of antenna elements employed in the linear beamformer.

CMA based algorithms suffer from inherent signal capture problem as shown in Section 4.1.1.2. Several papers have been written to overcome this problem by applying multiple CMA beamformers to the same observed data and extract all CM signals in the environment. The outputs of these beamformers can further be processed to select the desired signal [2, 4, 152, 177, 178, 179]. However, signal extraction performance of all these algorithms is limited by the antenna array size.

A very effective fast convergence CMA method based on least squares minimization approach is introduced by Agee [103]. This so-called LSCMA algorithm is a block update technique, which uses an alternating projections approach to minimize the CMA cost function. The approach first projects the received signal onto the set of signals which has the desired property, and then finds the closest approximation to this projected signal that can be obtained using a beamformer. LSCMA technique is utilized in Agee's Multi-Target Least Squares CMA (MT-LS CMA) [152] to blindly adapt a narrowband multistage beamformer. A block diagram of the MT-LSCMA is given in Figure 4.10. The MT-LSCMA algorithm employs the *Gram-Schmidt Orthogonalization (GSO)* technique to separate the incoming source signals onto individual output ports at the start of adaptation, thereby preventing the weight vectors in different ports from converging to the same beam pattern. After the algorithm converges, a *sorting procedure* is carried out to relate the output ports to each user's signal with the attempt to reduce the port shuffle problem. The simulation results show that, using a four-element circular array MT-LSCMA can separate a weak FSK signal from three strong FM interfering signals (*fully loaded array*).

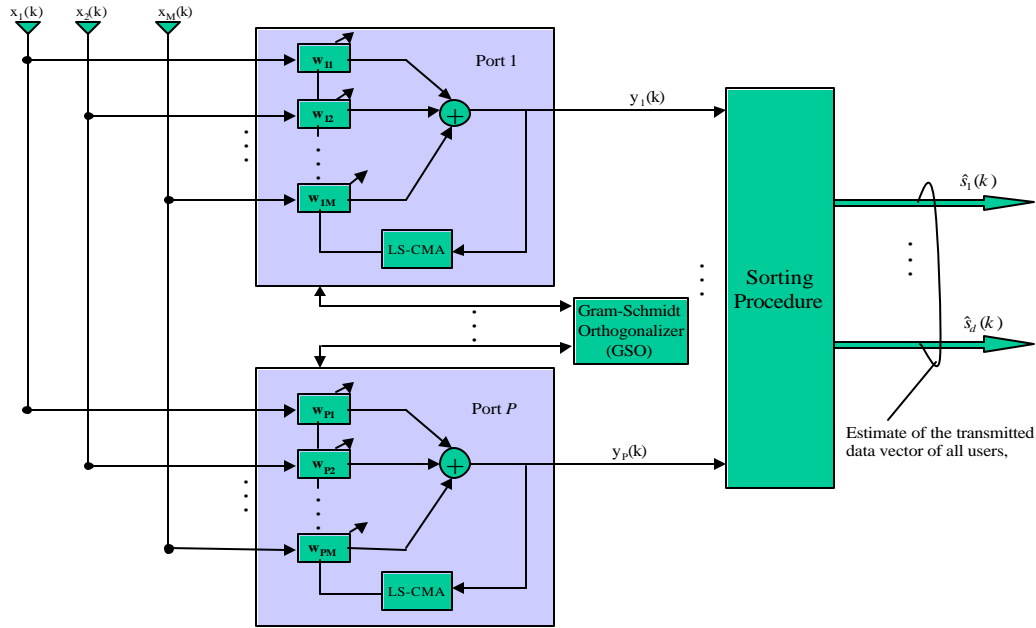


Figure 4.10: Multi-Target LS-CMA adaptive array. M is the number of antenna elements and it is usually equal to the number of ports, i.e. $M=P$. P different beamformer weights are adapted independently by LS-CMA technique. GSO orthogonalizes the weight vectors so that each port corresponds to a unique weight vector. Sorting procedure relates the port outputs to each user's signal. If number of users, D , is larger than the number of elements (or ports), then one output port may contain the signals of several users

Another blind beamforming algorithm, *Analytic CMA (ACMA)*, is proposed in [2]. ACMA uses a subspace approach to solve the signal capture effect and slow convergence of traditional CMA. ACMA attempts to simultaneously demodulate all CM signals impinging on the antenna array. However, it is very computationally complex, i.e. the most efficient form has complexity given by $O(9D^4n+36M^2n)$, where D is the number of signals of interests, n is the data collect length, and M is the number of elements. ACMA algorithm is derived for high-SNR conditions and the estimates of the ACMA beamformer are asymptotically biased. Improvements on this algorithm, in the presence of low SNRs, are presented in *Weighted ACMA (W-ACMA)* by Van der Veen [3]. W-ACMA uses a *weighting* scheme to whiten the noise and remove the bias.

The algorithms presented in [2, 4, 77, 152, 177, 178, 179] can mitigate the signal capture effect; however they are computationally complex. Alternative techniques have been proposed to mitigate the signal capture effect and port shuffle problem by exploiting the second order cyclostationarity of the desired signals [194, 195, 196]. These algorithms find their roots in the SCORE algorithm developed by Agee *et. al* [97]. However, SCORE-related algorithms are known to have a slow convergence as well as poor performance in the presence of coherent

multipath. Biedka and Kahn [1] propose three different methods for constraining a CMA beamformer to extract a cyclostationary signal by combining SCORE techniques (to discriminate against interference) with CMA techniques (both gradient-descent based and least-squares based) to mitigate coherent multipath.

4.2.1.2.1.2.2 FA PROPERTY

Finite Alphabet (FA) property thought to be much more powerful than the constant modulus property, but is more difficult to exploit. Some examples of digital signals possessing the FA property were given in Chapter 3 of the thesis.

Talwar *et. al* [106, 107] developed two powerful signal extraction techniques based on FA property of the signals. Both of these algorithms iteratively estimate the transmitted user symbols and the channel. Of these algorithms, Iterative Least Squares with Projection (ILSP) separates multiple user symbols via a ML beamformer whereas the other algorithm, Iterative Least Squares with Enumeration (ILSE) is a true ML joint detection algorithm. Both ILSP and ILSE, are treated extensively in Chapter 5 of the thesis. More computationally efficient but sub-optimal implementations of ILSP are given in [108, 109, 110]. Algorithms that account for ISI are presented in [42] and [65]. In both, ISI and cochannel interference are modeled with a set of linear equations. Implicit in both algorithms is the assumption of a linear beamformer. Van der Veen and Paulraj [169] combine the CM property with the FA property of the signals and propose a blind channel identification algorithm using *Real ACMA* (special case of the ACMA technique applied to real signals) to initialize the ILSP algorithm. The authors use this blind channel algorithm to carry out space-time linear beamforming for the linear approximation of GMSK signals.

4.2.1.2.1.2.3 CYCLOSTATIONARITY PROPERTY

In Section 4.1.1.1.2, we have shown that a LTDAF processor can perform interference rejection by exploiting the cyclostationary of digitally modulated signals. Such processors need training sequences to update the filter coefficients. However, cyclostationarity is also an exploitable property for blind processing. Class of blind beamforming algorithms called Spectral Self-Coherence Restoral (SCORE) algorithms [97] update a beamformer by attempting to restore the spectral correlation at a known cycle frequency. SCORE algorithms are powerful because they applicable to any cyclostationary signal (not just CM or FA). In addition, SCORE makes no

assumption about the array manifold or the interference environment. In particular, the performance of an algorithm called cross-SCORE [97] has been shown to converge to that of a non-blind optimal SINR beamformer if the number of interfering signals with the same spectral correlation frequencies in the environment does not exceed the number of elements. The convergence of the algorithm is highly sensitive to the spectral correlation coefficient and data collection time. The data collect time should be chosen to be large enough to discriminate between interfering signals with closely spaced spectral correlation frequencies but small enough to assure signal coherence.

4.2.1.2.2 Nonlinear

Nonlinear DOA estimation and signal extraction techniques have been analyzed by Mendel *et. al* in their novel blind beamforming algorithms based on fourth-order cumulants [111, 113]. The nonlinearity is introduced through the use of *virtual antenna elements* for beamforming. This novel idea is first introduced in [111], where the authors extended the classical ESPRIT algorithm to develop a new DOA estimation technique called *Virtual ESPRIT Algorithm (VESPA)*. The goal is to increase the effective aperture of an arbitrary antenna array by introducing *virtual elements* to the already existing arbitrary antenna array of M real elements as illustrated in figure 4.11. The VESPA algorithm is shown to resolve the DOAs of six independent uncorrelated BPSK sources with a three-element array. The authors modified the VESPA algorithm to perform direction finding for coherent sources in [112]. This so-called *Extended VESPA (EVESPA)* algorithm requires the use of a uniform linear array as a subarray. The EVESPA algorithm is shown to estimate the DOAs of 20 multipath components of five independent BPSK sources given a 14-element array. Finally, in [113] the authors extended the cumulant-based beamforming algorithm developed in [111] to coherent multipath propagation scenarios. Simulations show that the non-linear cumulant-based beamformer with four antenna elements can recover a total of 14 multipath components of four closely spaced coherent BPSK sources. These virtual element based beamforming algorithms model the sources as non-Gaussian, whereas the noise is modeled as a Gaussian random process with unknown covariance matrix. The authors show that fourth order cumulants are capable of suppressing both white and colored Gaussian noise with arbitrary covariance. However, their applicability to practical

systems is an open issue due to their higher complexity and slower convergence compared to the second-order based signal extraction techniques.

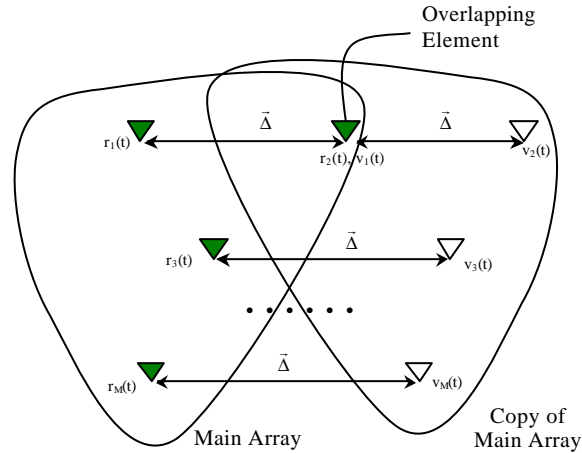


Figure 4.11: VESPA creates a copy of the main real array and forms a virtual array of M sensors displaced in space with a known displacement vector. Only one pair of sensors forms a doublet rather than a full-copy of the array (this is done in ESPRIT algorithm). This results in two subarrays: one with M real sensors the other with M virtual elements. Due to the overlap of one virtual and one real element (forms the doublet), the total aperture consists of $2M - 1$ sensors.

4.2.2 JOINT DETECTION TECHNIQUES

There have been few contributions geared specifically towards narrowband signal extraction in overloaded array environments. One very interesting paper by Grant and Cavers [13] analytically demonstrates that overloaded array processing is possible with a highly complex Joint MAP (JMAP) algorithm. Figure 4.12 presents a block diagram of the MAP receiver. A number, D , of cochannel interferers impinge on the array from different angles of arrival. The array is matched filtered and sampled at some integer multiple of the baud rate. The sampled array signals are input to a multi-user detector, which attempts a simultaneous MAP estimate of all users. Inspired by the work of Verdu in CDMA multi-user detection [157, 158, 197], Grant and Cavers derived a closed form expression for a tight upper bound on error probability for synchronous users in fading channels. The derivation accounts for the possibility of imperfect channel estimates. Their results predict that a two-element array, in moderate SNR environments, can successfully demodulate up to six equal power users, even with an imperfect channel estimate. This prediction outperforms results achieved with linear space-time processing. Although these results were found under the synchronous user assumption, it has been found in [35, 203] that asynchronous users will help improve the JMAP's performance. No

upper bound on error probability has been found for the asynchronous user case in the presence of multipath.

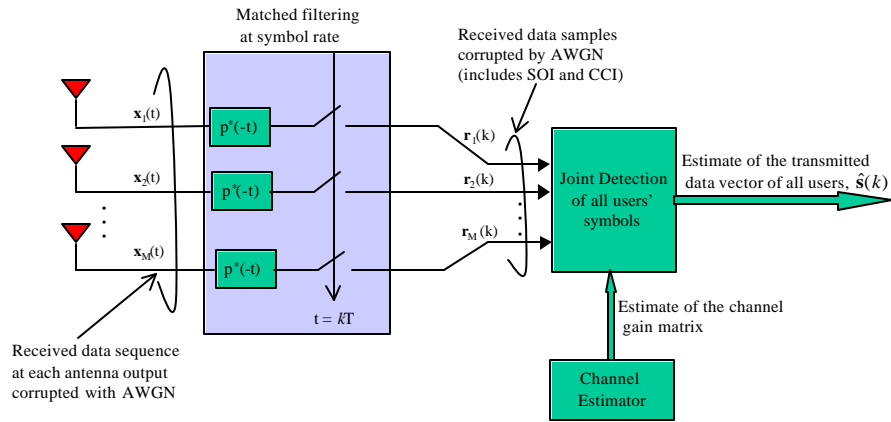


Figure 4.12: Multi-user receiver employing an M antenna array. Transmitted symbols of all users are separated and demodulated jointly using Joint-MAP (JMAP) algorithm. Channel estimates are obtained through the use of training sequences or pilot symbols (for CDMA type systems).

In Section 4.1.1.1.3, we have mentioned non-linear interference rejection algorithms based on Single Input Single Output (SISO) DFE processor structure. A novel DFE structure is introduced in [21, 98, 99]. This structure, so-called Multi-user DFE (MU-DFE), is comprised of a Multiple Input Multiple Output (MIMO) feedforward filter for simultaneous separation of multiple users and a MIMO feedback filter for multipath equalization. An extensive analysis of this MMSE joint detector structure can be found in Chapter 5.

Finally, several papers coupled MLSE algorithm with antenna arrays to carry out joint detection as well as equalization. One important algorithm is the multi-element version of ICE [35, 203], which was discussed in Section 4.1.2. The authors show that for equal-power synchronous users, the ambiguity problem present in the single-element receiver is not present in the two-element receiver. Finally, the performance of the algorithm was found to be sensitive to Doppler shift: as the channel changes more quickly, it becomes more difficult to track. The authors also show that, in the case of no ISI and perfectly synchronous users, the algorithm boils down to an exhaustive symbol-by-symbol search to minimize the ML cost function. This is exactly how ILSE [106, 107] works and it will be shown in Chapter 5 that ILSE provides a baseline for signal extraction in overloaded scenarios.

ILSE assumes that the interference is spatially uncorrelated. In a realistic multi-user environment, there may be a large number of low power interferers coming from a specific

location, which induces spatial correlation among the users. Agee [10] developed a blind maximum likelihood receiver for direction finding (DF) in dense, spatially correlated interference scenarios. The algorithm was found to successfully demodulate up to ten cochannel CPFSK signals with a four element circular array.

4.3 SUMMARY

In the first part of this chapter, we have described many examples of interference canceling (both interference rejection and joint detection) receivers for single element receivers. Literature suggests that time varying and non-linear receivers will perform better than less complex linear solutions. In particular, joint MAP receiver is guaranteed to separate co-channel signals with a lower probability of symbol error than any other receiver. This receiver structure suggests that the capacity of an M -element array is much greater than M , i.e., overloaded array processing is possible for narrowband signals. However, the computational complexity of a JMAP receiver increases exponentially with the number of users, which results in an impractical receiver structure. This motivates a search for sub-optimal receivers that might approach the JMAP's performance. In this survey, we have described a host of array processing techniques. Among those, linear STAP techniques break down in overloaded environments due to the array size limitations. The success of time-varying interference suppression techniques, such as FRESH filtering for single element receivers, suggests that this may also be a successful approach for overloaded antenna arrays. However, for overloaded homogenous environments, joint detection schemes are expected to be the most successful. The only drawback of ML joint detection receivers is the prohibitive complexity for a large number of users. No practical implementation of an overloaded array processor for a large number of narrowband users has been found in the literature.

The following chapter provides an extensive analysis of three multi-user detection algorithms that were found to be candidate "promising" approaches for signal extraction in overloaded scenarios.

CHAPTER 5: SIGNAL EXTRACTION ALGORITHMS

This chapter consists of the analysis and simulation results of three different signal extraction techniques: Multi-user Decision Feedback Equalizer (MU-DFE), Iterative Least Squares with Projection (ILSP) and Iterative Least Squares with Enumeration (ILSE). In the sequel, we discuss the computational complexity and performance tradeoffs of these algorithms in regards to signal extraction in overloaded array scenarios. In all of these algorithms, the number of elements and number of users are denoted by m and d , respectively. In addition, a benign channel model is assumed since the mere purpose of analyzing the algorithms was to see whether they perform well in extracting more near-equal power user signals than the number of antenna elements. Therefore, the following assumptions are made in simulating the performance of these algorithms:

- Narrowband user signals with no excess bandwidth
- Total number of co-channel users are known
- Users are both symbol and frame synchronous
- Additive noise is spatially and temporally uncorrelated and has a zero-mean Gaussian distribution
- Channel is time-invariant over the duration of a TDMA burst, i.e. Doppler effects and fading are ignored

System analysis in chapter 2 shows that, received signals on the airborne receiver are subject to high Doppler shifts (~300-600 Hz). In addition, the signals would experience flat fading since the delay spread in an airborne channel is much less than the symbol period for a TDMA-type signal. The fading is expected to have a Rician distribution due to a strong Line-of-sight (LOS) component for each user signal. A more complete airborne channel model that incorporates Doppler effects, flat fading characteristics and phase offsets is an area of future work.

5.1 MULTI-USER DECISION FEEDBACK EQUALIZER (MU-DFE)

5.1.1 INTRODUCTION

The Multi-user DFE is a low-complexity signal extraction approach for separating multiple co-channel users impinging on an antenna array as well as equalizing the ISI for each user. It consists of an m -element antenna array followed by a space-time multiple-input multiple-output

(MIMO) feedforward filter with n_s taps and a MIMO feedback filter with n_q taps. The structure of the processor is shown in Figure 5.1.

Signal extraction is carried out by the MIMO feedforward filter, which has $m \times n_s$ degrees-of-freedom (DOF). Our initial goal was to see whether we can exploit this increased DOF in extracting more signals than number of elements, i.e. form $(m \times n_s) - 1$ nulls with the MIMO feedforward filter. On the other hand, the purpose of the MIMO feedback filter is to cancel ISI in every user symbol simultaneously.

5.1.2 CHANNEL AND SIGNAL MODELS

This algorithm assumes a stationary *temporal* multipath channel. Temporal multipath condition occurs when the scatterers are located very close to the mobiles so that multipath components are simply the delayed versions of the LOS signals coming from the same angle-of-arrivals.

The stationary multipath channel matrix for the i^{th} multipath component of each user signal is given by:

$$\mathbf{H}_i = \begin{bmatrix} \mathbf{a}_{1i} & 0 & \cdots & 0 \\ \vdots & \ddots & \ddots & \vdots \\ 0 & 0 & \cdots & \mathbf{a}_{di} \end{bmatrix} \begin{bmatrix} \mathbf{a}_1(\mathbf{q}_1) \\ \vdots \\ \mathbf{a}_d(\mathbf{q}_d) \end{bmatrix} \quad (5.1)$$

where \mathbf{a}_{ji} is the complex Gaussian channel gain of the i^{th} multipath component of the j^{th} user, and $\mathbf{a}_j(\mathbf{q}_j)$ is the steering vector for the j^{th} user signal with an AOA of \mathbf{q}_j .

For the Multiple Input Multiple Output (MIMO) model, we define the following signal vectors:

$$\mathbf{s} = [s_1(k), s_2(k), \dots, s_d(k)]^T, \quad \mathbf{v} = [v_1(k), v_2(k), \dots, v_m(k)]^T, \quad \mathbf{x} = [x_1(k), x_2(k), \dots, x_m(k)]^T \quad (5.2)$$

where \mathbf{s} is the symbol vector for d users, \mathbf{v} is the complex valued Gaussian noise samples at m antenna elements. The received signal vector \mathbf{x} at each snapshot of time, k , is then defined by:

$$\mathbf{x}(k) = \mathbf{H}_0^T \mathbf{s}(k) + \cdots + \mathbf{H}_i^T \mathbf{s}(k-i) + \cdots + \mathbf{H}_L^T \mathbf{s}(k-L) + \mathbf{v}(k) \quad (5.3)$$

where k denotes the time index, $\mathbf{s}(k)$ represents the LOS symbol vector, i.e. $i = 0$, and $\mathbf{s}(k-L)$ represents the L^{th} multipath symbol vector.

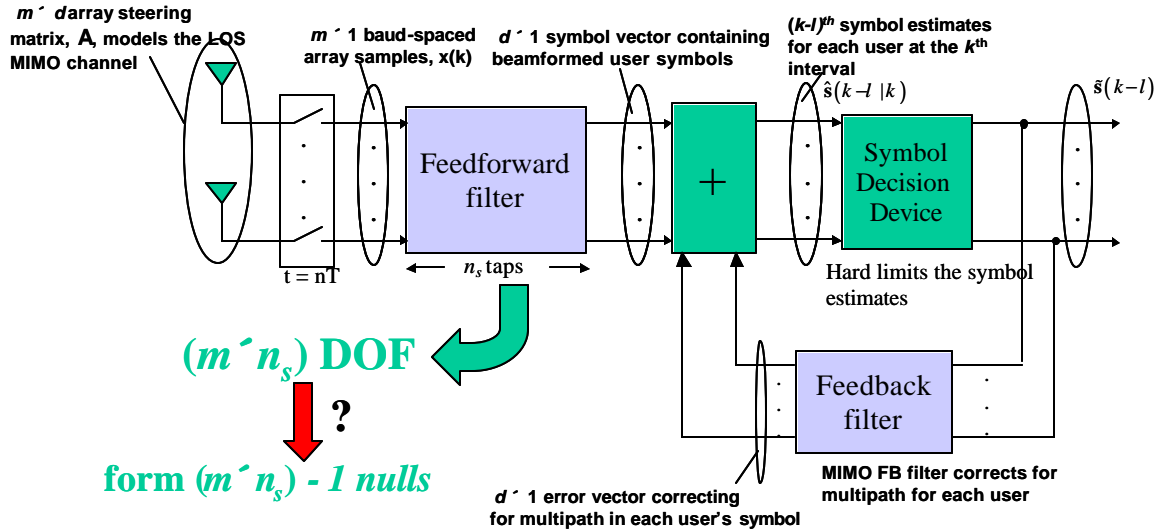


Figure 5.1: Multi-user detector employing a multiple input multiple output (MIMO) Decision Feedback Equalizer (DFE). The MIMO feedforward filter acts as a beamformer/equalizer. Symbol decision device is a hard limiter whose output (hard limited symbol estimates for the interference) is fed back using a MIMO feedback filter. The MU-DFE incorporates a decision delay denoted by l in such a way that hard symbol estimates of k th symbol of each user are made at the end of the $(k+l)$ th interval.

5.1.3 MIMO FEEDFORWARD FILTER

MU-DFE consists of a feedforward filter with n_s taps. Baud-spaced array output vector is fed to the MIMO feedforward filter whose complex coefficients are expressed by

$$\Theta_S^H = \begin{bmatrix} \mathbf{S}_0 & \mathbf{S}_1 & \dots & \mathbf{S}_{n_s} \end{bmatrix} \quad (5.4)$$

$d \times m$ (n_s+1) $d \times m$ $d \times m$ $d \times m$

The MIMO FF filter serves as a space-time filter. The structure of the MIMO FF filter is shown in figure 5.2. The l th coefficient matrix, \mathbf{S}_l , acts as a bank of optimum SINR beamformer weights as shown in figure 5.3. The purpose of the MIMO FF filter is to simultaneously separate all of the users by forming an optimum SINR beam in the direction of each user. Since the MU-DFE has a decision delay of l symbols, only the $(k-l)$ th symbol of each user is extracted. This is achieved by setting all the coefficient matrices except for the l th matrix, \mathbf{S}_l , to very small numbers, i.e. $\mathbf{S}_n \approx \mathbf{0}$ for $n \neq l$. Therefore, MIMO FF filter acts as a canceller for the users' symbols except for the $(k-l)$ th symbol.

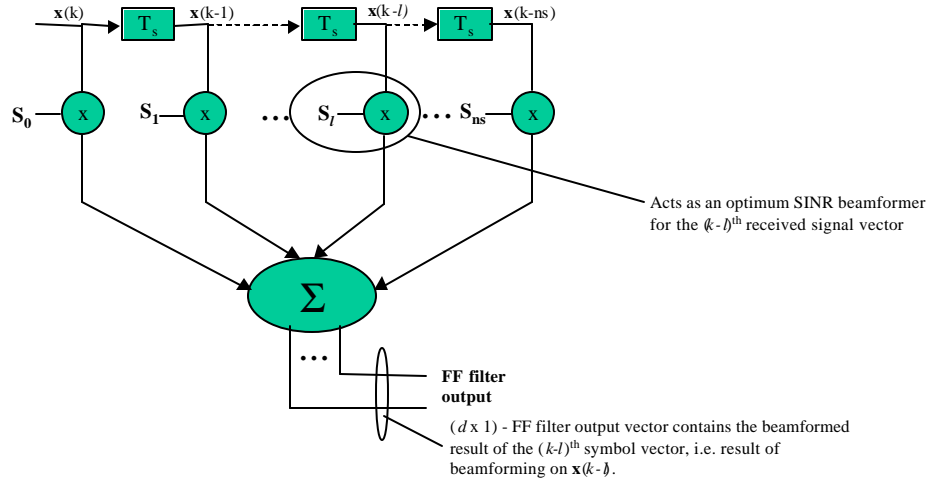


Figure 5.2: Visualizing the MIMO feedforward filter. FF filter has $ns+1$ taps and each tap consists of a $d \times m$ coefficient matrices

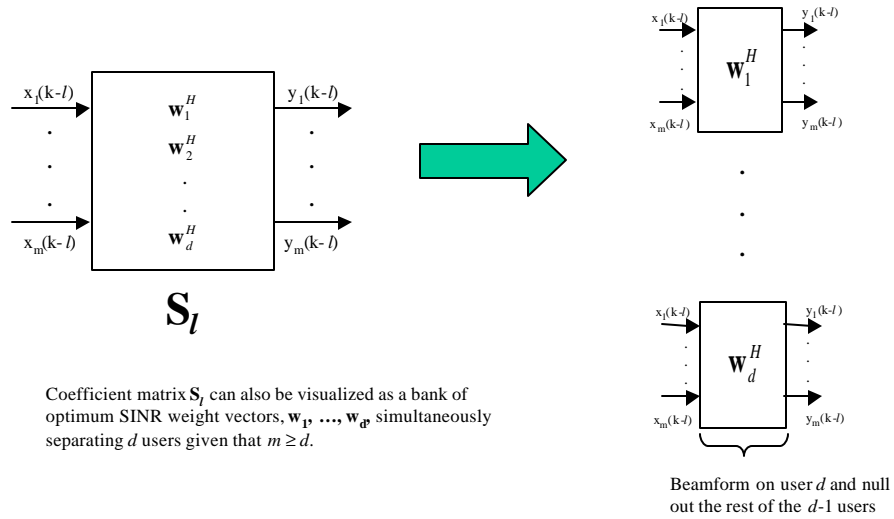


Figure 5.3: Visualizing the MIMO feedforward filter. The l^{th} coefficient matrix, S_l acts as a bank of optimal SINR beamformers for the $(k-l)^{th}$ symbol of each user. The rest of the coefficient matrices are approximately zeros.

5.1.4 MIMO FEEDBACK FILTER

MIMO Feedback Filter (MIMO FB filter) contains nq taps. The processed user symbols at the $(k-l)^{th}$ symbol interval, are delayed by one symbol period and then are fed to the MIMO FB filter whose complex coefficients are expressed by

$$\Theta_Q^H = \begin{bmatrix} Q_0 & Q_1 & \dots & Q_{L+ns-l-1} \\ d \times m & d \times m & \dots & d \times m \end{bmatrix} \quad (5.5)$$

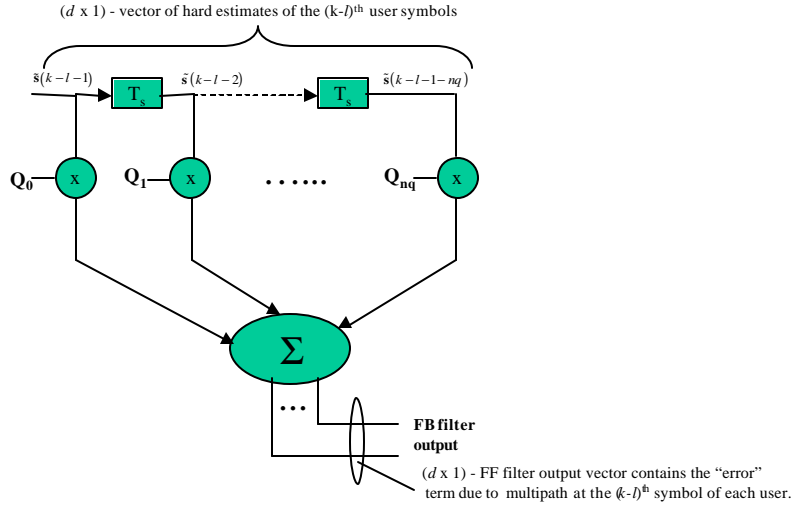


Figure 5.4: Visualizing the feedback filter. FB filter has $nq+1$ taps and each tap consists of $d \times d$ coefficient matrices

MIMO FB filter corrects for the multipath. It feeds back the complex “error” term for each user’s symbol. This error term is then subtracted from the beamformed user symbols at the output of the MIMO FF filter. The FB filter coefficients $\mathbf{Q}_0, \mathbf{Q}_1, \dots, \mathbf{Q}_{nq}$ are designed such that $\mathbf{Q}_n \approx \mathbf{0}$ for $n \geq L$ where L is the channel length.

5.1.5 DESIGN OF THE FILTER COEFFICIENTS

MU-DFE filter coefficients Θ_s^H and Θ_ρ^H are calculated using the MMSE criterion. The cost function to be minimized is the expected value of the squared error between the actual transmitted $(d \times 1)$ symbol vector and its estimate:

$$J = E \left[\left\| \mathbf{s}(k-l) - \hat{\mathbf{s}}(k-l|k) \right\|^2 \right] \quad (5.6)$$

Note that the design of the coefficients are non-adaptive and merely depends on the channel characteristics. The filter coefficients and therefore the channel coefficients are updated at the end of each TDMA slot. The equations used to update the filter coefficients are as follows [98]:

$$(\mathbf{F}\mathbf{F}^H + \mathbf{Y})\mathbf{Q}_S = \mathbf{F}_{pres} \quad (5.7)$$

$$\mathbf{T}_Q = \mathbf{F}_{past}^H \mathbf{T}_S \quad (5.8)$$

where Ψ is an $m (ns + 1) \times m (ns + 1)$ noise covariance matrix and the rest of the matrices are defined as:

$$\mathbf{F}_{tot} = \begin{bmatrix} \mathbf{F}_{fut} & \mathbf{F}_{pres} & \mathbf{F}_{past} \end{bmatrix} \triangleq \begin{bmatrix} \mathbf{H}_0 \cdots \mathbf{H}_L \cdots \mathbf{0} \\ \vdots \quad \ddots \quad \ddots \quad \vdots \\ \mathbf{0} \cdots \mathbf{H}_0 \cdots \mathbf{H}_L \end{bmatrix} \quad (5.9)$$

$\mathbf{F}_{fut} \triangleq$ First dl columns of \mathbf{F}_{tot} ; contains the multipath channel taps for the symbol interval $\{k, \dots, k-l+1\}$.

$\mathbf{F}_{pres} \triangleq$ Columns $dl + 1$ to $d(l+1)$ in \mathbf{F}_{tot} ; contains the multipath channel taps for the symbol interval $k-l$.

$\mathbf{F}_{past} \triangleq$ Columns $d(l+1)$ to $d(ns+L+1)$ in \mathbf{F}_{tot} ; contains the multipath channel taps for the symbol interval $\{k-l-1, \dots, k-ns-L\}$.

The noise covariance matrix is assumed to be non-singular and thus its existence makes the matrix inverse operation in (5.7) always stable and invertible.

5.1.6 SIMULATION RESULTS

Our simulations are based on apriori known 2-tap stationary multipath channel. The users are assumed to have equal powers and noise is assumed to be both spatially and temporally uncorrelated. Both symbol and frame synchronous QPSK modulated data is sent with 200 symbols in each frame. The antenna array is circular array with a radius of 0.25λ . The FF filter length and the decision delay are chosen to be $ns = 8$ and $l = 6$, respectively.

Figure 5.5 shows the performance results for d equally spaced, equal power QPSK users impinging on a 8-element circular array. Performance degradation can be seen as the number of users increase from one to eight. The algorithm can demodulate users at very low SNRs given that the array is underloaded. The algorithm is then tested for different critically loaded antenna array cases, i.e. $m = d$. Figure 5.6 shows the symbol error rate averaged over 100 slots per SNR value. All the user symbols are extracted with good error rates for SNRs higher than 20dB. However, the performance of the algorithm degrades slightly as the number of elements and users increase.

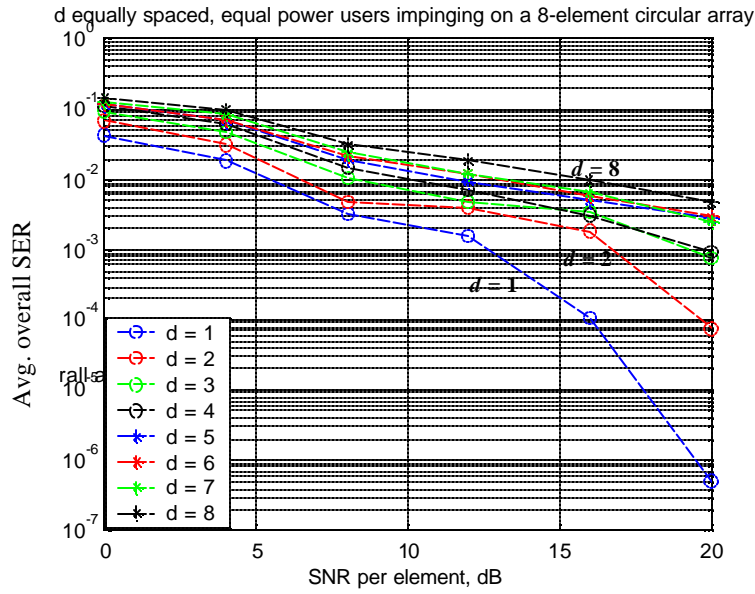


Figure 5.5: Performance of MU-DFE using an 8-element circular array of radius = 0.25λ . The array geometry is kept constant while the number of users impinging on it is increased from 1 to 8. The users are spaced equally with a spacing of 45° . As the number of users increases, the performance of the algorithm decreases. For this simulation, we used $L = 1, ns = 4, l = 3$.

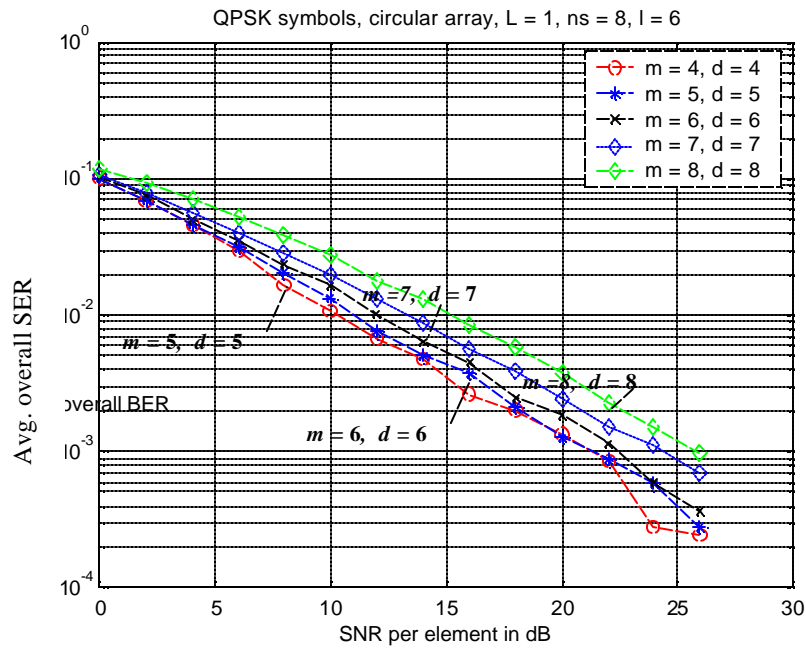


Figure 5.6: Simulation results for the critically loaded case. The user angles are equally spaced from 0° to 360° . Users are assumed to have equal powers, and channel is assumed to be 2-tap stationary multipath channel ($L = 1$) with scatterers impinging on the antenna array from the same direction as the LOS signals.

5.1.7 EFFECT OF CHANGING THE FILTER LENGTHS

The FF filter length, ns , should be chosen to be at least equal to the decision delay. However, the simulations also show that increasing the FF filter length increases the computational complexity but does not increase the performance. The FB filter length results in the optimum signal extraction performance when $nq = L + ns - l - 1$. The FB filter is crucial when significant multipath exists. When there is no multipath, i.e. $L = 0$, all the feedback coefficients become zero and non-linear MU-DFE boils down to a linear Space-time filter. Figure 5.7 shows the performance of the MU-DFE with and without feedback when four equally spaced QPSK users impinge on a four-element circular array. We can see that, the non-linear processor, i.e. MU-DFE with feedback, can adjust to the increasing channel length ($L + 1$), and the performance stays almost the same for increasing L . However, for the case of linear ST-filter, performance starts degrading as the multipath becomes more severe. This is due to the lack of feedback filter that corrects for the multipath.

5.1.8 ANGULAR SPACING OF THE USERS

As shown in Figure 5.6, the algorithm performs well even in critically loaded environments provided that the angular spacing of the users is sufficiently large. The algorithm is also tested for the case of closely spaced users. Figure 5.8 shows the performance of the algorithm when two equal power QPSK users impinge on a three-element circular array. As the spacing gets smaller, the array steering matrix, \mathbf{A} , becomes ill-conditioned. This condition results in a noise enhancement, thereby degrading the algorithm's performance.

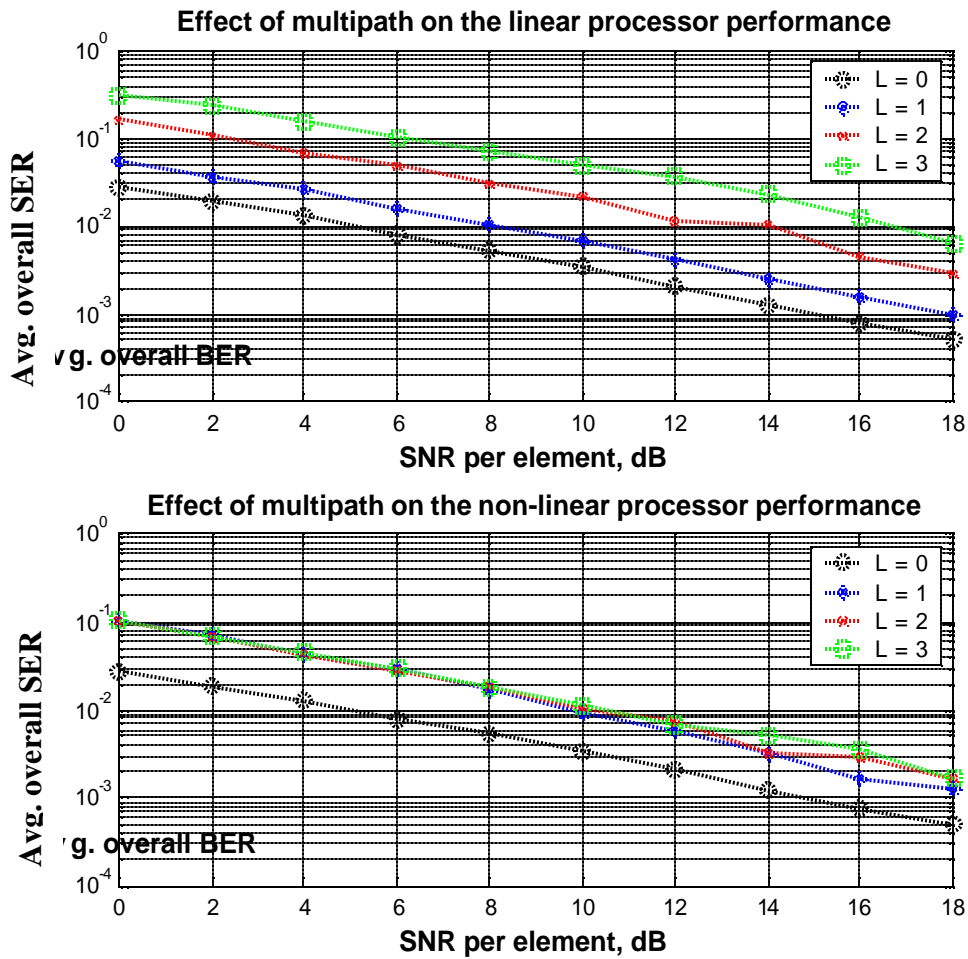


Figure 5.7: The effect of feedback filter on the performance of MU-DFE in a multipath channel. Four equal spaced, equal power QPSK users impinge on a 4-element circular array. The non-linear processor, MU-DFE with feedback, is robust to the increasing channel length, $L+1$. However, the performance of the linear ST-filter, MU-DFE without feedback, decreases with increasing channel length. Non-linear feedback corrects for the severe multipath distortion. For both cases, the feedforward filter was chosen to be of length $n_s = 4$. For the non-linear case, the decision delay was chosen to be $l = 3$.

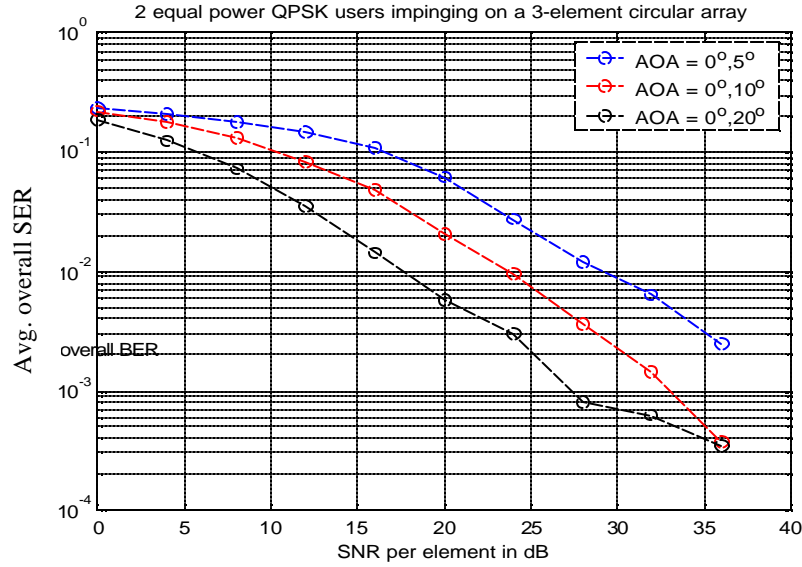


Figure 5.8: 2 equal power QPSK users impinge on a 3-element circular array. Performance degrades significantly as the users are closely spaced.

5.1.9 COMPUTATIONAL COMPLEXITY

Figure 5.9 depicts the computational complexity of the MU-DFE based on the number of complex multiplication required for separating a *snapshot* of d user symbols. The equation for the complexity is given by [98] as

$$\frac{1}{4} m^2 d(l+1)(l+2) + \frac{1}{6} m^3 (ns+1)^3 + m^2 (ns+1)^2 d + dm(ns+1) + d^2 m(L+1)(nq+1) \quad (5.10)$$

Calculate $FF^H + Y$
Factorize $FF^H + Y$
Solve for FF filter coefficients
Equalization of one symbol vector during FF filtering
Solve for FB filter coefficients

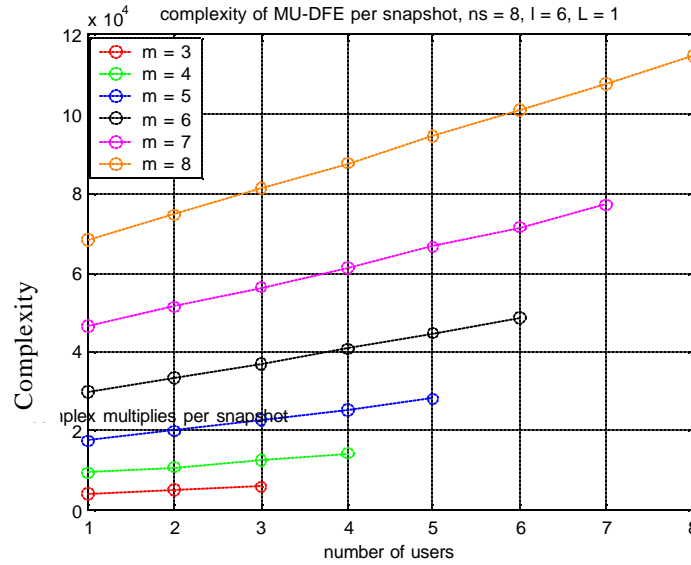


Figure 5.9: Computational complexity of the MU-DFE per snapshot per iteration. The complexity is polynomial in m and d . The complexity is also affected by the FF filter length, ns and channel order, L .

5.2 ILSP AND ILSE

5.2.1 INTRODUCTION

Iterative Least Squares with Projection (ILSP) [106, 107] and Iterative Least Squares with Enumeration (ILSE) [106, 107] are two block algorithms that use a Maximum-likelihood (ML) approach to separate multiple synchronous co-channel users impinging on an antenna array. Both algorithms exploit the Finite Alphabet (FA) property of digital signals. The main difference between the two algorithms is that ILSP is an adaptive beamforming algorithm whereas ILSE is a joint detection algorithm.

ILSP tries to estimate the channel and transmitted FA symbols by iteratively performing a Least Squares (LS) estimate of the channel and the signals. ILSP maps the signal estimates onto FA symbols by using hard decisions. ILSE searches for the true ML estimate of all users' signals by enumerating over all possible transmitted signals.

5.2.2 SYSTEM MODEL

Figure 5.10 shows the general system structure. The m -element array at the receiver collects N baud-rate samples, thereby forming the $m \times N$ matrix, \mathbf{X} , at the array output, which is called the *received signal matrix*. The parameters d and m denote the number of *synchronous* users and the

number of antenna elements respectively. Note that since the user samples are assumed to be perfectly synchronized, we can simply use a baud-spaced matched filter and then employ a symbol-by-symbol detection scheme. The received signal matrix is then defined by:

$$\mathbf{X} = \mathbf{A} \mathbf{S} + \mathbf{V} \quad (5.11)$$

$d \times N \quad m \times d \quad d \times N \quad m \times N$

where \mathbf{A} is the array steering matrix, \mathbf{S} is the symbol matrix for all d users and \mathbf{V} is the complex white Gaussian noise matrix. These algorithms assume no ISI and, therefore, the channel is simply modeled as the array steering matrix, i.e. line-of-sight channel. This is a valid channel approximation in airborne communication systems where the receiver is located at altitudes on the order of miles above earth surface.

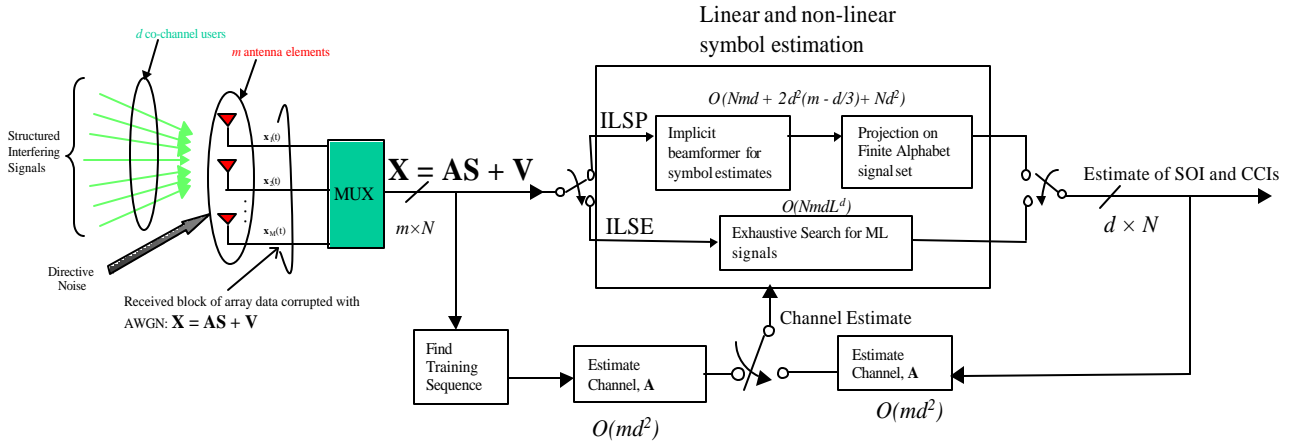


Figure 5.10: Block diagram of the two iterative detectors employing an overloaded array. Symbol synchronous Finite Alphabet user symbols can be extracted by estimating the channel and estimating the symbol matrix iteratively. Symbol estimation can be done either by using the linear ILSP or non-linear ILSE algorithms. The relative complexities in terms of *flops* are denoted in the diagram.

5.2.3 ILSE AND ILSP ALGORITHMS

Baud-spaced complex received signal samples are then processed with either the ILSE or the ILSP detectors to estimate each user's transmitted symbols. Both of the algorithms use an iterative Least Squares (LS) channel estimation. Matrix expression for the channel estimate is given by

$$\hat{\mathbf{A}}_k = \mathbf{X}\mathbf{S}_k^H (\mathbf{S}_k\mathbf{S}_k^H)^{-1} \quad (5.12)$$

where k is the symbol interval. In other words, the estimated symbol matrix of all users is used in a Least Squares fashion to update the corresponding channel matrix. The main difference between the ILSE and ILSP algorithm is the way that the symbol matrix is estimated.

ILSP estimates the transmitted matrix \mathbf{S} by performing a Least Squares (LS) estimate of the signals using the known or estimated channel characteristics using (5.13) and mapping the signal estimates onto FA symbols by using the projection, defined at (5.14). Equation (5.13) has an implicit linear beamformer solution, and therefore limits the performance of the projection approach to underloaded and critically loaded array scenarios.

$$\bar{\mathbf{S}} = (\mathbf{A}^H \mathbf{A})^{-1} \mathbf{A}^H \mathbf{X} \quad (5.13)$$

$$\mathbf{S} = \text{proj}[\bar{\mathbf{S}}] \quad (5.14)$$

On the other hand, the ILSE algorithm searches for the ML estimate of all user signals by enumerating over all possible transmitted signals. This approach provides an optimum solution to the signal extraction problem in the absence frequency-selective multipath. Joint detection of all user symbols is carried out by employing an exhaustive enumeration over all L^d possible $(d \times 1)$ -signal vectors $\mathbf{s}^{(j)}$ and choosing that signal vector that minimizes the ML criterion at (5.15).

$$\hat{\mathbf{s}}(n) = \arg \min_{\mathbf{s}^{(j)} \in \Omega} \|\mathbf{x}(n) - \mathbf{A}\mathbf{s}^{(j)}\|^2, \quad j = 1, \dots, L^d \quad (5.15)$$

where L is the alphabet size, $\hat{\mathbf{s}}(n)$ is the $d \times 1$ signal estimate vector and $\mathbf{x}(n)$ is the $m \times 1$ received signal vector at n^{th} symbol snapshot. The block estimate of the user signal matrix is then given by $\hat{\mathbf{S}}(N) = [\hat{\mathbf{s}}(1), \dots, \hat{\mathbf{s}}(N)]$.

5.2.4 ANALYTICAL PROBABILITY OF ERROR

In our analysis of ILSE, we also utilize the tight upper bound for probability error developed by Talwar *et al.* [106]. This analysis provides an insight to the signal ambiguity problem later depicted in figure 5.17, which is a result of mapping multiple symbols onto the same signal point on the array space. The following Union bound formula gives a tight upper bound on the probability of error (PE) by considering the distance properties of the symbols mapped on the array manifold:

$$PE \leq N_e Q \left(\frac{d_{\min}}{2\mathbf{s}} \right) \quad (5.16)$$

where the minimum distance is given by

$$d_{i,\min} = \min_{i, j \neq i} \|\mathbf{A}\mathbf{s}^{(i)} - \mathbf{A}\mathbf{s}^{(j)}\| \quad j = 1, \dots, L^d \quad (5.17)$$

and $N_e = \frac{1}{L^d} \sum_{i=1}^{L^d} N_i$ represents the average number of nearest neighbors of $\mathbf{A}\mathbf{s}^{(i)}$.

5.2.5 SIMULATION SCENARIOS

In all of our simulations in this section, we use a circular antenna array of radius 0.25λ (where λ is the wavelength of the signal-of-interest). The user symbols are assumed to be perfectly baud-synchronous and are of QPSK modulation format. The performance curves depict the resulting symbol error rates (SER) for the users versus SNR at each antenna element. As mentioned before, the channel is modeled by the steering matrix (LOS channel with no multipath) and is assumed to be time-invariant within each data block. Three different channel scenarios are simulated: (1) apriori known channel, (2) training-based channel estimation, (3) blind channel estimation.

5.2.6 APRIORI KNOWN CHANNEL

Here, the channel is assumed to be perfectly known, i.e. $\mathbf{A}_0 = \mathbf{A}$. In other words, the two techniques, ILSP and ILSE, try to demodulate the user symbols simultaneously without iterating back and forth between the channel estimates and symbol estimates. The results of these known channel simulations set a baseline for the performance of the two iterative algorithms that employ either training-based or blind channel estimation.

5.2.7 TRAINING-BASED CHANNEL ESTIMATION

Training-based channel estimation can be done by using a known preamble embedded in the time slot of each user. Since we have assumed all the users are synchronized with each other, we can use the first $N_{training}$ symbols of each user sequence to carry out the initial channel estimation. The channel is still assumed to be the array steering matrix. We can then represent the received signal matrix of (5.11) as shown in (5.18) where $N_{training}$ and N_{data} represent the number of training symbols and number of data symbols within a burst of N symbols respectively.

$$\begin{bmatrix} \mathbf{X}_{training} \\ \vdots \\ \mathbf{X}_{data} \end{bmatrix} = \mathbf{A} \begin{bmatrix} \mathbf{S}_{training} \\ \vdots \\ \mathbf{S}_{data} \end{bmatrix} + \mathbf{V}, \quad (5.18)$$

where the block length: $N = N_{training} + N_{data}$

Using the signal model of (5.18), the steering matrix is initialized (denoted by \mathbf{A}_0) using a Least Squares estimate of matrix \mathbf{A} as shown in (5.19). Following the initialization, the symbol matrix is estimated using (5.15) and the channel is refined by (5.20) iteratively for the duration of the user slots.

$$\mathbf{X}_{training} = \mathbf{A}_0 \mathbf{S}_{training} + \mathbf{V} \stackrel{LeastSquares}{\Rightarrow} \mathbf{A}_0 = \mathbf{X}_{training} \mathbf{S}_{training}^\dagger \quad (5.19)$$

$$\hat{\mathbf{A}}_k = \mathbf{X}_{data} \mathbf{S}_{k,data}^H \left(\mathbf{S}_{k,data} \mathbf{S}_{k,data}^H \right)^{-1} \quad (5.20)$$

In our simulations, we use an IS-136-type slot format, where $N_{data} = 130$ and $N_{training} = 14$ (approximately 8% of the slot is known). The mere purpose of using the above mentioned slot block format is to see whether the algorithms can perform well in overloaded scenarios even with very short training symbols.

5.2.8 BLIND CHANNEL ESTIMATION

In blind ILSP and ILSE, the channel is initialized by random steering vectors. However, blindly randomizing the steering vectors, i.e. with completely random AOAs, may result in huge number of re-initializations of the channel before the global minimum is reached. This is especially true for the overloaded scenarios. Therefore, the AOAs are randomized in such a way that their means are evenly spaced around 360 degrees, and the pdfs are non-overlapping asymptotically Gaussian. Figure 5.11 illustrates an example AOA randomization. This type of randomization assumes that the range of the user AOAs are known within a specified angular spread around their mean values.

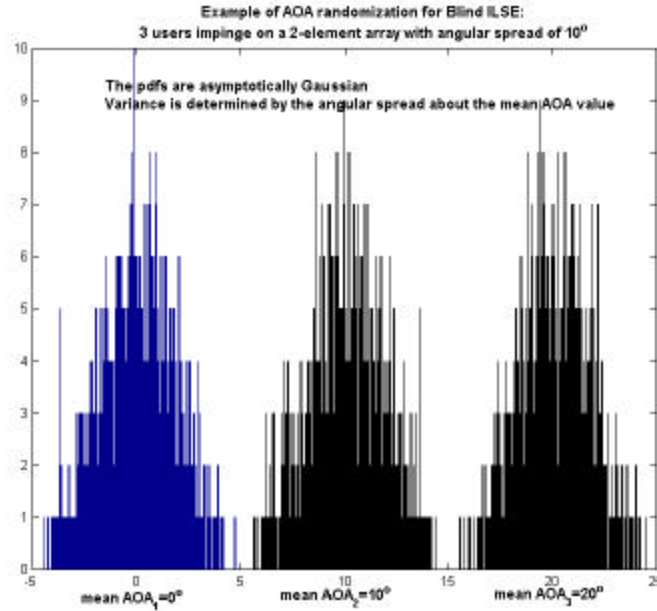


Figure 5.11: Example of AOA randomization for blind ILSE and blind ILSP

Another important issue with blind techniques is that any blind joint detection processor is subject to *port shuffle* problem. When a blind processor is trying to extract signals solely on their signal properties, e.g. ILSE exploits the finite alphabet (FA) property of digital signals, there is no way to distinguish between signals of the same type. Hence, there is no guarantee that the j^{th} user will appear on the output of j^{th} output port of the signal processor. This is called the *port shuffle problem* as depicted in figure 5.12. For digital systems, the port shuffle problem can often be solved by searching for some user id in the demodulated data. No easy solution exists for analog systems.

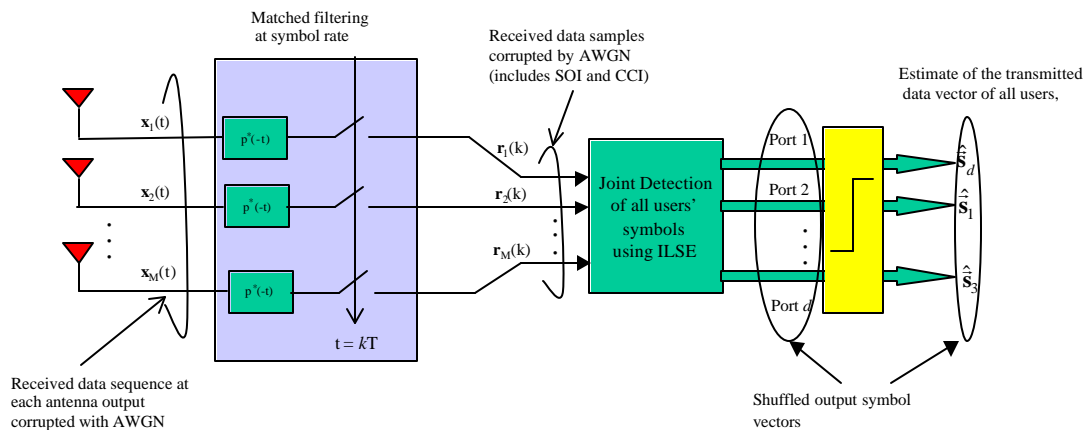


Figure 5.12: Port shuffle problem in blind joint detection techniques.

Figure 5.13 shows the simulation results for ILSP using a perfectly known channel, training-based channel estimation and blind channel estimation. In all cases, the antenna array is fully loaded where $d = \{3,4,5,6,7\}$ synchronous QPSK modulated users impinge on $m = \{3,4,5,6,7\}$ element circular array with radius of 0.25λ . The algorithm performance is very similar in all three cases. The algorithm converges quickly, and therefore the computational complexity is low. However, as explained before, performance of the ILSP algorithm is limited by the ML beamformer and thus by the array size. Therefore, the algorithm cannot support an overloaded antenna array. Figure 5.13 also shows that, the performance degrades as both m and d increase. This is because ILSP is very sensitive to the angular spacing of the users. For higher number of equally spaced users, the angular spacing is small, which causes the columns of \mathbf{A} to become nearly dependent. This results in a noise enhancement while computing the Least Squares estimate of the signals using (5.13) which can also be written as $\bar{\mathbf{S}} = \mathbf{A}^\dagger \mathbf{X}$ where † denotes the pseudo-inverse operation. Figure 5.14(a) depicts the consequence of this noise enhancement. Three equal-power co-channel QPSK users impinge on a three-element circular array (fully loaded array) with AOAs given by 0° , 5° and 12° . ILSP fails to demodulate the users whereas ILSE performs well in the same scenario. Figure 5.14(b) shows the average SER obtained using ILSE for each one of the same three co-channel users. As expected, user 3 has the lowest average SER since it is well separated from the rest of the signals. Therefore, we can deduce that the ILSP algorithm is very sensitive to the user spacing due to the implicit beamformer solution used in symbol estimation, whereas ILSE is still very effective in separating closely spaced users.

Furthermore, ILSE algorithm is able to extract more signals than antenna array elements even when the signals have small spatial separations. Figure 5.15 shows the performance of the ILSE algorithm for the overloaded case where 4 to 10 equally spaced (over 360°), equal-power QPSK signals impinge on a three-element circular array (radius = $\lambda/4$). The algorithm extracts the user symbols at reasonable SNRs until the number of users exceeds the square of the number of elements. The performance of the ILSE is expected to degrade drastically once $d > m^2$.

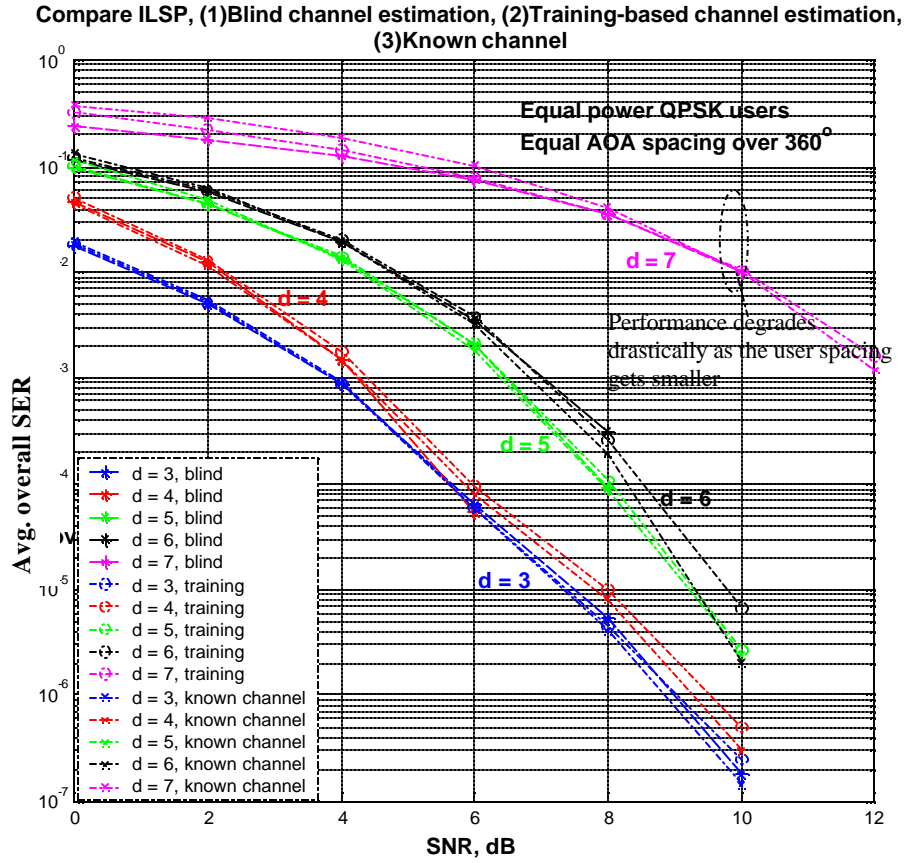


Figure 5.13: Performance curves for ILSP with (1) perfectly known channel, (2) training based channel estimation and (3) blind channel estimation. The array is fully loaded. The users are equally spaced in AOA. The performance degrades with the increasing number of users and antenna elements due to smaller angular spacing of the users. The performance for all three cases are very similar.

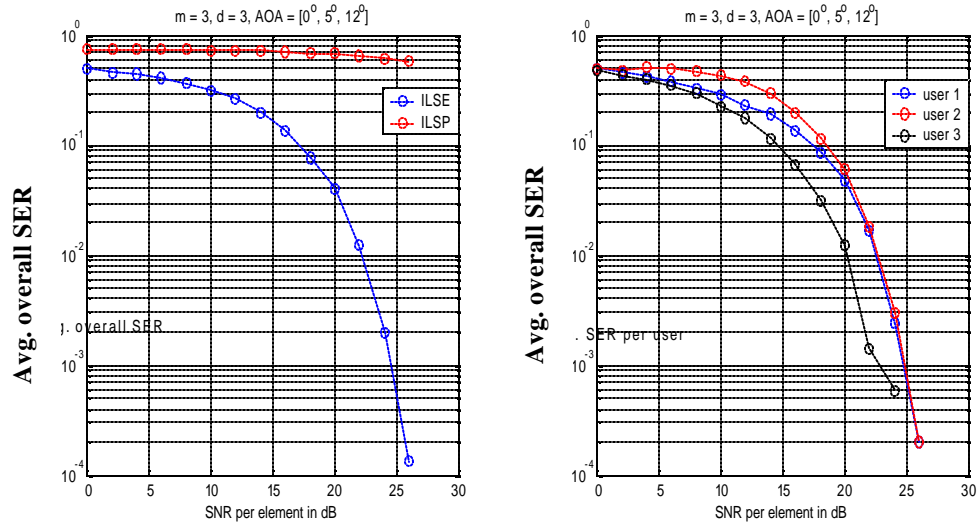


Figure 5.14: (a) Three equal-power synchronous users impinge on a three-element array. ILSE can demodulate closely spaced users whereas ILSP fails drastically. (b) Performance of ILSE in demodulating 3 closely spaced users. The AOA of user 2 is closest to the other two signals and therefore has the highest SER whereas user 3 has the lowest SER since it is well separated from the others.

This might be due to the signal crowding in the array space. Simple visualization example is given in figure 5.16. This figure depicts the signal space at the array output when 5 equal power equally spaced BPSK user symbols impinge on a two-element array. As more and more users impinge on the array, the signal points get very close to each other resulting in indistinct decision boundaries. As expected, signal crowding becomes even more prevalent when the users are very closely spaced. If the users are of different powers, signal points become more separated and thus signal extraction performance of ILSE is expected to improve.

Results depicted in figure 5.15 portray another issue with a symbol-by-symbol joint detection algorithm like ILSE. This so-called, *signal ambiguity* problem is prevalent in joint detection of *equal* power symbol *synchronous* users. This ambiguity occurs when distinct user symbols are mapped on to the same signal point as a result of highly overloaded scenarios. In such cases, the minimum Euclidean distance given by equation (5.17) approaches zero which results in complete ambiguity in the signal space. A simple illustration of signal ambiguity problem is shown in figure 5.17.

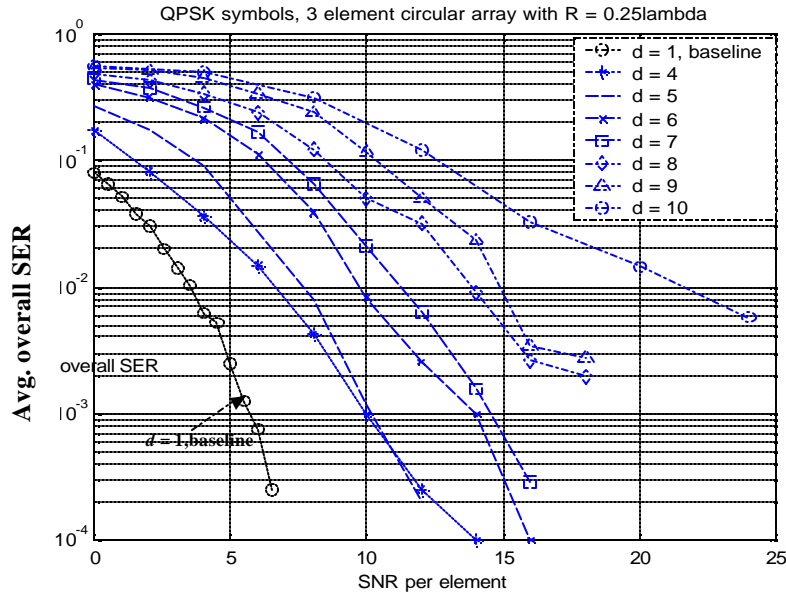


Figure 5.15: The users are equally spaced over 360° (except for the case $m = 3, d = 6$ where the users are equally spaced over 180°). Single user (AOA = 60°) performance is also illustrated as a baseline. The figure shows that ILSE performs well for the cases $d \propto m^2$

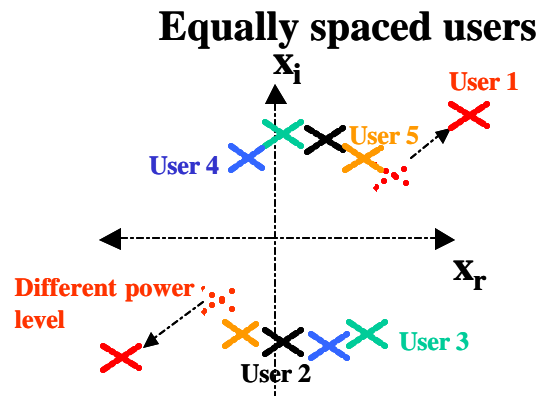


Figure 5.16: *Signal crowding*. Assume a zero-phase unity gain channel. 5 baud-synchronized BPSK users impinge on a 2-element array. Signal points at array output gets closer as more users impinge on the array, i.e. harder to draw decision boundaries. Un-equal powers may help reduce the crowding, e.g. for user 1. Signal crowding is worse for closely spaced users.

However, if the users have un-equal receive powers, signal ambiguity problem becomes insignificant. In fact, the performance of the ILSE algorithm improves in the case of un-equal power users since the algorithm exploits any kind of difference in the FA signal set. We

simulate two different scenarios to show the significance of the signal powers on the algorithm performance. In the first scenario, four closely spaced equal-power users impinge on a two-element array with AOAs = $\{-3^\circ, 0^\circ, 2^\circ, 7^\circ\}$. In the second scenario, the same number of users impinge on the same antenna array however the power distribution of the users is such that $P_{\text{user1}} > P_{\text{user2}} > P_{\text{user3}} > P_{\text{user4}}$. Figure 5.18 shows the resulting average SER curves for each one of the four unequal-power and equal-power users. We can see that, ILSE can successfully demodulate the unequal-power users. However it fails to do so when the users have equal powers.

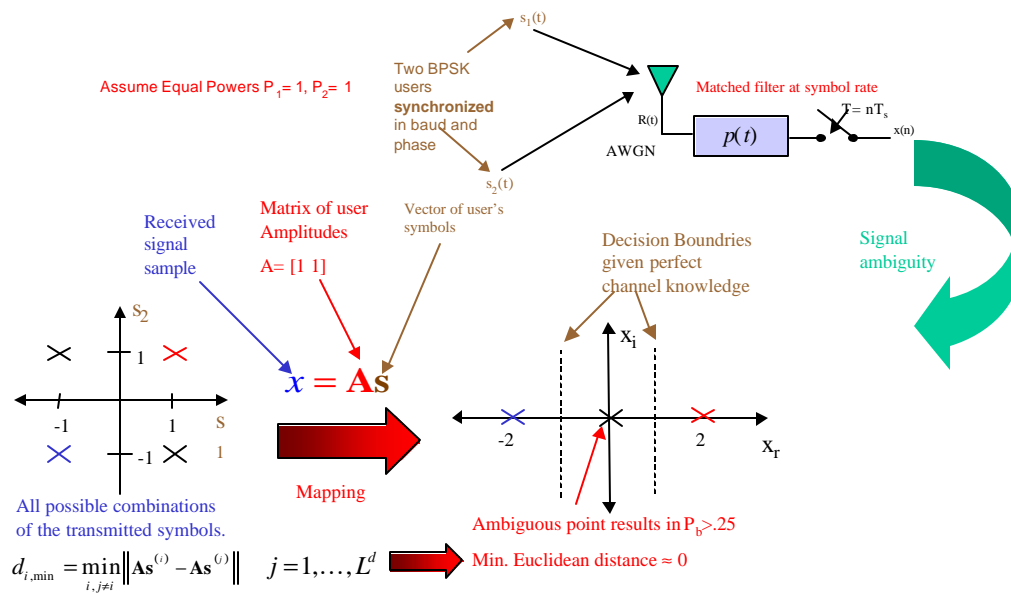


Figure 5.17: Signal ambiguity in joint detection of equal-power synchronous users. Signal ambiguity is most prevalent whenever the user signals are perfectly symbol-synchronous and have equal powers. In that case, the minimum Euclidean distance, $d_{i,\min}$ among the symbols after mapping on the array response becomes zero. This results in an ambiguous point on the signal space. Thus the symbol-by-symbol joint detector cannot distinguish between the distinct transmitted user symbols.

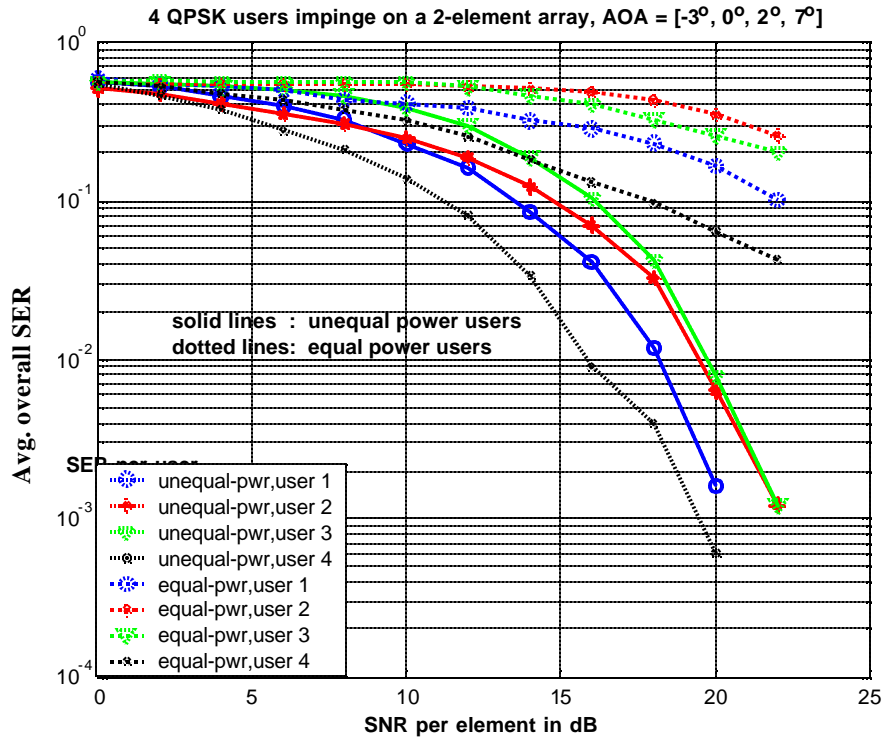


Figure 5.18: Average SER curves for the four closely spaced unequal-power and equal-power QPSK users impinging on a two element array ILSE is able to separate all four unequal-power closely spaced users whereas it fails when the users have equal powers.

Finally, the performance of ILSE with three different channel scenarios are compared: (1) apriori known channel, (2) training-based channel estimation, and (3) blind channel estimation. In each case, a two-element array is used to separate $d = \{3,4,5\}$ closely spaced equal-power QPSK users (10° separation). Figure 5.19 depicts the resulting average overall symbol error rate for nine different scenarios. We can see that, there is almost no degradation in the performance as we go from apriori known channel assumption to blind and training-based channel estimation using short training sequences. As expected, the performance of ILSE in all three cases degrades gracefully with increasing number of users. The important conclusion that can be drawn from these results is that a blind or training-based ILSE processor can successfully separate more signals than number of elements even when the users are of equal powers and are closely spaced.

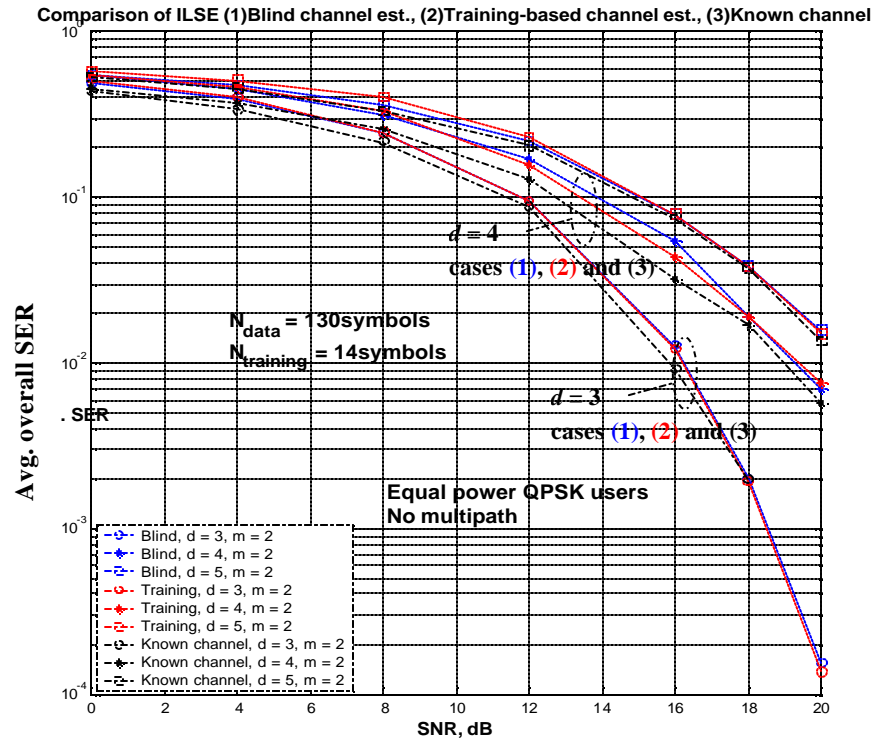


Figure 5.19: Comparison of ILSE (1) blind channel estimation, (2) training-based channel estimation, (3) known channel. Equal-power QPSK users impinge on a two-element antenna. Angle-of-arrival of the users are: $d = 3, [0^\circ, 10^\circ, 20^\circ]$; $d = 4, [0^\circ, 10^\circ, 20^\circ, 30^\circ]$; $d = 5, [0^\circ, 10^\circ, 20^\circ, 30^\circ, 40^\circ]$. Performance of ILSE in all three cases is very similar for the same number of user environment. Performance degrades gracefully as the number of users increase.

5.3 SUMMARY

This chapter analyzed the performance of three different multi-user signal extraction algorithms. The first algorithm, MU-DFE, separates the multiple user symbols simultaneously by using the bank of optimum SINR beamformers built in the MIMO feedforward structure. The weights of the bank of beamformers are calculated according to the MMSE criterion. Although this space-time filter MIMO filter structure has a low computational complexity, signal extraction performance is limited by the array size. The algorithm is shown to perform well in underloaded and critically loaded array scenarios ($m \geq d$) given that the users are well spaced in AOA. However, as the user spacing gets smaller, the beamformers have to form narrower beams in the desired user direction and thus the overall signal extraction performance degrades even in underloaded array scenarios.

The second algorithm, ILSP, has an implicit ML beamformer solution for signal extraction. The optimum beamformer weights in ILSP are calculated by minimizing the Least Squares (LS) solution. The algorithm carries out signal extraction and channel estimation in an iterative fashion. Similar to MU-DFE, the performance of ILSP is limited by the array size and angular spacing of the users. Results have shown that, ILSP with either blind or training-based channel estimation can successfully extract well-separated user signals in critically loaded scenarios.

The final algorithm, ILSE, is a true ML joint detection algorithm that provides an optimum solution for the overloaded antenna array scenarios in the presence of AWGN channel with no frequency selective multipath. The algorithm can successfully demodulate up to m^2 multiple co-channel synchronous signals, assuming that the antenna array is perfectly calibrated. Unlike MU-DFE and ILSP, the performance of ILSE is not sensitive to the user spacing. In fact, ILSE is shown to successfully separate very closely spaced equal-power users even when the channel is not known. Specifically, we show that ILSE processor employing either training-based (with short training sequences) and blind channel estimation performs as good as ILSE with apriori known channel. The simulation results also show that overloaded array performance of ILSE improves further when the users are of un-equal powers.

The main issue associated with ILSE is its prohibitive computational complexity, which is on the order of $O(NmdL^d)$ flops per iteration. ILSE can be improved to separate asynchronous TDMA users. The asynchronous frame case would result in a trellis whose states are estimated using a sequence estimator. The trellis search would add to the already existing high complexity of the ILSE algorithm. Another extension may be to incorporate frequency-selective multipath, which again would result in a channel with memory and thus requiring a more complex ML sequence estimator. Even though ILSE is not a practical solution to the overloaded signal extraction problem, it provides a theoretical baseline for future work. Sub-optimal techniques to replace the ML brute force as well as incorporating a robust and less complex channel estimation techniques are open research issues in overloaded array processing.

CHAPTER 6: MULTI-USER TIME DELAY ESTIMATION AND SYNCHRONIZATION

6.1 INTRODUCTION

In Chapter 5, all of the multi-user signal extraction algorithms assume that user symbols are perfectly time and phase aligned at the receiver antenna array. This enables symbol-by-symbol joint detection. However, in practical mobile communication systems, the uplink transmission is completely asynchronous. In other words, the user data are not time, and phase aligned due to the propagation delays and clock mismatches. This condition necessitates appropriate phase and time synchronization (or timing delay estimation) in the receiver before signal separation using a joint detection algorithm. This thesis deals with symbol timing issues only, in other words, we will assume perfect phase recovery throughout the rest of this final chapter.

Main goal of the delay estimation research effort is to come up with a low complexity data-aided timing recovery algorithm and embed it in a Per Survivor Processing [7,43] trellis. Figure 6.1 illustrates a simple case where 2 asynchronous BPSK user signals impinge on a receiver with unknown time delays, $\tau_1 = \varepsilon_1 T$ and $\tau_2 = \varepsilon_2 T$, where T is the symbol period. This time misalignment between 2 user sequences result in ISI, which can be represented with a joint detection trellis as shown in figure 6.2. The complexity of such a trellis would be: $L^{\mathbf{d}} \times L^{\mathbf{d}}$, where L is the alphabet size ($L = 2$ for BPSK), d is the number of users and \mathbf{d} is the number of ISI symbols. Viterbi algorithm can be used to find the most likely path through the trellis and jointly detect user symbol sequences. This is the conventional MLSE algorithm used as a joint detector. Per Survivor Processing, on the other hand, is a more powerful *blind* ML technique that estimates channel parameters as well as the transmitted symbol sequences. Our ultimate goal in multi-user time delay estimation research is to utilize PSP trellis as shown in figure 6.3 to update time delay estimates for each user at each state of the trellis by using the candidate symbols as well as candidate receive samples. This approach suggests a low-complexity data-aided timing delay estimation algorithm that would produce new time-delay estimates for each user as shown in figure 6.4. These delay estimates along with the past candidate user symbols (suggest data-aided techniques) would then be used in the next stage to refine the delay

estimates. Figure 6.4 suggests a robust and low-complexity multi-user delay estimation algorithm based on data-aided techniques.

In our research effort, we focused on data-aided delay estimation techniques because they can exploit the built-in training sequences in TDMA-type systems, and known pilot sequences in CDMA-type systems.

The following section of this chapter gives an analysis of the multi-user time delay estimation problem in an attempt to come up with a low-complexity data-aided structure that could easily be embedded in previously mentioned complex PSP architecture.

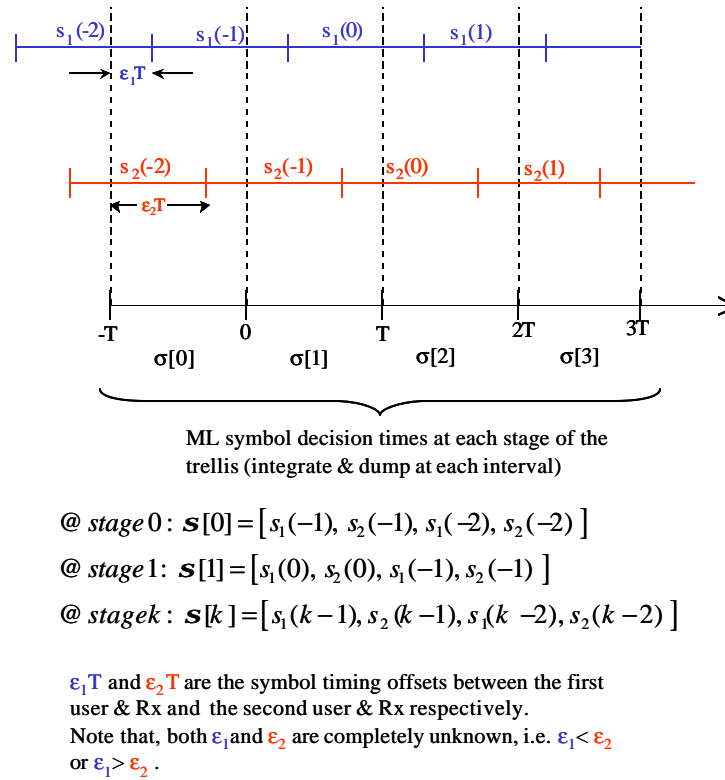


Figure 6.1: Illustration of 2 asynchronous BPSK user sequences

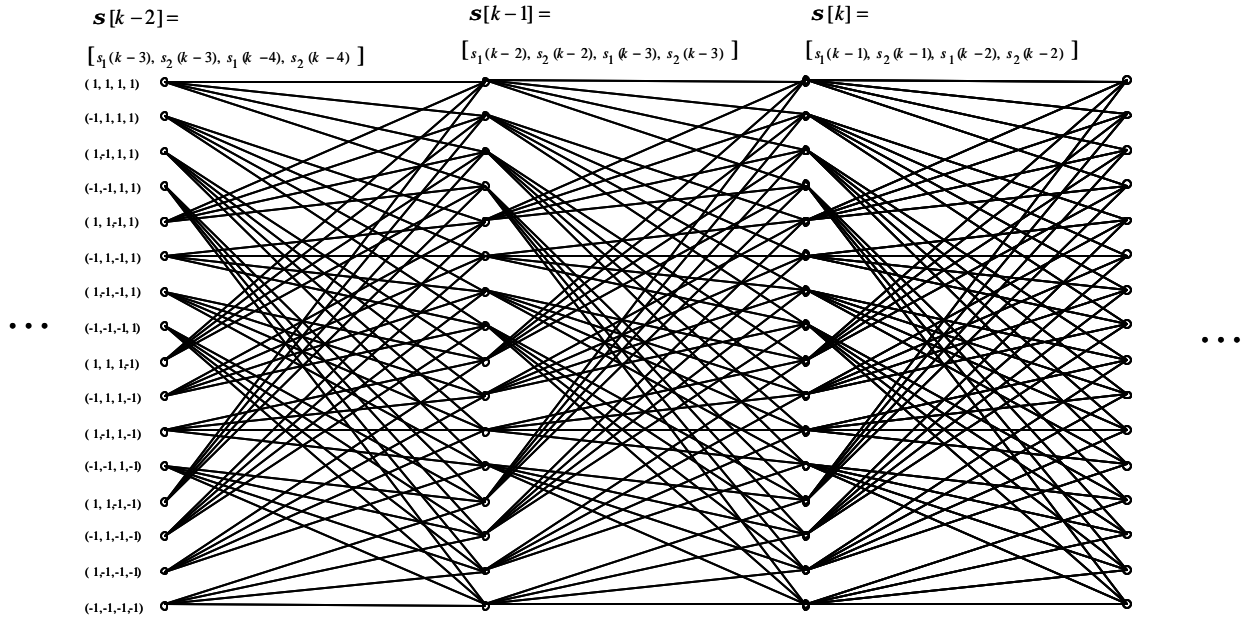


Figure 6.2: MLSE used as a joint detector. In this example, detection of 2 asynchronous BPSK users requires a joint detection trellis due to the 2-symbols of ISI (time misalignment as shown in figure 6.1).

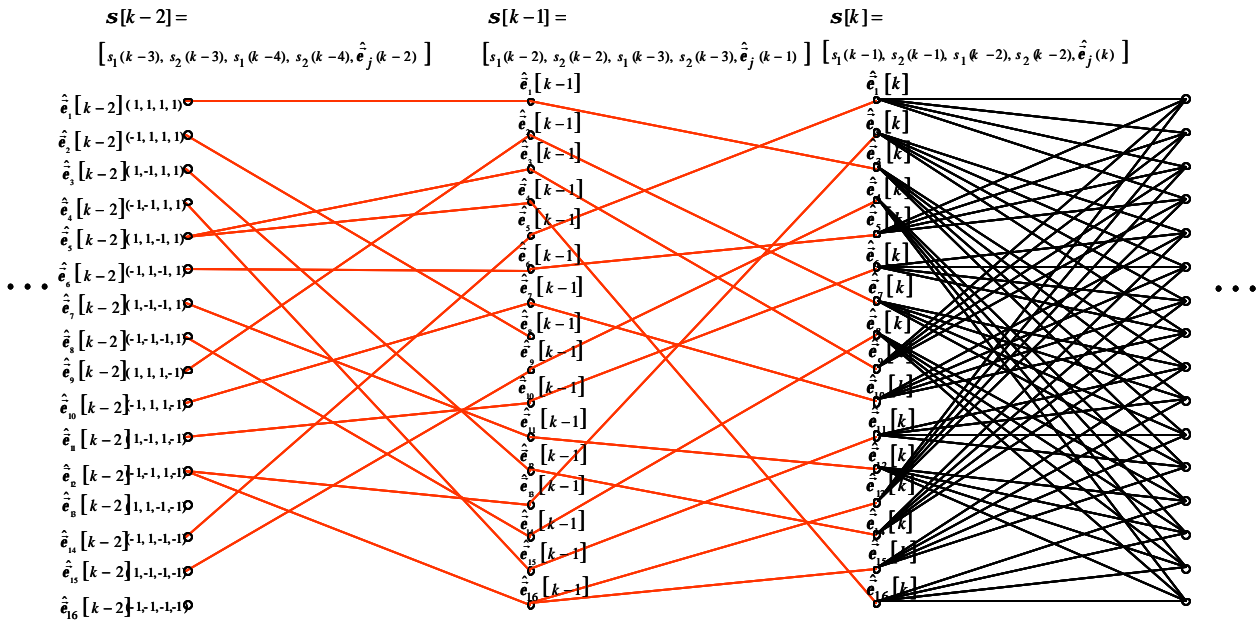


Figure 6.3: Proposed PSP based channel estimation algorithm that incorporates time-delay estimation algorithm. Each user's time delay as well as symbol sequence are estimated at each state of the PSP trellis. These estimates are updated in the following stages until the trellis is terminated.

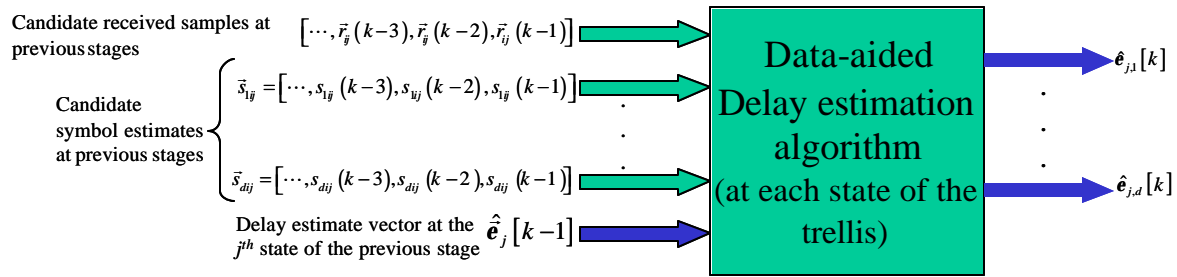


Figure 6.4: Conceptual data-aided time delay estimation algorithm to be used within the PSP trellis.

6.2 ANALYSIS OF MULTI-USER DELAY ESTIMATION PROBLEM

Figure 6.5 shows the two main multi-user delay estimation structures. The first structure is a joint multi-user delay estimator based on brute force ML search over a quantized range of candidate delay estimates. Several ML multi-user time delay estimation algorithms have been proposed in the context of multipath time-delay estimation [23, 61, 62, 63] as well as in the context of JADE (Joint Angle-of arrival and Delay Estimation) techniques [75, 76, 77, 80, 82]. All of these algorithms rely on a maximum likelihood search for the delay estimates, and therefore are far too complex to embed in the PSP trellis shown in figure 6.3.

A low-complexity alternative to joint multi-user delay estimation techniques is to perform synchronization on a single user (thus estimate its time delay) and treat the rest of the users as interference modeled as either (1) AWGN or (2) colored noise.

However, before applying single user delay estimation algorithm to a multi-user scenario, we have to answer a fundamental question: is the multi-user delay estimation problem separable? In other words, can we treat the interference as additive noise (either white or colored) and perform synchronization merely on the desired user's sequence as well as estimating its time delay? If so, how much do we lose in performance by treating the interference simply as AWGN instead of colored noise process? The following analysis provides answers to these questions.

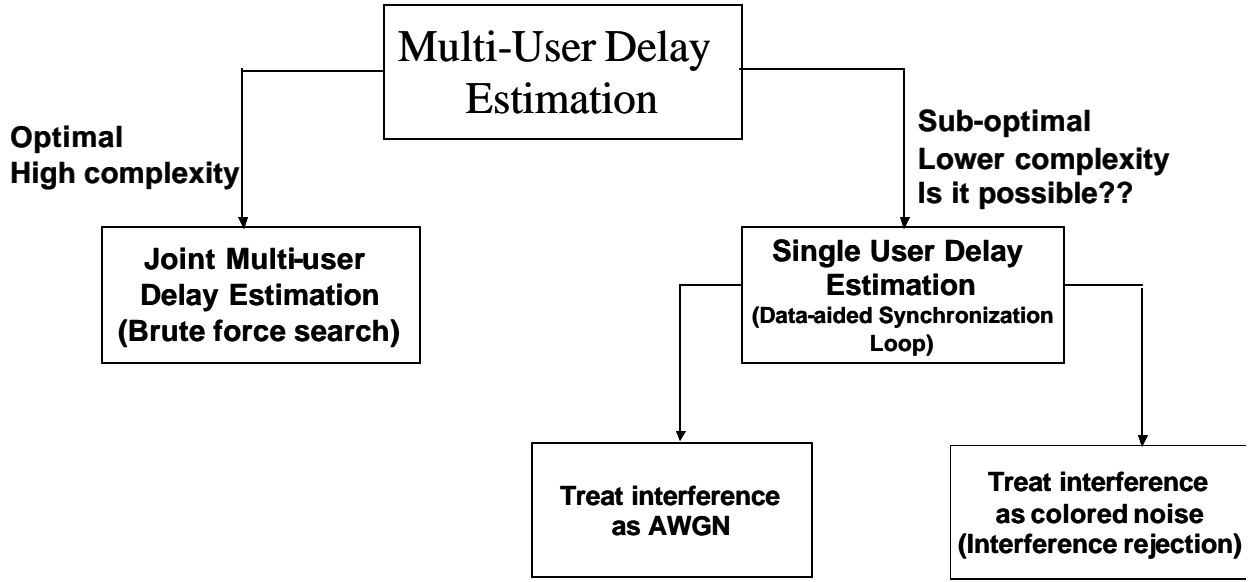


Figure 6.5: Roadmap of Multi-user time delay estimation

6.2.1 DISCRETE EQUIVALENT CHANNEL MODEL

Figure 6.6 depicts the discrete equivalent channel model used in multi-user delay estimation analysis. Assume Du user signals (no multipath components) impinge on a single antenna, then the received signal, $r(t)$, at the front end of the receiver can be modeled as:

$$r(t) = x(t) + z(t) = \sum_{d=1}^{Du} \sum_{l=1}^{Npkt} \mathbf{a}_d s_d(l) p(t - lT_{sym} - \mathbf{t}_d) + z(t) \quad (6.1)$$

where $Npkt$ is the slot length for each user, s_d , \mathbf{t}_d and \mathbf{a}_d are d^{th} user's *known* symbol, *unknown* time delay and *known* complex channel gain, respectively. In the analysis, complex channel gain was modeled as a Rayleigh random variable, and raised cosine pulse shaping was used for the pulse shaping function, $p(t)$. Additive noise process $z(t)$ was assumed to be AWGN within the band of desired signal.

The fractional rate sampler at the receiver over-samples the noisy received signal is then by a factor of Q_o . The received signal samples can then be represented as:

$$r[k] = \sum_{d=1}^{Du} \sum_{l=1}^{Npkt} s_d(l) \mathbf{a}_d p\left(\frac{kT_{sym}}{Q_o} - lT_{sym} - \mathbf{t}_d\right) + z[k] \quad (6.2a)$$

Finally, we can further modify (6.2a) to express the received *sub-samples* as

$$r[n, q] = x[nQ_o, q] + z[nQ_o, q] = \sum_{d=1}^{Du} \sum_{l=1}^{Npkt} s_d[l] \mathbf{a}_d p \left((nQ_o + q) \frac{T_{sym}}{Q_o} - \mathbf{t}_d \right) + z[nQ_o, q] \quad (6.2b)$$

where q is the sub-sample index (sample index per symbol), n is the symbol index. From (6.2b), we can write the expression for the discrete equivalent channel of the d^{th} user:

$$\mathbf{G}_0^d = \left[g_0^d \ g_1^d \ \cdots \ g_{Q_o}^d \right]^T \quad (6.3)$$

where $g_q^d = \mathbf{a}_d p \left((nQ_o + q) \frac{T_{sym}}{Q_o} - \mathbf{t}_d \right)$.

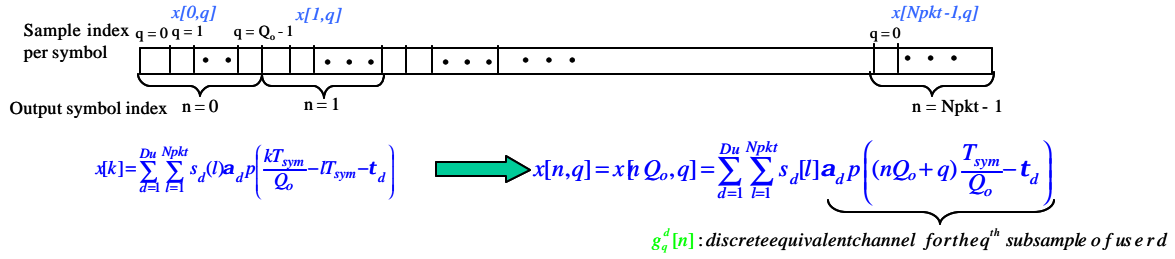
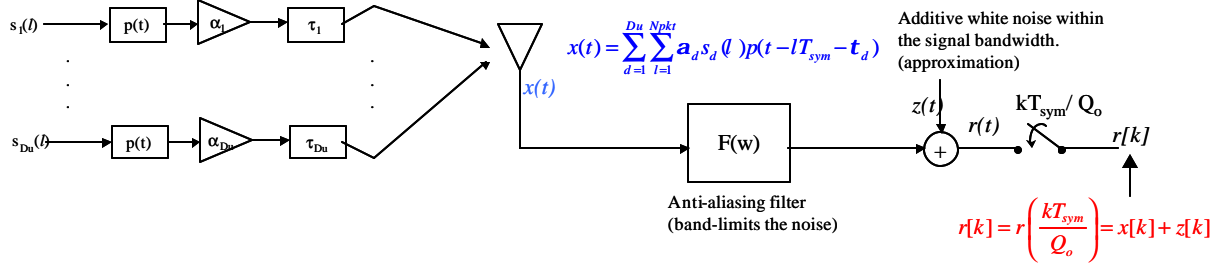


Figure 6.6: Discrete equivalent channel model used in the analysis .

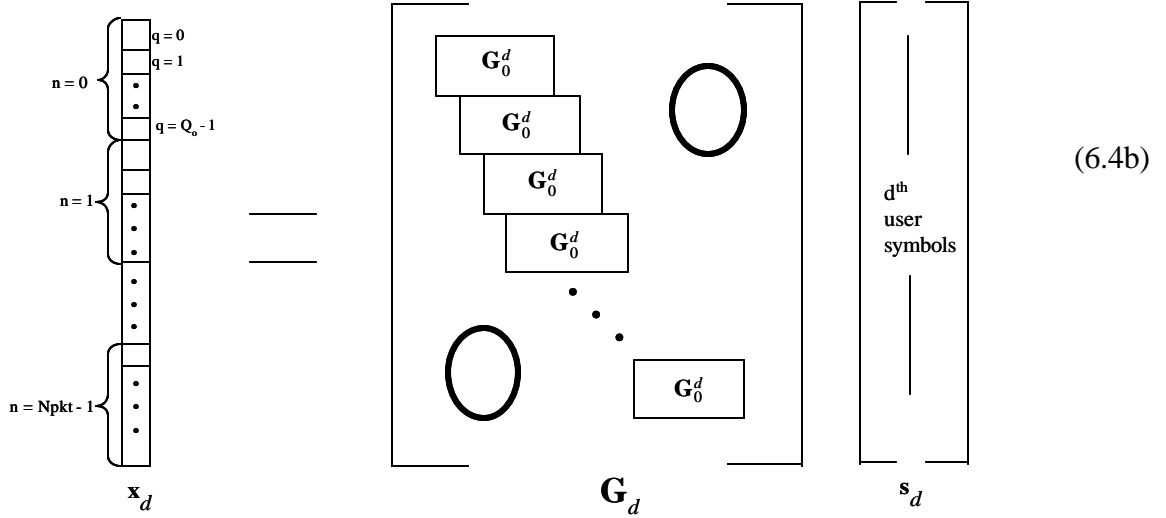
Using the channel model of (6.3) we can re-write the received signal vector as

$$\mathbf{r}_{rcv} = \sum_{d=1}^{Du} \mathbf{x}_d + \mathbf{z} = \sum_{d=1}^{Du} \mathbf{G}_d \mathbf{s}_d + \mathbf{z} \quad (6.4a)$$

$(Q_o \cdot Npkt) \times 1$

where the sub-sample vector for the d^{th} user's received signal, \mathbf{x}_d , is given by (6.4b) where \mathbf{G}_d represents the discrete equivalent channel for the d^{th} user arranged in a block Toeplitz matrix format.

In our analysis, we assumed that the only unknown parameter of the discrete channel model, \mathbf{G}_d , is the time delay of the d^{th} user, τ_d .



6.2.2 MAXIMUM LIKELIHOOD COST FUNCTION

We can derive the ML cost function for the joint multi-user delay estimation as well as for the single user delay estimation by using (6.4a) and (6.4b). ML criterion for joint multi-user delay estimation requires a d -dimensional search to find the most likely delay estimation vector for d users and is given by

$$\hat{\mathbf{t}}_{\times d} = \underset{\mathbf{t}}{\operatorname{argmin}} F_{ML}(\mathbf{t}) = \underset{\mathbf{t}}{\operatorname{argmin}} \left\| \mathbf{r}_{rcv} - \sum_{d=1}^{Du} \hat{\mathbf{x}}_d(\mathbf{t}_d) \right\|^2 \quad (6.5)$$

On the other hand, single user delay estimation cost function requires d one-dimensional search to estimate the delays of d users. Corresponding ML criterion that estimates the desired user's time delay is then given by

$$\hat{\mathbf{t}}_{du} = \underset{\mathbf{t}_{du}}{\operatorname{argmin}} F_{ML}(\mathbf{t}_{du}) = \underset{\mathbf{t}_{du}}{\operatorname{argmin}} \left(\mathbf{r}_{rcv} - \hat{\mathbf{x}}(\mathbf{t}_{du}) \right)^H \Phi_{nn}^{-1} \left(\mathbf{r}_{rcv} - \hat{\mathbf{x}}(\mathbf{t}_{du}) \right) \quad (6.6a)$$

where, the estimate of the desired user received signal component, $\hat{\mathbf{x}}(\mathbf{t}_{du})$ can be represented by

$$\hat{\mathbf{x}}(\mathbf{t}_{du}) = \mathbf{G}_{du} \mathbf{s}_{du} \quad (6.6b)$$

In (6.6) Φ_{nn} denotes the impairment covariance matrix. In this analysis, two different cases are considered: (1) ignore the interference by treating it as AWGN, and (2) account for the

interference in the covariance matrix. The first case results in the following formulation of the impairment covariance matrix:

$$\Phi_{nn} = \mathbf{s}_z^2 \mathbf{I} \quad (6.7a)$$

where \mathbf{s}_z^2 is the variance of AWGN.

The second case accounts for both AWGN and CCI in the covariance matrix:

$$\mathbf{F}_{nn} = \sum_{d, d \neq du} \mathbf{s}_d^2 \mathbf{G}_d \mathbf{G}_d^H + \mathbf{s}_z^2 \mathbf{I} \quad (6.7b)$$

The following section discusses the results of the comparison of the three different cases mentioned above.

6.2.3 ANALYSIS RESULTS

Figure 6.7 (a) and (b) depict the joint multi-user delay estimation error surface for two equal power QPSK users with delays, $\tau_1 = -0.2T_{\text{sym}}$ and $\tau_2 = 0.1T_{\text{sym}}$, for different block lengths at a fixed SNR of 18dB. Four graphs in figure 6.7(a) show that the user delays are not separable for a block length of 10 symbols ($N_{\text{pkt}} = 10$). In other words, the delay for the user 2 cannot be accurately estimated given that the delay of user 1 is perfectly known, and vice versa. This situation can easily be visualized in the two checkerboard plots in figure 6.7(a). On the other hand, if we increase the block length to $N_{\text{pkt}} = 30$ symbols, the delays become separable. This is depicted in figure 6.7(b). In other words, given that τ_1 is perfectly estimated, minimizing the cost function, F_{ML} , would exactly give the value for τ_2 , and vice versa.

Figure 6.8 shows the results for estimating the delay of a single SOI given that the delays of CCI are perfectly known. These results set lower bounds on joint delay estimation for different block sizes and different number of users. As expected, the standard deviation of the error estimate ($\mathbf{s}_{\mathbf{f}_{du}}$) decreases with increasing SNR and N_{pkt} . For a fixed block size, $\mathbf{s}_{\mathbf{f}_{du}}$ is insensitive to the increasing number of CCI. Figure 6.8 also shows that $\mathbf{s}_{\mathbf{f}_{du}}$ converges to within $0.05 T_{\text{sym}}$ for $\text{SNR} > 12\text{dB}$ and $N_{\text{pkt}} \geq 20$ symbols with very slight degradation in error in going from $N_{\text{pkt}} = 20$ to $N_{\text{pkt}} = 30$.

In short, figures 6.7 and 6.8 depict that multi-user time delay estimation problem is separable for short blocks of *known* data, e.g. $N_{\text{pkt}} \geq 20$ symbols, for appreciable SNRs. Now, the question is: what is the performance degradation in estimating the delay of SOI in the case of (1) ignoring CCI completely (treating the CCI as AWGN) and (2) accounting for the CCI?

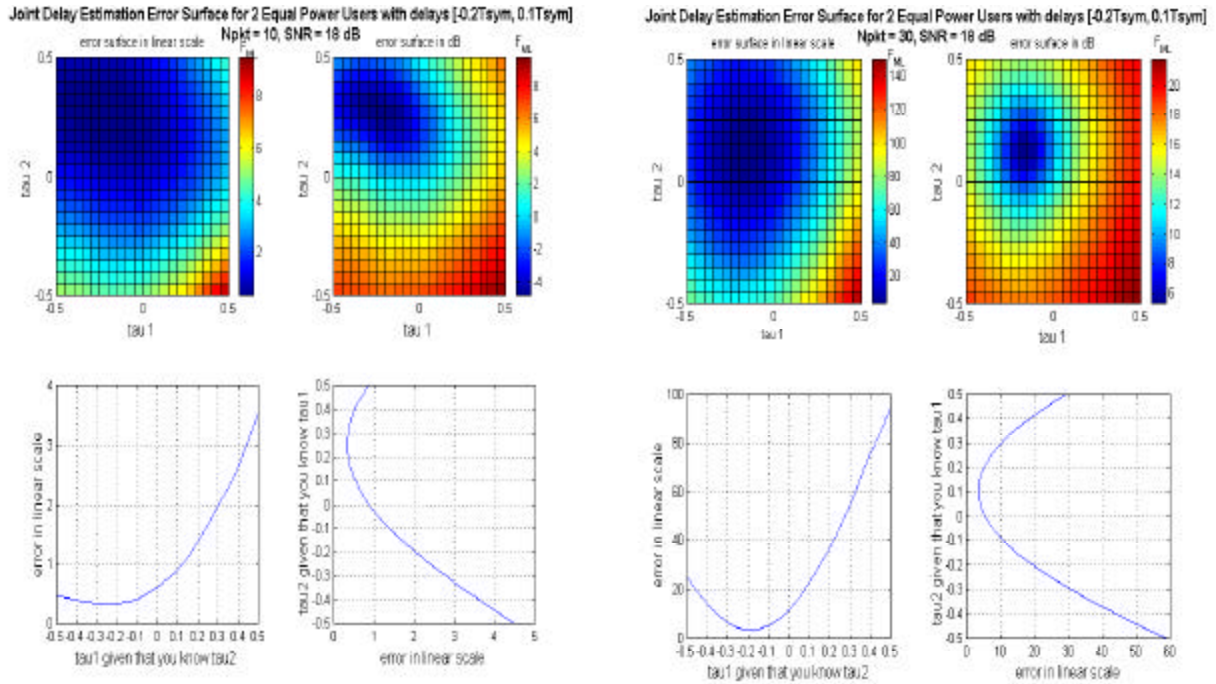


Figure 6.7: Joint multi-user delay estimation error surface. (a) Delays are not separable for short data blocks, e.g. $N_{\text{pkt}} = 10$ symbols. τ_1 cannot be reliably estimated given that τ_2 is perfectly known, and vice versa. This is depicted in the two checkerboard plots. (b) Delays become separable for longer data blocks, e.g. $N_{\text{pkt}} = 30$ symbols.

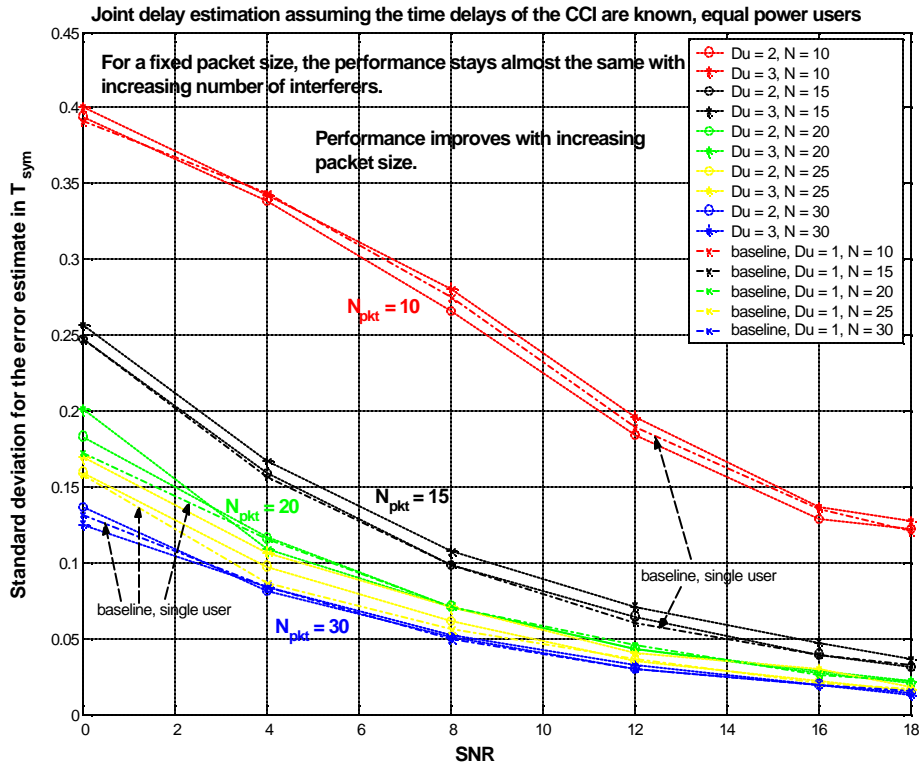


Figure 6.8: Results for estimating the delay of SOI given that the delays of CCI are perfectly known. Lower bounds on joint delay estimation for different block sizes and different number of users. Delay estimation error has a Gaussian distribution with zero mean, therefore standard deviation of the error estimate in T_{sym} is plotted against SNR.

Figures 6.9 compares the delay estimation error versus N_{pkt} in both cases for different number of CCI. The SNR is fixed at 18dB. In both situations, the error increases with increasing number of CCI and as expected, case (2) behaves better than case (1).

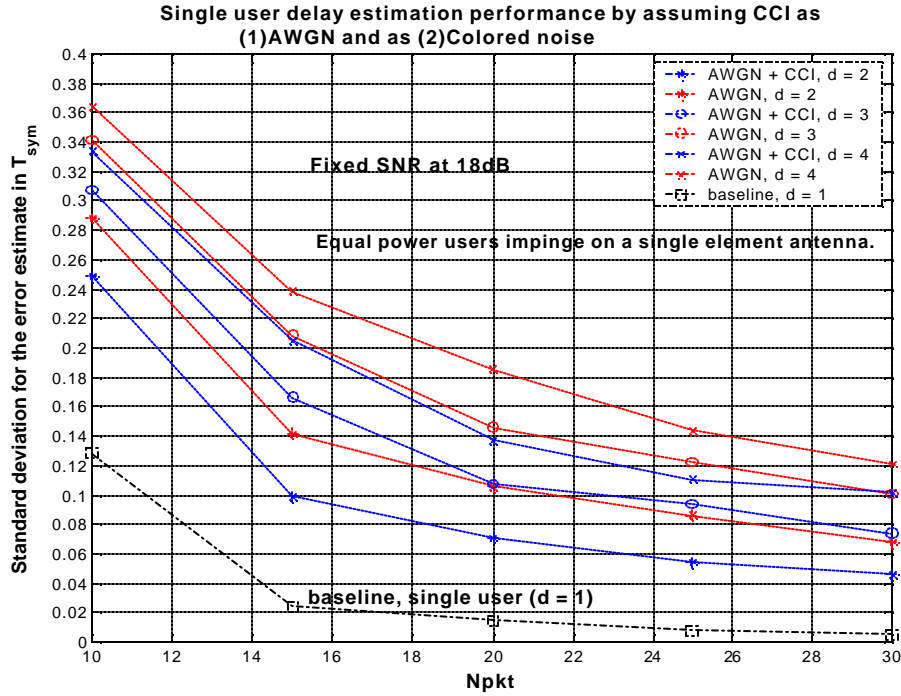


Figure 6.9: Single user delay estimation. Case (1): ignore the interference and treat it as AWGN. Case(2): account for the interference in the ML function formulation.

Figure 6.10 compares the delay estimation error in case (1) and case (2) with the lower bounds shown in figure 6.8. To summarize the results of this section, one can conclude that single-user delay estimation is a sub-optimal low complexity solution to the multi-user delay estimation problem. The multi-user delays are separable for block sizes larger than 20 symbols and accounting for interference in the formulation of the ML criterion improves the delay estimation performance. We can further investigate the characteristics of the impairment covariance matrix given in (6.7b) by using Cholesky factorization:

$$\Phi_{nn}^{-1} = \mathbf{F}^H \mathbf{F} \quad (6.8)$$

We can then modify the ML criterion given in (6.6a) with (6.8):

$$\begin{aligned}
F_{ML} &= \left(\mathbf{r}_{rcv} - \hat{\mathbf{x}}(\mathbf{t}_{du}) \right)^H \mathbf{F}^H \mathbf{F} \left(\mathbf{r}_{rcv} - \hat{\mathbf{x}}(\mathbf{t}_{du}) \right) \\
\operatorname{argmin}_{\mathbf{t}_{du}} & \\
\Rightarrow F_{ML} &= \left[\mathbf{F} \left(\mathbf{r}_{rcv} - \hat{\mathbf{x}}(\mathbf{t}_{du}) \right) \right]^H \left[\mathbf{F} \left(\mathbf{r}_{rcv} - \hat{\mathbf{x}}(\mathbf{t}_{du}) \right) \right] \\
\operatorname{argmin}_{\mathbf{t}_{du}} & \\
\Rightarrow \hat{\mathbf{t}}_{du} &= \operatorname{argmin}_{\mathbf{t}_{du}} F_{ML}(\mathbf{t}_{du}) = \operatorname{argmin}_{\mathbf{t}_{du}} \left\| \mathbf{F} \left(\mathbf{r}_{rcv} - \hat{\mathbf{x}}(\mathbf{t}_{du}) \right) \right\|^2
\end{aligned} \tag{6.9}$$

Figure 6.11 shows the resulting block Toeplitz structure of the \mathbf{F} matrix (Cholesky factor of Φ_{mm}^{-1}), which suggests that \mathbf{F} can be used as a *linear pre-filter*. Therefore, the new ML criterion in (6.9) suggests a data-aided single-user delay estimation structure shown in figure 6.12. In this structure, a pre-filter, \mathbf{F} , can be used to whiten the noise (some type of interference rejection at the front end) and then apply the data-aided delay estimation algorithm on the “clean” signal and estimate the time delay of the desired user signal.

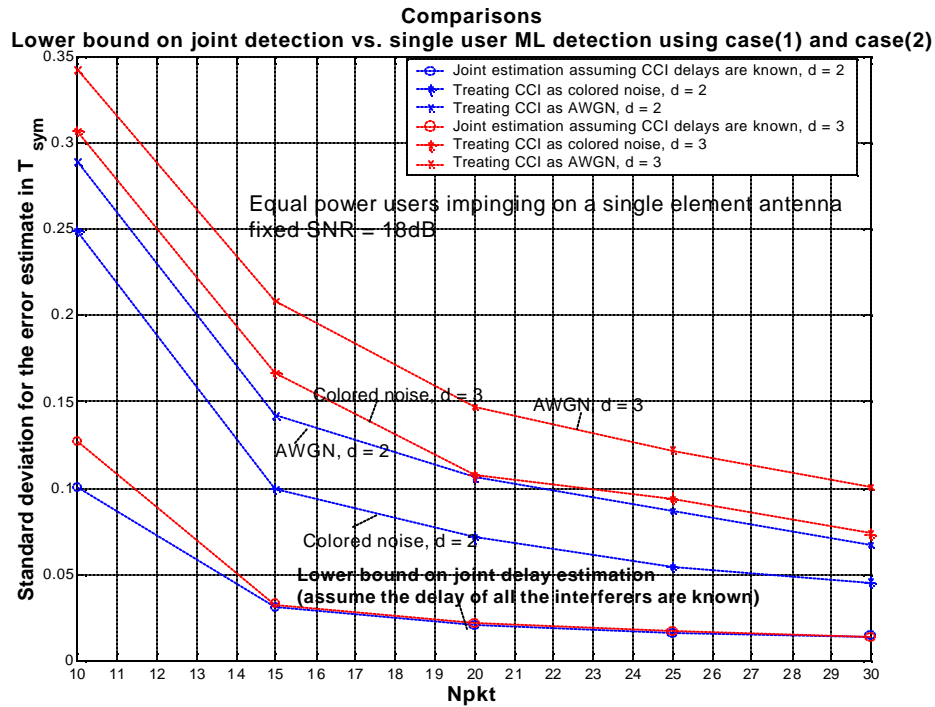


Figure 6.10: Comparison of case (1) and case (2) results with lower bound results.

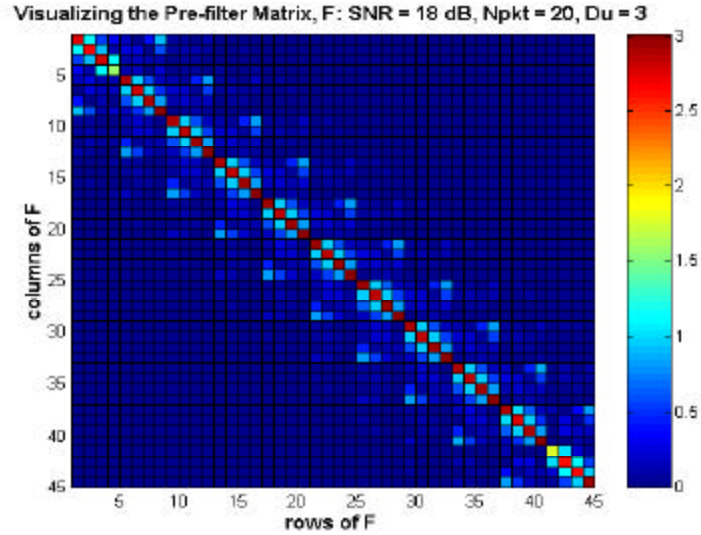


Figure 6.11: Cholesky factor of Φ_{nm}^{-1} is a block Toeplitz matrix \mathbf{F} . This matrix can be used as a linear pre-filter for interference rejection (noise whitening).

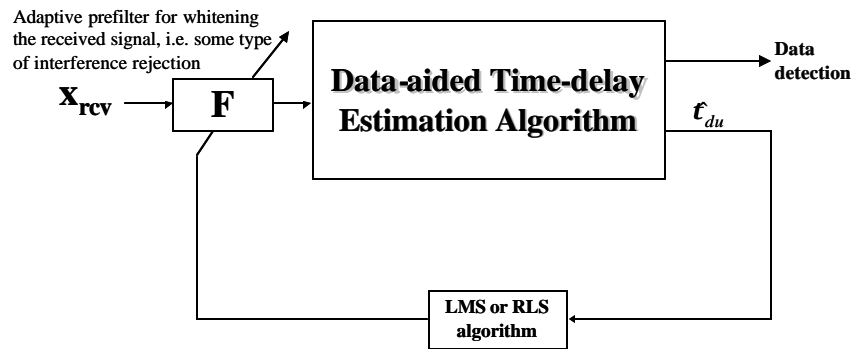


Figure 6.12: Possible multi-user time delay estimator structure. Received signal (SOI + CCI+AWGN) is first pre-filtered with an adaptive linear filter, \mathbf{F} . Then SOI's time delay is estimated by a low-complexity data-aided time delay estimation algorithm. The coefficients of the adaptive filter can be updated using either LMS or RLS algorithms.

The following section of this chapter proposes a low-complexity single-user synchronization/time-delay estimation algorithm based on data-aided techniques.

6.3 DATA-AIDED SINGLE-USER DELAY ESTIMATION ALGORITHM

As mentioned in the previous section, the goal is to design a robust and low-complexity multi-user time delay estimator and embed it in a PSP trellis. We have also shown in the above analysis that, single user delay estimation in a multi-user environment is feasible assuming that we have long enough known data sequences (e.g., training sequences in TDMA systems), i.e. $N_{\text{pkt}} > 20$ symbols.

Many single user delay estimation and synchronization algorithms based on data-aided techniques exist in signal processing literature [85, 87 - 94]. All of these techniques employ a digital timing recovery loop and an interpolator for estimating and compensating for non-integer sample delays. These techniques are mainly developed for correcting for mismatch between the transmitter local oscillator and free running receiver oscillator. This mismatch causes small drifts in samples. In our research, we assume that the transmitter and receiver clocks are perfectly matched, and thus the time delay is attributed to the propagation delays in a wireless environment.

Consequently, we developed a general purpose Delay Locked Loop (DLL) that can estimate and compensate for both integer and non-integer sample delays within $\pm T_{\text{sym}}$. Section 6.3.1 gives a brief overview of the structure of a generic DLL. Section 6.3.2 explains the specific features of the proposed DLL. Section 6.3.3 shows simulation results for DLL operation in single-user case. Finally, Section 6.3.4 summarizes the results for the DLL algorithm.

6.3.1 DELAY LOCKED LOOP (DLL)

Figure 6.13 depicts a general digital timing recovery loop based on a DLL structure. This structure is very similar to Gardner's timing recovery structure [85, 87], which has been widely used in today's practical synchronization systems. The DLL comprises of three main parts: Timing Error Detector (TED), timing control, and interpolator & decimator. Pulse shaped noisy received signal is first matched filtered at symbol rate and then oversampled by a factor of Q_b by a free running clock. These samples are then processed by an interpolator/decimation filter (FIR filter) that compensates for the fractional sample delays. The interpolator produces interpolants at a higher rate than $1/T_s$. These interpolants are then decimated to produce T_s -spaced samples. These T_s -spaced interpolants are used by the TED to detect timing error information for future symbol and are further decimated to symbol rate for data detection. TED generates an error signal based on a data-aided algorithm, which is fed to the loop filter for averaging. The loop filter output is some function of the timing error, which is used by the control unit to refine the timing adjustment and update the interpolation/decimation filter input.

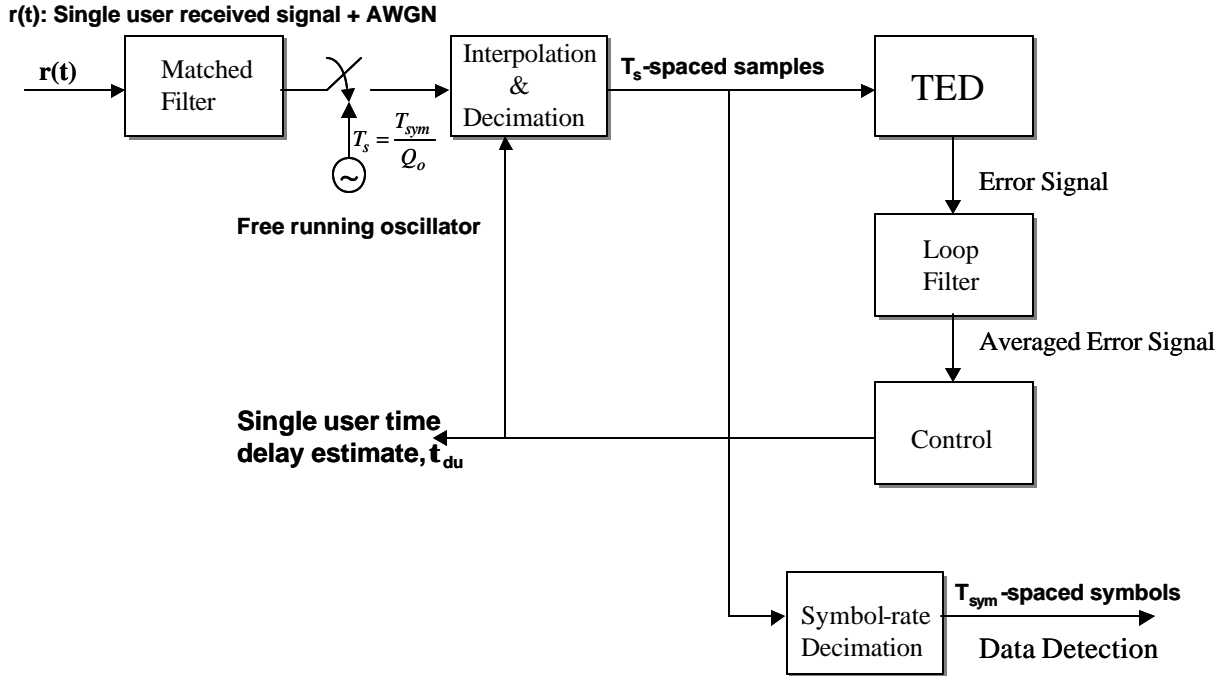


Figure 6.13: Block Diagram of General DLL architecture

6.3.2 PROPOSED SCHEME

A detailed block diagram for the proposed DLL algorithm is given in figure 6.14. Time delay of the desired user to be estimated can be represented by

$$\mathbf{t}_{du} = (m_k + \mathbf{m}_k)T_s \quad (6.10)$$

where m_k and \mathbf{m}_k are the integer-sample delay portion and fractional-sample delay portion of the overall time delay. The goal of the DLL is to estimate both m_k and \mathbf{m}_k and compensate for the time delay. The following sections briefly discuss the structure of the rest of the DLL components.

6.3.2.1 INTERPOLATION AND DECIMATION PROCESSING

The goal of the interpolator/decimator filter is to use m_k and μ_k estimates generated by the control algorithm to execute interpolation and build desired interpolants. There exists a host of interpolator/decimator structures [87, 89, 90, 94]. This thesis compares two simple structures: Linear interpolator and cubic interpolator.

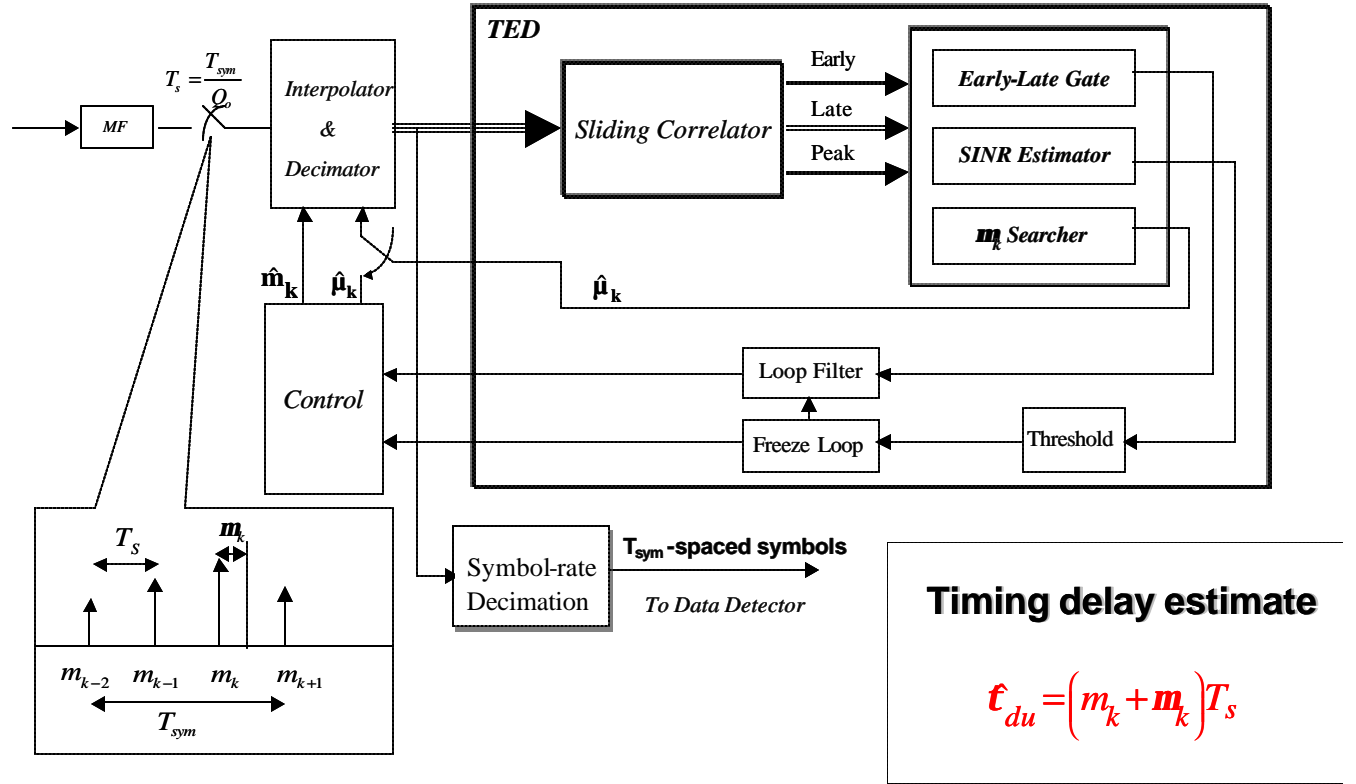


Figure 6.14: Proposed DLL block diagram. m_k : basepoint sample out of Q_o samples per symbol, μ_k : fractional timing offset

6.3.2.1.1 Linear Interpolation

Linear interpolation can be implemented by the simple formula:

$$y(kT_i) = y(k) = x(m_k) + \mu_k [x(m_k + 1) - x(m_k)] \quad (6.11)$$

This is a 1st order polynomial with respect to μ_k where the coefficients are linear super-positions of the two samples. This formula implements the straight line that connects the two samples and builds any third point along that line, which is located in offset of μ_k . An illustration of this as well as the linear interpolator FIR structure is given in figure 6.15.

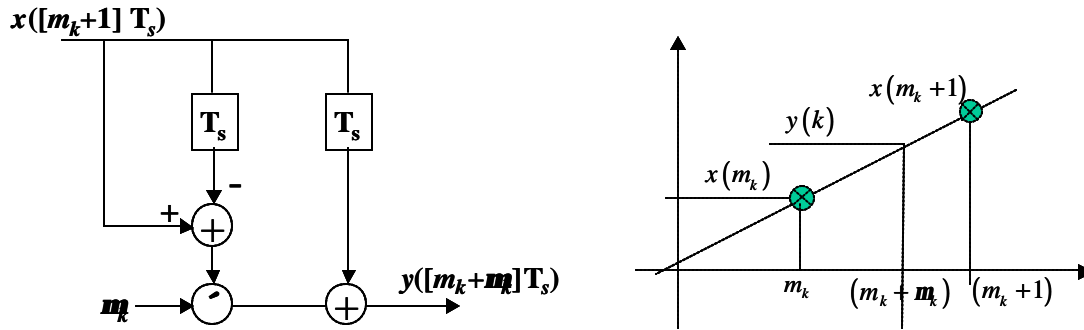


Figure 6.15: Linear Interpolation used in the synchronization scheme

6.3.2.1.2 Cubic Interpolation

A 3rd order polynomial with respect to μ_k whose coefficients are linear superposition of more than two samples. Figure 6.16 illustrates cubic interpolator based on 4 samples to create a single interpolant. The coefficients of the FIR filters are based on Lagrange coefficients and known as Farrow structure [87].

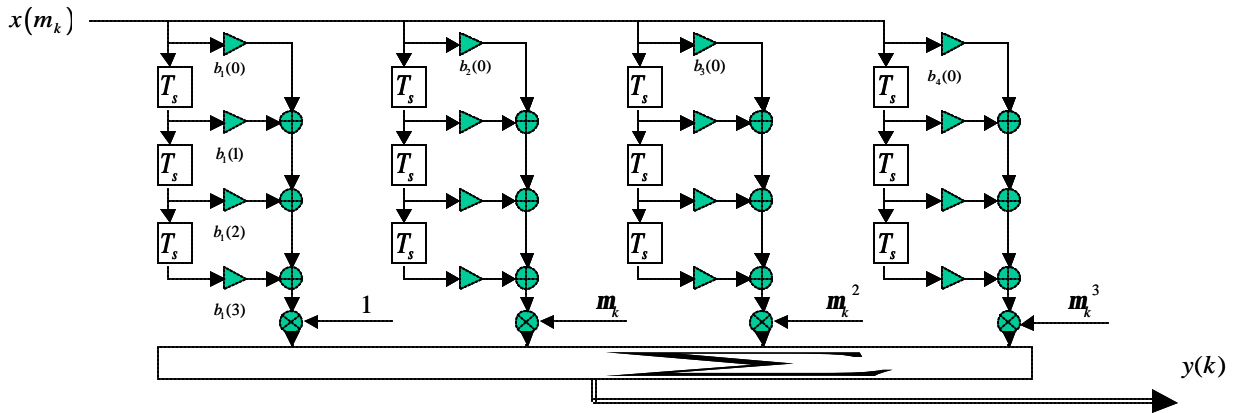


Figure 6.16: Cubic Interpolator based on Farrow structure

6.3.2.1.3 Linear vs. cubic interpolator

Comparing the two FIR structures in figures 6.15 and 6.16, cubic interpolator filter is much more complex than the linear interpolator. However, cubic interpolator is expected to perform better in the proposed synchronization scheme. Employing a polyphase implementation instead of direct form FIR structure can reduce the complexity of the cubic interpolator. More efficient implementation of the interpolator/decimator filter is a recommended future research issue.

6.3.2.2 TED

The TED algorithm is a data-aided version (employs a sliding correlator) of the Early-Late Gate originally developed by F.M. Gardner [84]. Two candidate algorithms were examined for post processing on the correlator output:

$$TED_1 = h_1 - h_{-1} \quad (6.12)$$

$$TED_2 = \sum_{i=1}^N (h_i - h_{-i}), \quad N = 4Q_o \quad (6.13)$$

The sliding correlator slides throughout the interpolator outputs to build estimates for “early”, “late” and “peak” hypothesis at the correlator output. “Early” samples are denoted by h_i and “late” samples are denoted by h_{-i} in (6.12) and (6.13). TED_1 criterion (6.12) is based on single early-late sample and thus has limited range of detectability. In order to increase the detector range, we have examined another criteria (TED_2), given in (6.13), which is based on the sum of N early-late gate samples. The error signal is passed through the loop filter (1st order IIR or higher order FIR) to average the effect of noise and to create reliable estimate for the timing delay.

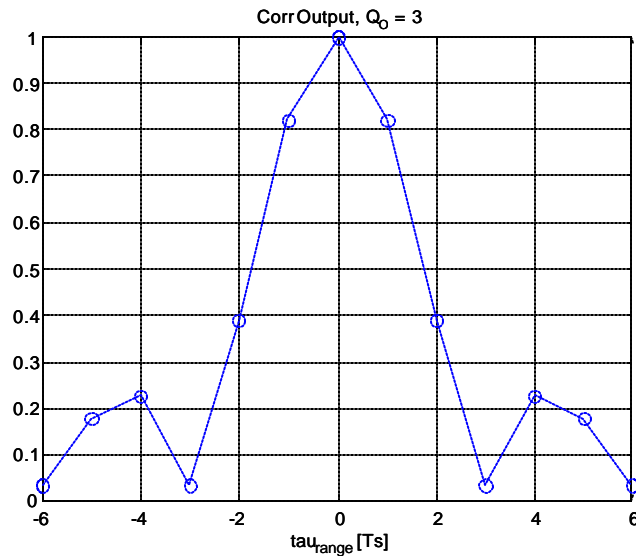


Figure 6.17: Sliding correlator output is symmetric at ideal sampling. Early-late detector produces zero output due to perfect match.

6.3.2.2.1 SINR Estimator

In order to make the DLL operation robust to high levels of noise, a “freeze” loop mechanism is developed. In other words, if the incoming received signal is highly corrupted by noise (e.g., $\text{SNR} < -15\text{dB}$), the control unit stops updating the m_k and \mathbf{m}_k estimates, i.e. control loop is said to be “frozen”. This prevents the interpolator/decimator from working on unreliable timing estimates. This “freeze” loop mechanism can be controlled by one of the following SINR criteria:

1. Correlator Peak Error

The threshold for freezing the DLL operation can be determined by just looking at the absolute error at the correlator peak output given below:

$$\text{SINR}_{est} = |h_{peak_index} - 1| \quad (6.14a)$$

2. Peak to Second Peak Ratio

This criterion is based on the cross correlation properties of the training sequence. It uses the ratio of the correlator peak and the second highest peak that is $\pm kQ_o$ samples away:

$$\text{SINR}_{est} = \frac{h_{peak_index}}{\max_{i \in \{peak_index \pm k \cdot Q_o\}} (h_i)}, \quad k \text{ is an integer} \quad (6.14b)$$

The second criterion was found to be more effective in choosing a distinct threshold. Figure 6.18 illustrates that the “peak to second peak ratio” criterion enables us to discriminate in between SINR’s of -20 dB and SINR’s of 0 , 5dB , 10dB while the “correlator peak error” criterion does not discriminate well between these states. Figure 6.18 also shows that the best threshold is found to be 2.8 (Peak/Second Peak) for $Q_o = 2$. This threshold value is different for different oversampling factors.

6.3.2.2.2 m_k estimator

The purpose of this estimator is to map the output of the TED, which is some function of the non-integer sample time delay, to a quantized estimate of the fractional time delay and feed this $\hat{\mathbf{m}}_k$ to the interpolator/decimator. This estimation can be done in two ways. The first one is to utilize the S -curve ROM look-up table to derive an estimate for \mathbf{m}_k . The second way is to use a “ \mathbf{m}_k searcher”. This searcher first creates n interpolants in between each two consecutive

samples. These interpolants correspond to n different hypothesis of \mathbf{m}_k . The searcher then picks the best hypothesis based on correlation. Figure 6.19 shows an example of the correlator peak at the output of the \mathbf{m}_k searcher. Here the resolution of \mathbf{m}_k ($\mathbf{m}_{k,res}$) is taken to be 0.2 of a sample. The same resolution is used in the simulations.

Comparing the two approaches for \mathbf{m}_k estimation, the S-curve approach is much more efficient, however it suffers from stability issues due to the memory of the loop filter. Second approach on the other hand, is a more complex but robust approach. One can easily see that increasing the resolution of the \mathbf{m}_k searcher will result in better fine-tuning. Simulation results will show that DLL with either a cubic or linear interpolator could still have some residual timing error due to this finite resolution of the \mathbf{m}_k searcher.

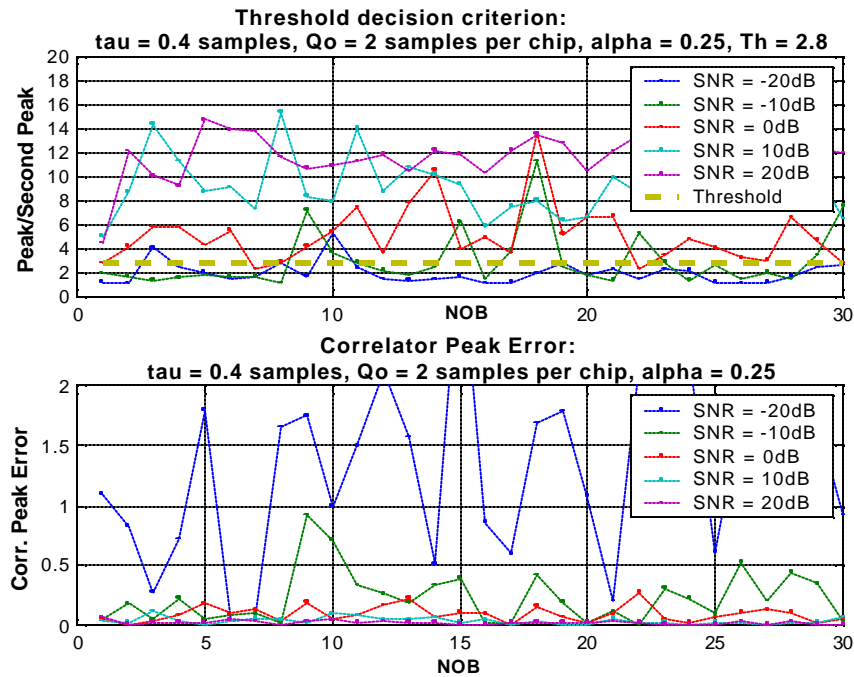


Figure 6.18: SINR Estimator Criteria to determine the threshold for the “freeze” loop mechanism. Peak/Second Peak criterion gives a more distinct threshold than the Correlator Peak Error criterion.

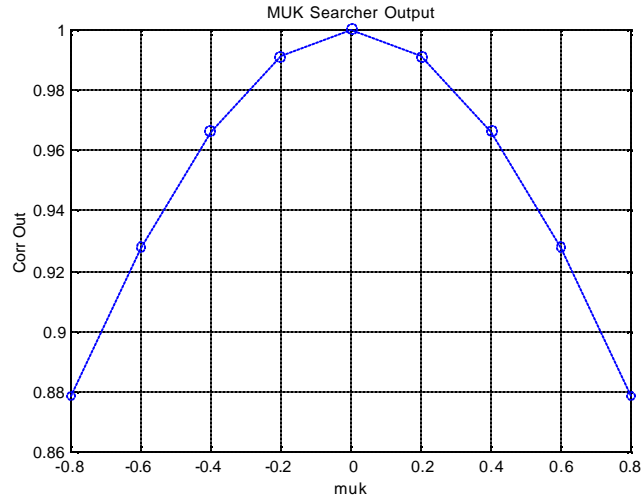


Figure 6.19: μ_k - searcher output. $\mu_{k,res} = 0.2$ of a sample. Quantized μ_k hypothesis

6.3.2.3 CONTROL ALGORITHM

The TED output is an averaged version of the Early-Late detector based on correlation of sequence of chips. This output is not the timing offset itself but a function of the timing offset, and can be expressed as $f(\tau)$. The objective of the control algorithm is to generate an estimation of the timing offsets based on the TED output $f(\tau)$.

S-curve Look-Up Table

As shown in figure 6.20, $f(\tau_{du})$ possesses an S-curve type relationships with the timing offset τ_{du} such that :

1. It is unbiased, i.e., has zero crossings at $\tau_{du} = 0$.
2. It has linear type shape for a range of $-t_{du,max} \leq t_{du} \leq t_{du,max}$.
3. It has symmetry with respect to $\tau_{du} = 0$ such that the sign indicates the direction of correction.

This S-curve is generated offline and quantized to create a look-up table that relates $f(\tau_{du})$ with τ_{du} . This is an efficient control algorithm since the quantized $f(\tau_{du})$ values, for a particular oversampling factor, are stored in a ROM only once. Figure 6.20 also illustrates the comparison between the two TED algorithms given in (6.12) and (6.13). TED₂ algorithm, which is given by (6.13), results in a more linear S-curve and more importantly there is no ambiguity in mapping

$f(\tau_{du})$ to a estimate of τ_{du} . Therefore, TED_2 results in a detectability range of $\pm T_{sym}$. On the other hand, conventional Early-Late detector, TED_1 given by (6.12), results in mapping ambiguity. For example, by looking at the blue curve in figure 6.20, $f(\tau_{du}) = 0.8$ corresponds to either $\hat{\tau}_{du} \approx 1.4 \text{ samples}$ or $\hat{\tau}_{du} \approx 2.5 \text{ samples}$. Due to these ambiguous regions, the detectability range of TED_1 is limited to approximately $\pm \frac{1}{3} T_{sym}$.

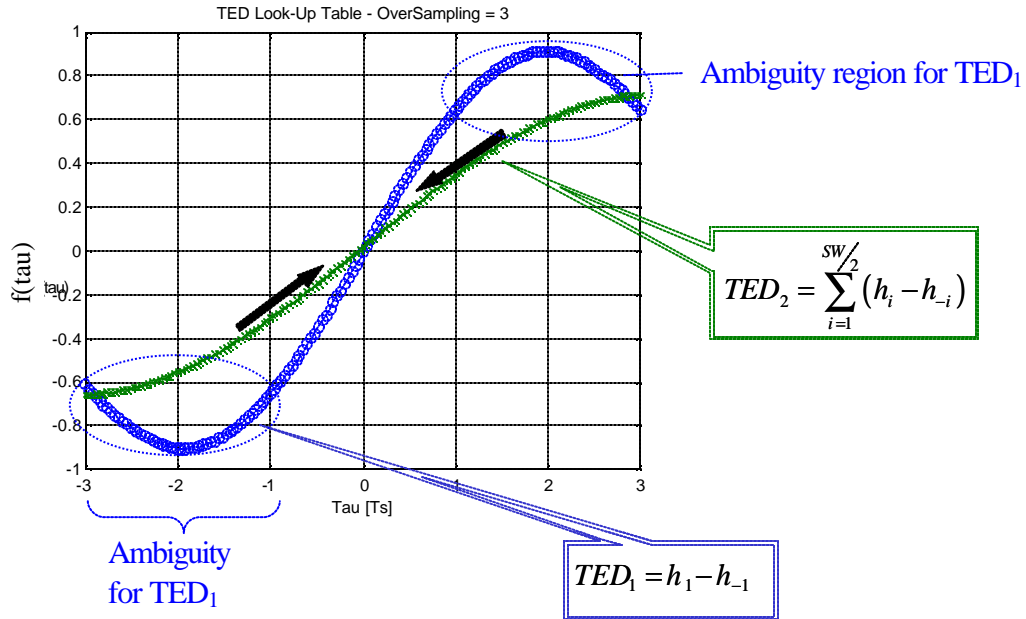


Figure 6.20: S-curves for TED_1 and TED_2 . TED_1 has a lower range of operation due to the ambiguous regions in mapping $f(\tau_{du})$ to a estimate of τ_{du} .

6.3.3 SIMULATION RESULTS

The performance of the proposed DLL was tested for six different structures:

1. DLL + ideal cubic interpolator, $Q_o = 2$ samples per chip (μ_k is assumed to be apriori known)
2. DLL + ideal linear interpolator, $Q_o = 2$ samples per chip (μ_k is assumed to be apriori known)
3. DLL + cubic interpolator with estimated μ_k , $Q_o = 2$ samples per chip
4. DLL + linear interpolator with estimated μ_k , $Q_o = 2$ samples per chip
5. DLL with no interpolator, $Q_o = 2$ samples per chip
6. DLL with no interpolator, $Q_o = 3$ samples per chip

The purpose of first two ideal interpolator structures is to obtain lower bounds on the performance of the DLL.

The following simulation results are based on loop filter forgetting factor of $\alpha = 0.25$ and block size of 31 known sequences with good cross correlation properties. The choice of α depends on a tradeoff between noise immunity and fast convergence, especially in low SNR scenarios. In our simulations, we fixed α to 0.25 which resulted in the best compromise.

Time delay of the desired user is assumed to be in the range of $\pm T_{\text{sym}}$ and constant over many training blocks (length of 31 bits). In realistic channel environments, propagation delay is time-varying and it is a function of the coherence time of the wireless channel. In our research effort, we model the channel as a stationary AWGN channel since our mere purpose is to design a general purpose DLL and show its “steady state” and “transient” characteristics for wide ranges of non-integer sample delays. DLL operation is said to reach steady state whenever the time delay to be estimated is a fraction of a sample ($|\tau_{\text{du}}| < T_{\text{sym}}/Q_o$). Transient behavior of DLL can be observed for non-integer (or integer) sample delays greater than one sample ($|\tau_{\text{du}}| > T_{\text{sym}}/Q_o$). DLL compensates for these delays by first locking on to the correct integer portion of the sample delay, i.e. adjusting the basepoint to the correct m_k , and then fine-tuning in between samples, using interpolator, to correct for the fractional sample delay, i.e. adjusting the basepoint to $m_k + \mathbf{m}_k$. Transient behavior of DLL determines the approximate number of known data (e.g. training sequences in TDMA systems or pilot sequences in CDMA-type systems) blocks required for convergence to a low and reliable delay estimate error. In other words, transient behavior of DLL gives an idea of the length of integration time in the loop filter.

Figures 6.21 and 6.22 depict the DLL performance in estimating a time delay of $\tau_{\text{du}} = 0.4$ samples. Results were averaged over 100 blocks. Performance of DLL using all of the above mentioned 6 structures were compared. Figure 6.21 shows that the mean squared error (MSE) of the TED output decreases with an increasing SNR (E_s/N_o). Zooming in the positive SNR region, we can see that the performance of DLL with cubic interpolator ($Q_o = 2$) approaches to the performance of the ideal cases. In other words, cubic interpolator successfully fine-tunes in between samples and DLL correctly estimates and completely compensates for the fractional delay. This zoomed figure also illustrates that there is an irreducible error floor for the no interpolator cases due to the residual timing error. As expected, no interpolator case with $Q_o = 3$ samples/symbol outperforms the one with $Q_o = 2$ samples per symbol.

In wideband systems, e.g. WCDMA, symbol decisions are made at the peak of the correlator output after de-spreading. Consequently, correlator peak error is a good measure of performance for the DLL operating in wideband systems. Figure 6.22 shows the MSE of the correlator output peak, which is less than 0.1 for $\text{SNR} > -10\text{dB}$. An interesting behavior is observed at $\text{SNR} > 0\text{dB}$: all 6 versions of DLL result in very close correlator peak MSE. This result suggests that in *single-user delay estimation/synchronization* for wideband applications, we can get away with using a low-complexity DLL without an interpolator (with $Q_o = 2$ samples per chip). This conclusion may not be true for the *multi-user* case, which is an area of further research.

In narrowband cases, effect of residual timing error in single-user delay estimation / synchronization algorithm depends on the common air interface. In other words, particular system's sensitivity to small timing offsets (maximum delay estimation error of $0.5T_s$ for DLL with no interpolator and $Q_o = 2$) determines whether an interpolator is needed or not. However, in the multi-user scenarios, similar to the wideband case, either a joint detection or interference rejection algorithm that separates the multi-user signals follows proposed DLL. In such structures, even a small residual timing error could result in non-negligible performance degradation data detection.

Although cubic interpolator gives the best fine-tuning at $\text{SNR} > -10\text{dB}$, its performance is limited by the finite resolution of the μ_k searcher. In other words, DLL with cubic interpolator may still result in a small residual timing error. However, as can be seen from figure 6.23, this residual error is negligible, i.e. for $\tau_{du} = -0.48$ samples the MSE of the TED output is less than 0.01 for $\text{SNR} \geq 5\text{dB}$.

Finally, the transient response of the DLL with cubic interpolator was analyzed for a time delay of $\tau_{du} = 1.8$ samples ($1.8/2 = 0.9 T_{\text{sym}}$) and the results are depicted in figure 6.24. The top portion of the figure shows that the absolute delay estimation error is less than 0.5 of a sample for $\text{SNR} \geq -5\text{dB}$ and $\text{NOB} > 7$ blocks. The bottom figure shows that the loop filter output is in the range of $\{-0.1, 0.1\}$ for $\text{SNR} \geq 0 \text{ dB}$.

6.3.4 SUMMARY OF DLL RESULTS

The simulation results in section 6.3.3 show that the proposed DLL structure (with or without an interpolator) can successfully estimate and compensate for any integer timing offset within the

range of $-T_{\text{sym}} \leq \tau \leq T_{\text{sym}}$ for $\text{SNR} > -5\text{dB}$. The convergence time during the “transient” stage depends on the loop filter’s forgetting factor, α . We demonstrated that with an $\alpha = 0.25$ and a block size of 31 known data sequences, DLL locks to the right timing after operating on approximately 7 blocks. A very important feature of the proposed DLL is that, with the help of a linear or cubic interpolator, it can compensate for any *non-integer* sample delay with some negligible quantization error in the μ_k searcher. Furthermore, DLL can achieve this performance only with 2 samples per symbol. Cubic interpolator was shown to be more effective than linear interpolator in fine-tuning the fractional sample delay estimates.

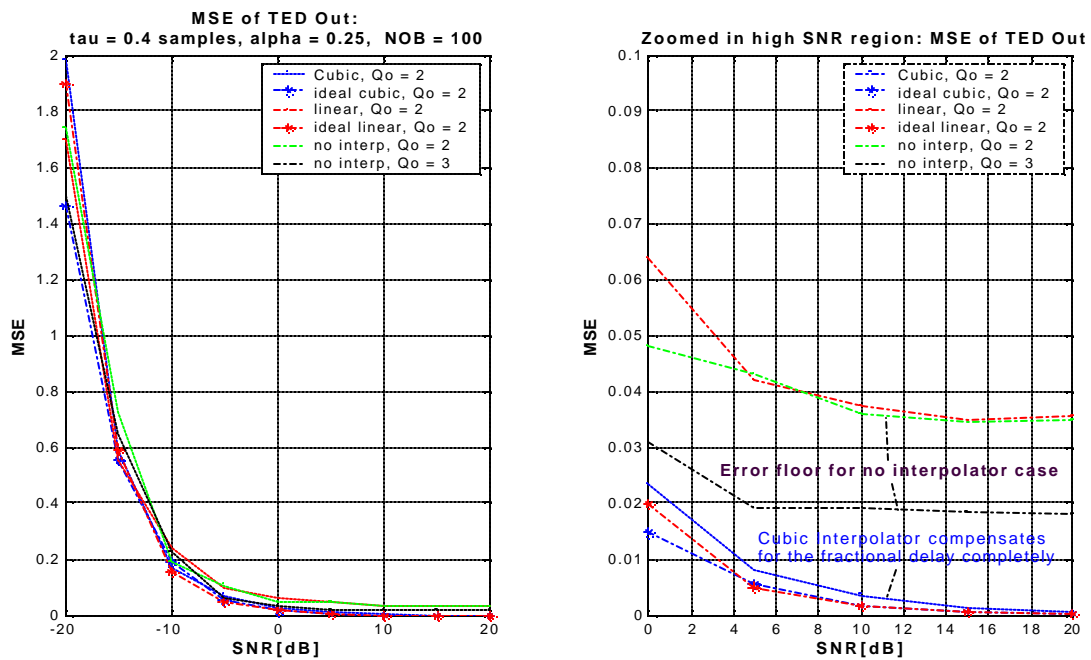


Figure 6.21: MSE of TED output for $\tau = 0.4$ samples. TED output MSE decreases with increasing SNR. Cubic interpolator with $Q_o = 2$ samples per symbol. Completely compensates for 0.4 fractional delay. Error floor for no interpolator case can be seen in the zoomed version of the figure.

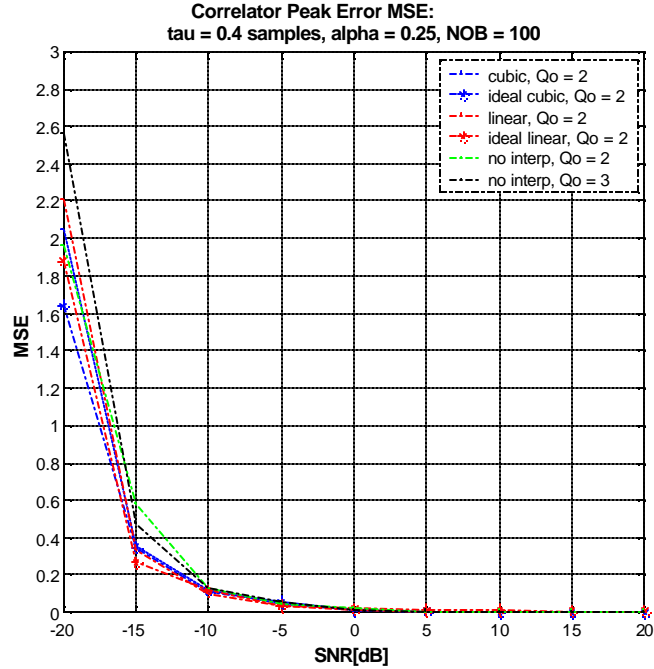


Figure 6.22: Correlator Peak Error MSE for $\tau = 0.4$ samples. For $\text{SNR} > -10\text{dB}$, $\text{MSE} < 0.1$ (for all 6 cases). Peak is close to 1. Cubic interpolator gives the lowest MSE.

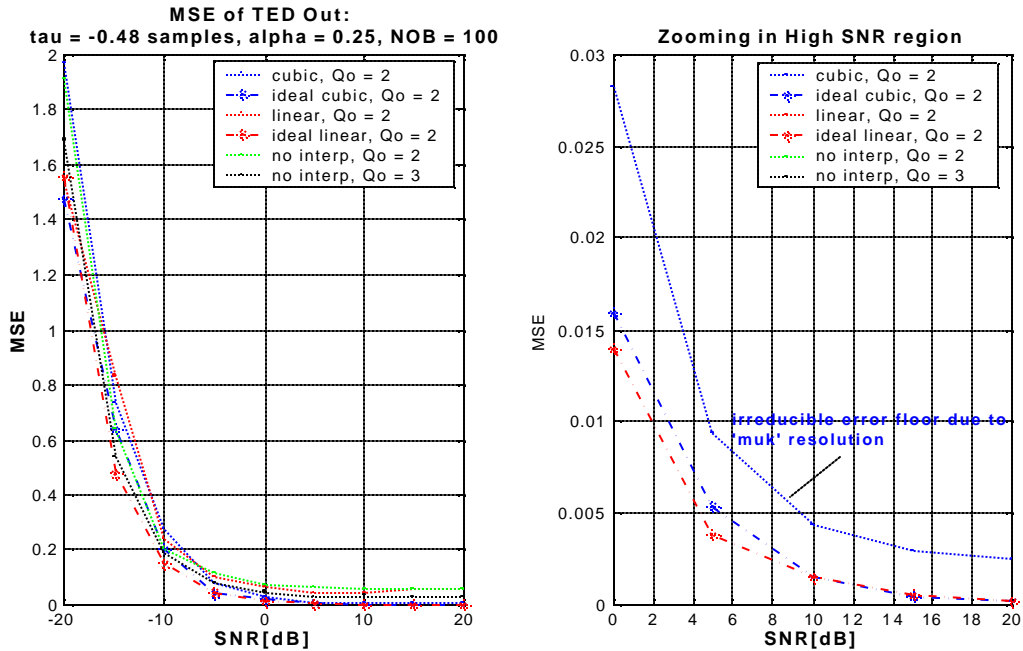


Figure 6.23: MSE of TED output for delay of -0.48 samples. Interpolator performance is limited by the ' $\mu_{k,\text{res}}$ '. Cubic interpolator still gives the best 'fine tuning'.

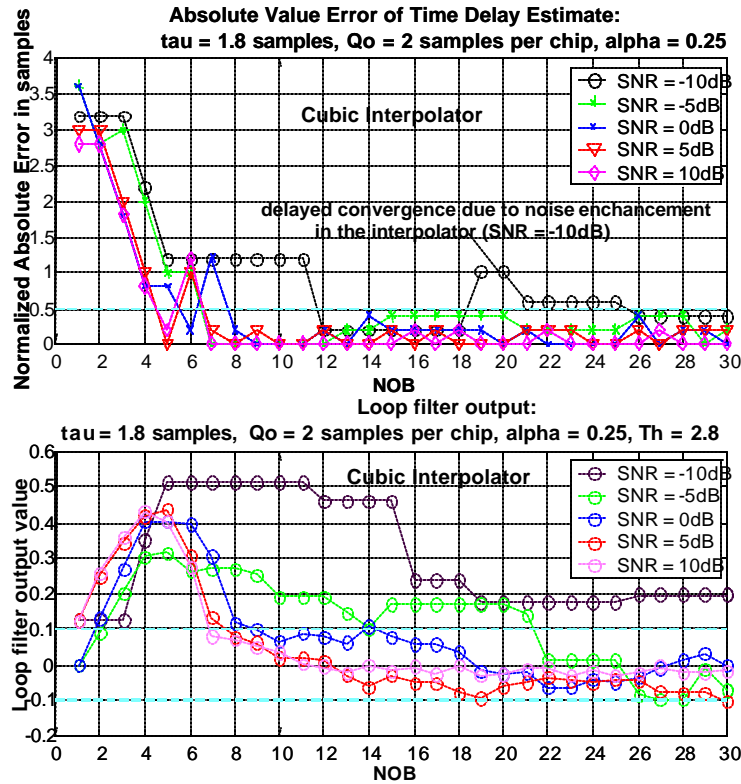


Figure 6.24: Transient behavior of the DLL. For $\text{SNR} \geq -5\text{dB}$ & $\text{NOB} > 7$ blocks: $|\tau - \tau_{\text{est}}| < 0.5$ samples and $-0.1 < \text{Loop filter output} < 0.1$

6.4 SUMMARY OF THE MULTI-USER TIME DELAY ESTIMATION RESEARCH EFFORT

As mentioned in Section 6.1, multi-user time delay estimation is a very crucial aspect of overloaded array processing. In real channel environments, the user signals arrive at the airborne receive-antenna with different unknown time delays. The receiver has to first reliably estimate these time-delays before carrying out the signal extraction. As discussed in Section 6.1, we propose to embed a low-complexity data-aided delay estimation / synchronization algorithm in a blind PSP trellis. PSP is a very powerful sequence as well as channel estimation technique with a high computational complexity. Therefore, a sub-optimal but very low-complexity delay estimation structure has to be developed. This structure is discussed in Section 6.2, which concludes that multi-user delay estimation problem is separable and can be tackled with a sub-optimal single-user delay estimation structure.

Section 6.3 analyzes the performance of the proposed low-complexity delay estimation structure, the DLL. This algorithm was shown to successfully estimate and compensate for single-user time delays (both integer and non-integer sample delay) within the range of $\pm T_{\text{sym}}$. Depending on the application and the complexity requirements of the overall system, the proposed DLL structure can incorporate an interpolator for fine-tuning the delay estimates. Simulation results demonstrated that, at a low oversampling rate of $Q_b = 2$ samples per symbol, DLL with a cubic interpolator could correctly estimate (with some negligible quantization error) any non-integer sample delay within few blocks of training data. This result has two practical outcomes. First outcome is that, A/D requirements are relaxed due to the low oversampling rate. Second outcome is that the loop filter's integration time is low, i.e. estimation error converges to zero within several training blocks.

In some applications, for example in single-user delay estimation for wideband systems, DLL without an interpolator can achieve acceptable delay estimation performance with only 2 samples per chip. In such cases, the worst-case delay estimation error is found to be 0.5 of a sample.

Although interpolator adds to the overall complexity, it is expected to be a crucial part of the DLL structure for *multi-user* scenarios. Two approaches can be taken to extend this single-user delay estimation/synchronization structure to a multi-user scheme:

1. Use a bank of Du DLLs (with interpolator) to estimate the time delay of each one of the Du users in a parallel fashion as shown in figure 6.25. In this case, the input to each DLL consists of samples of sum of all users' received signals plus AWGN. The sliding correlator in the TED of d^{th} DLL correlates the received signal samples (SOI + CCI + AWGN) with the known symbol sequence of the d^{th} user in order to estimate t_d . It is expected that, this multi-user structure can successfully estimate the delays of the users as long as the known symbol sequence of each user has good cross-correlation properties.
2. Use bank of Du DLLs with adaptive pre-filters up front. The structure for the single-user case was depicted in figure 6.12 of Section 6.3. Multi-user version of this structure is given in figure 6.26. At each DLL bank, first perform interference rejection using an adaptive pre-filter, \mathbf{F} , and then estimate the time-delay of the SOI using the proposed DLL.

The first multi-user structure is expected to perform well given that the known symbol sequence of each user possesses good correlation properties. Thus, this structure may be more applicable

to wideband systems. Consequently, Section 6.5 provides the simulation results for the interpolator-based DA timing recovery scheme for multi-user CDMA systems, i.e., multi-user time delay estimation using bank of DLLs.

The second multi-user structure is more appropriate for TDMA-type systems since the training sequences are not designed to have good cross-correlation properties. This structure is expected to have a much higher complexity than the first one due to the introduction of adaptive pre-filters. However, it is also expected to outperform the other one whenever the known user sequences have poor cross-correlation properties. The challenging part about the second multi-user structure is to come up with a robust and efficient adaptive interference rejection filter. This remains a future area of research.

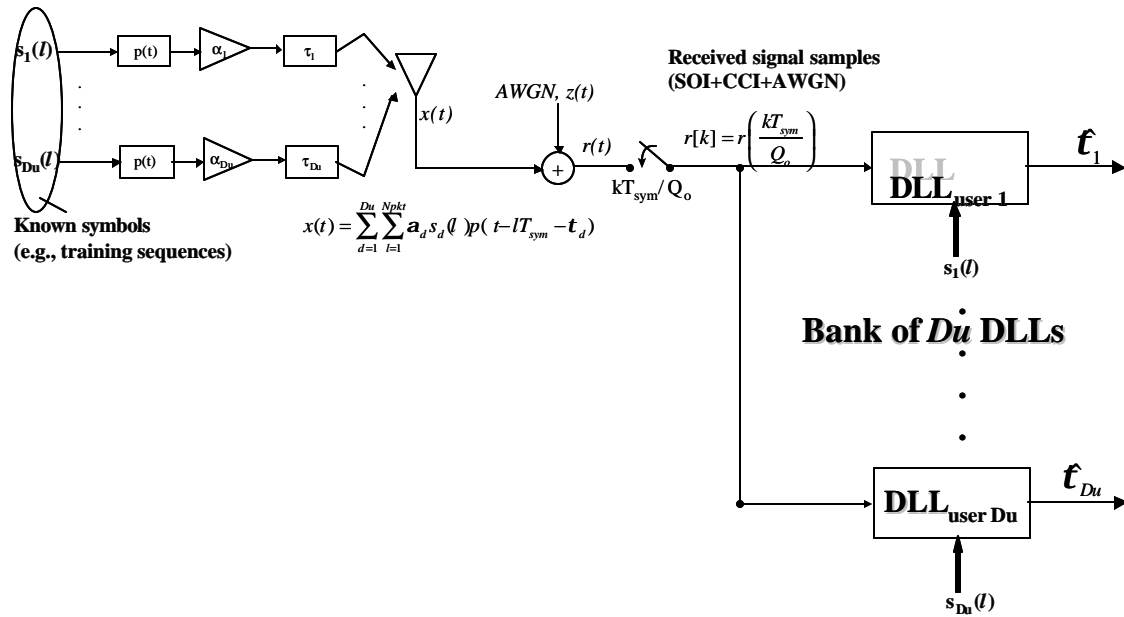


Figure 6.25: Possible multi-user delay estimation algorithm structure 1. Parallel bank of D_u DLL structures that simultaneously estimates the time delays of D_u user signals. This scheme is expected to work well given that the known symbol sequences of D_u users have good correlation properties.

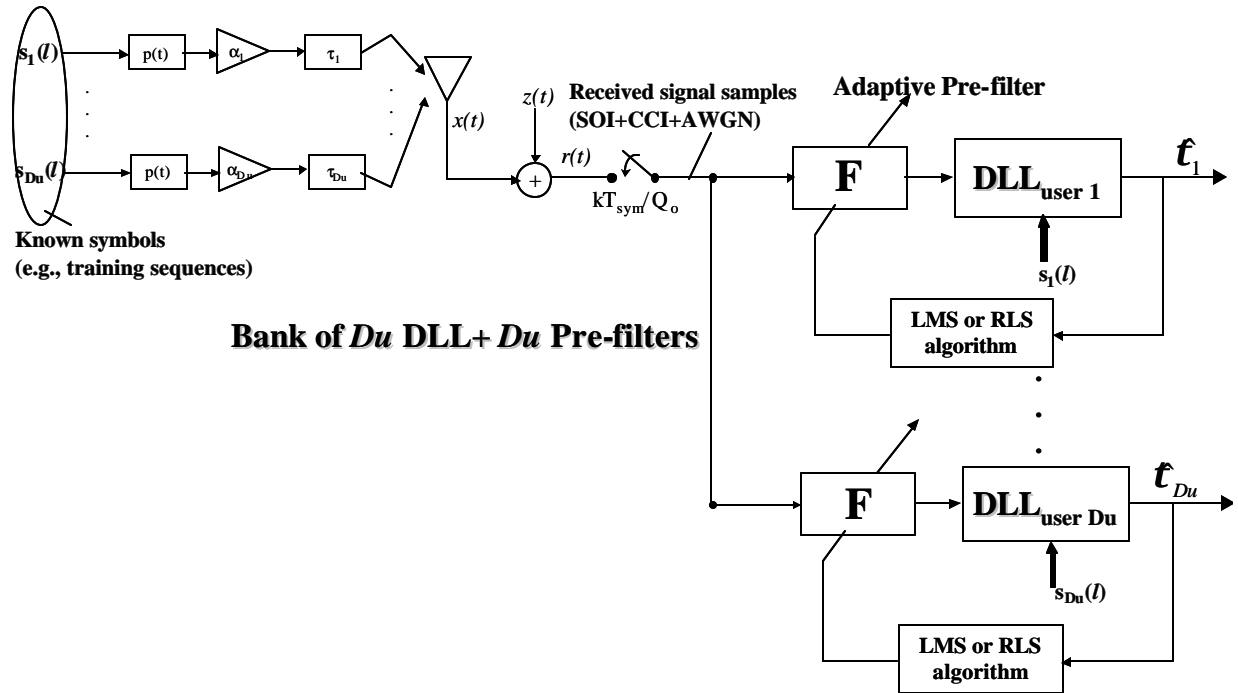


Figure 6.26: Possible multi-user delay estimation algorithm structure 2. Parallel bank of D_u DLL + D_u adaptive pre-filter structure. Adaptive filter suppresses the interference at each bank and “clean” signal is then operated by the DLL to estimate the delay.

6.5 INTERPOLATION BASED DA-TIMING RECOVERY SCHEME FOR MULTI-USER CDMA RECEIVERS

6.5.1 MULTI-USER DLL SIMULATION ARCHITECTURE

Single user synchronization is carried out using a single DLL as shown in Section 6.3. This structure can be extended to the multi-user case by employing a parallel bank of the proposed DLLs as shown in figure 6.25. As mentioned in Section 6.4, this structure is more applicable to CDMA-type systems. Thus, the proposed multi-user structure, shown in figure 6.27, is designed to simultaneously estimate the multi-user delays by exploiting the good cross-correlation properties of each user's PN-code. The received signal is composed of signal of interest (SOI) and Multiple Access Interference (MAI) waveforms. Thus, the TED at the k^{th} DLL branch incorporates a sliding correlator that correlates the received noisy signal (SOI+MAI+AWGN) with the k^{th} user's PN-code in order to estimate its time delay, t_k . The following section provides the simulation results for the proposed multi-user DLL architecture.

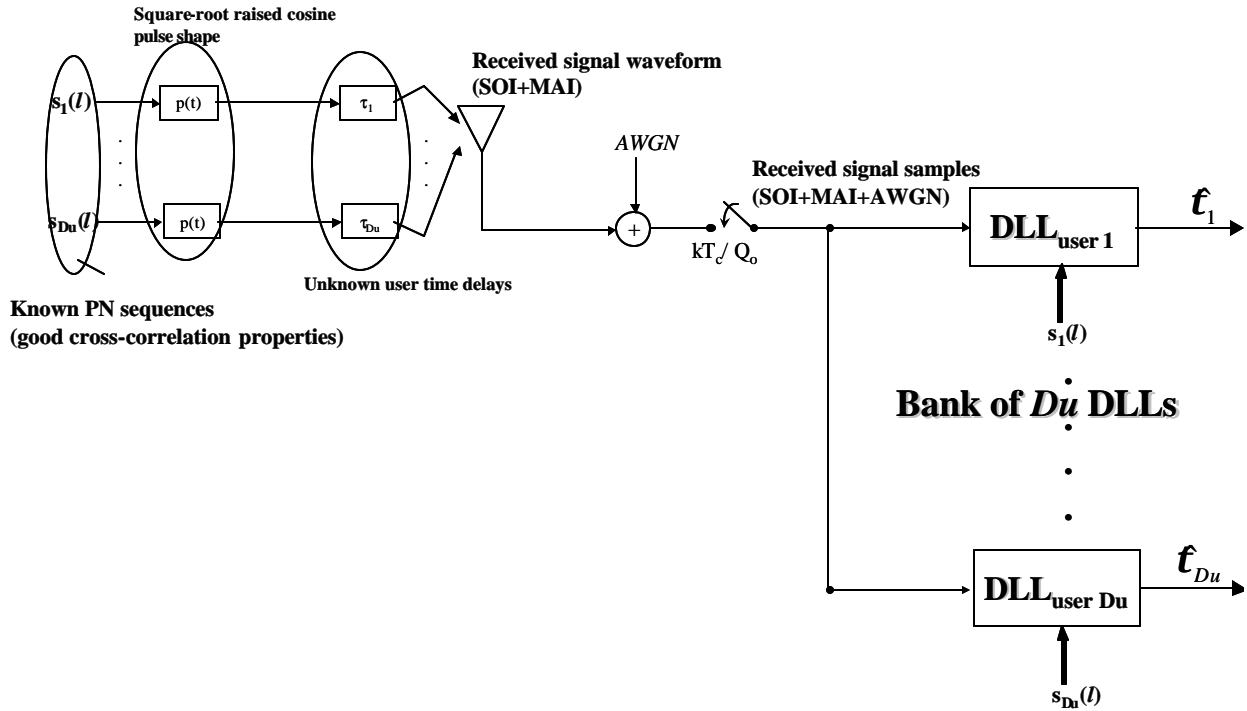


Figure 6.27: Proposed Multi-user Synchronization Scheme for CDMA receivers.

6.5.2 MULTI-USER DLL SIMULATION RESULTS

The proposed scheme has been examined for the multi-user case with a spreading factor of 31, where the number of users ranges from 1 to 6. Each user is assigned with a PN-code, which has good auto-correlation as well as cross-correlation properties. We assume asynchronous system where each user has its own distinct time delay. We also assume that code acquisition has been achieved such that the timing offset of each user is within a chip relative to the initial base point obtained by the code acquisition. We refer to [200] where the sensitivity of Direct Sequence CDMA (DS-SS-CDMA) interference cancellation techniques to timing errors has been explored. It was shown that timing error of $0.2 T_c$ (where T_c is the chip duration) introduces a significant degradation to the performance of proposed interference cancellation schemes. This introduces a stringent requirement to the accuracy of the timing recovery scheme. We investigate the tradeoff between high oversampling factor schemes ($Q_0 = 3,4$) without an interpolator and a low oversampling factor scheme ($Q_0 = 2$) with an interpolation processing.

Figure 6.28 illustrates the averaged timing error of the desired user as a function of SNR for the following four structures: $Q_0=2$ with cubic interpolator and $Q_0 = 2,3$ & 4 without an interpolator.

The time delay of the desired user is fixed at $t_{du} = 0.4 T_s$, where the time delays of the other 5 users are randomized in Monte Carlo simulation.

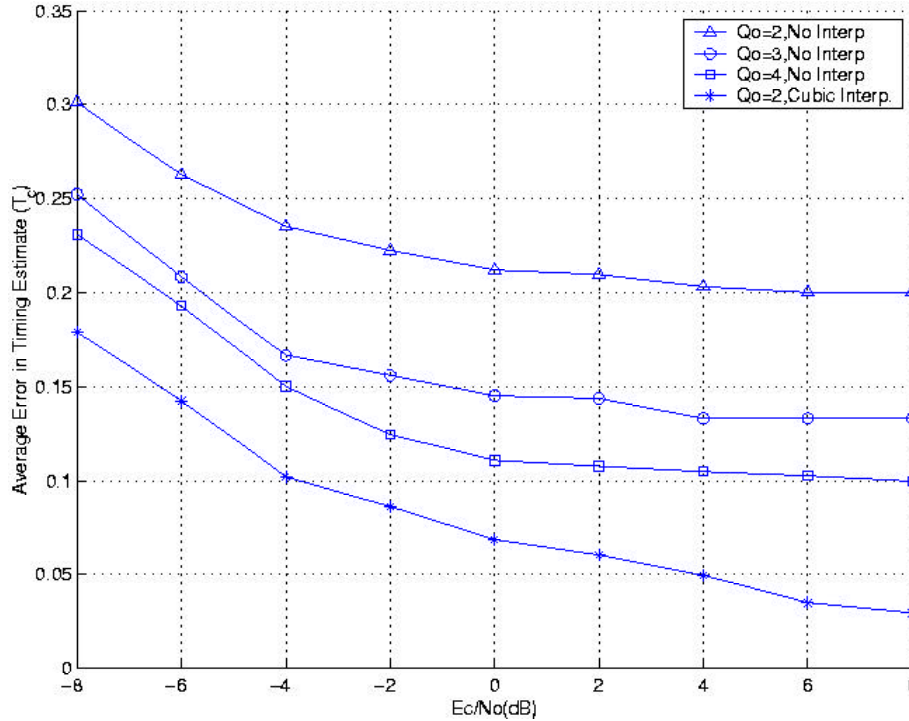


Figure 6.28: Comparison of 4 different DLL structures in multi-user synchronization scheme. Averaged timing error in T_c (users = 6, spreading gain = 31, $\tau_{du} = 0.4 T_s$)

It can be seen that $Q_o = 2$ with cubic interpolator outperforms the other 3 structures. In addition, this scheme results in a timing error that is lower than $0.125 T_c$ for $E_c/N_0 \geq -5\text{dB}$ and thus meets the requirements of [200]. Furthermore, the schemes without an interpolator suffer from an irreducible timing error, which is a function of Q_o and the initial timing error (0.4 of a sample). As expected, the residual error is reduced as Q_o increases.

Figure 6.29 examines the effect of Multiple Access Interference (MAI) on the performance of the proposed scheme. The upper plot demonstrates that the timing error detection is not sensitive to the increasing number of users. This is due to the good cross-correlation properties among different users, which preserve the symmetry properties of the correlator output and thus does not affect the early-late gate detector. However, the lower plot depicts the degradation of the

correlator output peak as the number of MAI increases, which illustrates the expected degradation in data detection.

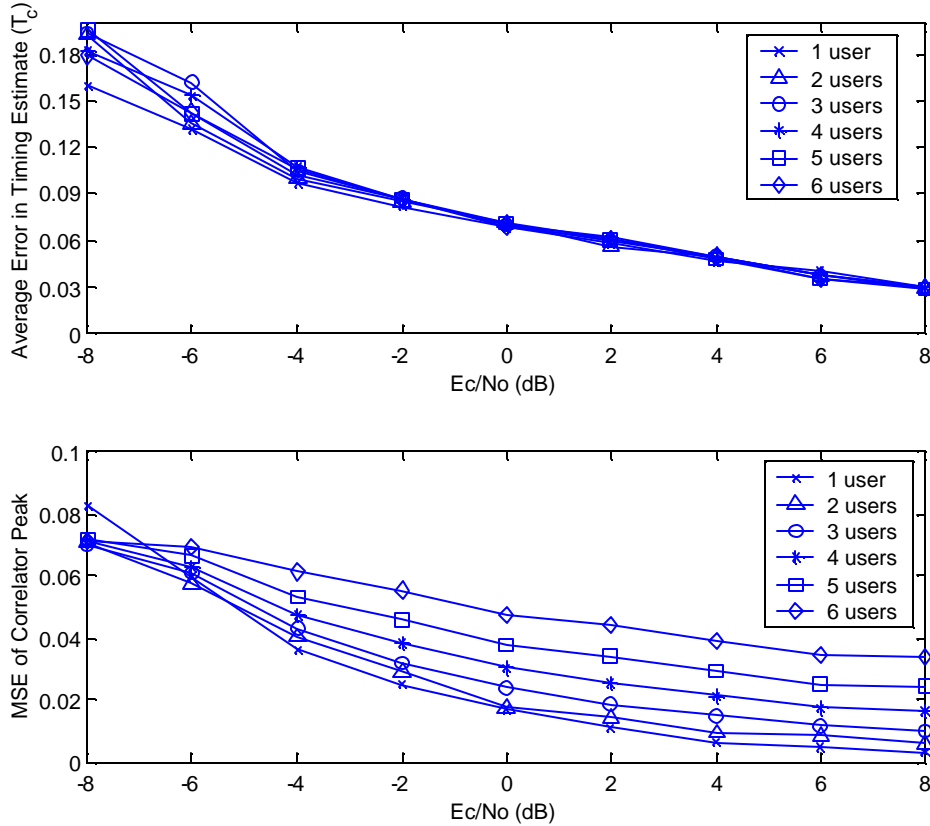


Figure 6.29: The effect of Multiple Access Interference (MAI) on the performance of the proposed multi-user DLL scheme for CDMA systems.

Figure 6.30 demonstrates the operation of the bank of DLLs for the selected scheme of $Q_o=2$ with a cubic interpolator. We set the timing offsets of the users to the following set: $t = [-1, -0.6, -0.2, 0.2, 0.6, 1] T_c$ for users 1, ..., 6, respectively with respect to the initial base points obtained from the code acquisition¹. It can be seen that the scheme simultaneously tracks the timing offset of each user.

¹ We assume that code acquisition has already been done such that the timing offset is within the range of a chip from the ideal timing strobe. Thus, each DLL picks the best phase out of Q_o phases and interpolates in between samples to compensate for a fractional timing

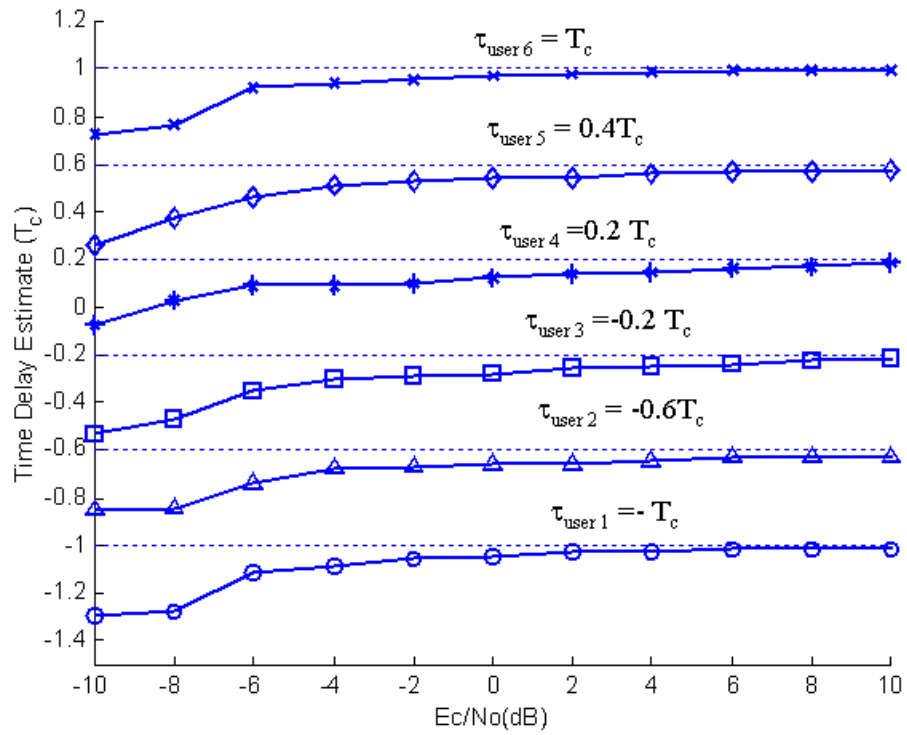


Figure 6.30: Simultaneous time delay estimation of 6 users' timing ($\tau = [-1, -0.6, -0.2, 0.2, 0.6, 1] T_c$) with the selected configuration of $Q_o = 2$ with a cubic interpolator

CHAPTER 7: CONCLUSIONS AND FUTURE WORK

This thesis encompasses system-level and algorithm-level research findings for airborne communication systems. System analysis defined the overloaded interference environment experienced by an airborne repeater in terms of geometry, Doppler effects and link budgets. The goal of this preliminary system analysis was not to come with an extensive airborne channel model but rather to get a rough idea about the interference scenario. The results of link budget analysis demonstrated that the airborne receiver faces the challenge of extracting desired user signals out of a harsh co-channel interference environment; where the number of CCIs are well above the number of receive antenna elements. Doppler analysis showed that, the received signals at the receiver experience high Doppler shifts (300-600Hz) due to the motion of the repeater. This implies that a robust carrier recover scheme has to be employed at the airborne receiver. In short, the overall system analysis results showed that powerful signal processing techniques must be used in order to extract desired signals from overloaded environments. The results of this analysis can be used as a reference for future research in defining robust geometry-based airborne channel models that incorporate Doppler effects, large scale fading as well as small scale fading.

Algorithm-level accomplishments of this research effort can be broken down into three categories: literature survey results, simulation results of three signal extraction algorithms assuming benign channel conditions, and multi-user time delay estimation techniques for the channel estimation research effort.

Extensive literature survey on narrowband signal extraction algorithms have shown that, joint detection techniques outperform interference rejection techniques in severe interference environments at the price of increased complexity. The JMAP receiver was found to be the optimum solution for narrowband signal extraction in overloaded scenarios. The literature survey also showed that joint detection schemes coupled with antenna arrays lie in the heart of overloaded array processing.

Encouraged by the literature survey results, three different joint detection algorithms were simulated and compared. The first algorithm, MU-DFE, was shown to simultaneously separate

multiple synchronous user symbols using a bank of MMSE beamformers built-in the MIMO feedforward filter. Similarly, the second algorithm, ILSP, was shown to extract user signals using the implicit ML beamformer solution in its iterative channel estimation / symbol estimation scheme. The performance of both MU-DFE and ILSP algorithms are limited by the array size, therefore, these algorithms failed in overloaded scenarios. Another drawback of these algorithms is their sensitivity to the angular spacing of the users. Even in underloaded scenarios, their signal extraction performance was shown to degrade when the user signals are closely spaced. Final algorithm, ILSE, is a true ML joint detection algorithm that provides an optimum solution for the overloaded antenna array scenarios in the presence of AWGN channel with no frequency selective multipath. ILSE processor with an m -element antenna array was shown to successfully demodulate up to m^2 multiple co-channel synchronous signals, assuming that the antenna array is perfectly calibrated. Unlike MU-DFE and ILSP, the performance of ILSE is not sensitive to the user spacing. In fact, ILSE was shown to successfully separate very closely spaced equal-power users even when the channel is not known. Specifically, the simulation results have shown that ILSE processor employing either training-based (with short training sequences) and blind channel estimation performs as good as ILSE with apriori known channel. In addition, the overloaded array performance of ILSE was shown to improve further when the users are of un-equal powers. The main drawback of ILSE is its prohibitive computational complexity, which is on the order of $O(NmdL^d)$ flops per iteration. However, even though ILSE is not a practical solution to the overloaded signal extraction problem, it provides a theoretical baseline for future work. Sub-optimal techniques to replace the ML brute force is an open research issue in overloaded array processing.

The final contribution of this thesis is the analysis of multi-user delay estimation problem as part of the channel estimation research effort. Initial analysis has shown that multi-user delay estimation problem is separable, and can be solved by employing less complex single-user delay estimation algorithms. For this reason, a low-complexity DLL was designed to operate at sampling rates as low as 2 samples per symbol, and was shown to estimate and compensate for any non-integer sample delay with negligible quantization error. The DLL structure also employs a “freeze” loop mechanism in order to make it more robust to extremely low SNR scenarios. The proposed DLL provides a practical solution to the single-user delay estimation /

synchronization problem. This single-user DLL structure was then extended to multi-user case where we have proposed a timing recovery technique for multi-user CDMA receivers that reduces the oversampling factor without introducing performance degradation. We showed that for spreading gain of 31, oversampling factor of 2 samples per chip with a cubic interpolator outperforms the case of oversampling factor of 4 samples per chip without an interpolator. Thus, the requirements of the A/D converter can be relaxed in the expense of increased computational complexity due to interpolation processing. We also showed that the proposed scheme meets the requirements for residual worst-case timing errors of multi-user interference cancellation techniques.

The proposed multi-user DLL scheme was shown to perform well in CDMA-type systems, since it exploits the good cross-correlation properties of the user PN-codes. Therefore, this scheme is expected to perform poorly in TDMA type environments due to the absence of spreading gain. In this respect, the thesis proposes another possible structure that utilizes DLLs in a multi-user delay estimation scheme for narrowband TDMA-type systems. Simulation and analysis of this proposed scheme remain as a further research issue.

APPENDIX A: PHYSICAL ENVIRONMENT CALCULATIONS

A.1 SPHERICAL EARTH MODEL

Airborne repeater is loitering above the spherical earth at an altitude of h .

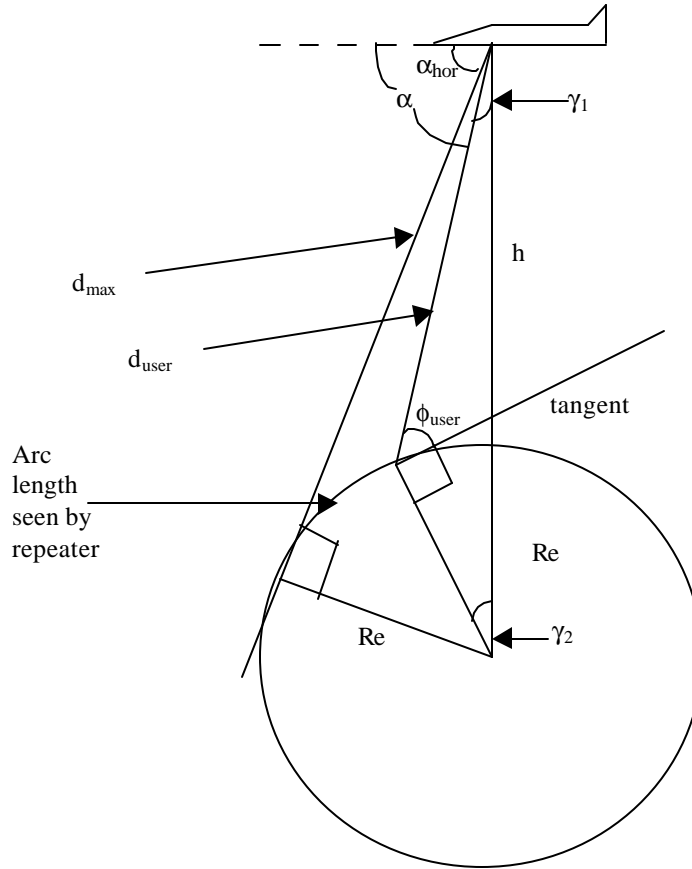


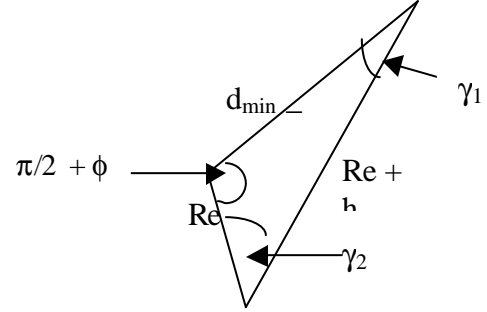
Figure A.1: Geometry of the ACN. The spherical earth model is assumed in these calculations.

In order to calculate the arc length seen by the repeater we need to calculate d_{max} (maximum horizon distance) and d_{user} (the slant distance to the user of interest).

To find these distances we apply the sine rule on the following triangle:

$$\frac{Re}{\sin g_1} = \frac{Re+h}{\sin \left(\frac{p}{2} + f \right)}$$

$$g_1 = \sin^{-1} \left(\frac{Re \sin \left(\frac{p}{2} + f \right)}{Re+h} \right) \quad (A.1a)$$



$$g_2 = p - \left(\frac{p}{2} + f \right) - g_1 \quad (A.1b)$$

Using the sine rule again we can find the slant distance to any user on the earth's curved surface

$$d_{user} = (Re+h) \frac{\sin g_2}{\sin \left(\frac{p}{2} + f_{user} \right)} \quad (A.2)$$

Finally, the maximum horizon distance can be found by using Pythagorean theorem:

$$d_{max} = \sqrt{(Re+h)^2 - Re^2} \quad (A.3)$$

A.2 DEPRESSION ANGLES

Horizon angle, α_{hor} , is the minimum depression angle possible:

$$\alpha_{hor} = \frac{p}{2} - \sin^{-1} \left(\frac{Re}{Re+h} \right) \quad (A.4)$$

The maximum depression angle depends on the maximum elevation angle as well as the altitude:

$$\alpha_{dep} = \frac{p}{2} - g_1 \quad (A.5)$$

where γ_1 is calculated in (A.1)

Table A.1 shows the user elevation angles, ϕ_{user} and the corresponding aircraft depression angles, α_{dep} . The altitude is fixed at 40,000 ft. The spherical earth model is used to obtain the results.

Table A.1: User elevation angles and corresponding aircraft depression angles using the spherical earth model

User elevation angle, degrees	Aircraft depression angle, degrees
0	3.54
1	3.68
2	4.07
3	4.64
4	5.34
5	6.12
6	6.96
7	7.84
8	8.74
9	9.67
10	10.6

A.3 ANGULAR SPACING BETWEEN TWO CO-CHANNEL CELLS

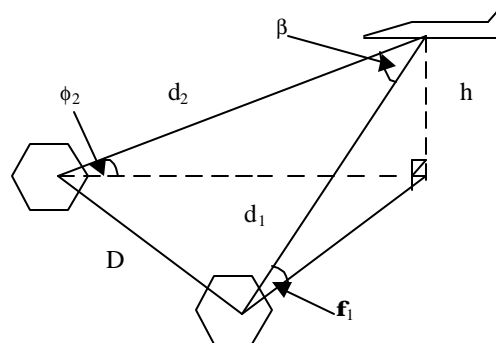


Figure A.2 Flat Earth Model. A desired user and an interferer are visible by the aircraft.

A flat earth model is used to calculate the angular spacing, β , in terms of altitude and elevation angles of the two co-channel users. Assuming both cells have the same size, the frequency reuse distance, D , can be expressed as: $D = \sqrt{3K} R_{cell}$ where K is the frequency reuse factor.

The horizon distances from the center of each co-channel cell to the repeater are d_1 and d_2 . These are computed as:

$$d_1 = \frac{h}{\sin \mathbf{a}_1} \quad (\text{A.6a})$$

$$d_2 = \frac{h}{\sin \mathbf{a}_2} \quad (\text{A.6b})$$

From this we can calculate the angular separation, β , by applying the cosine rule as follows:

$$D^2 = d_1^2 + d_2^2 - 2d_1d_2 \cos \mathbf{b} \quad (\text{A.7a})$$

$$\mathbf{b} = \cos^{-1} \left(\frac{d_1^2 + d_2^2 - D}{d_1d_2} \right) \quad (\text{A.7b})$$

The resulting angular spacing depends on the altitude of the repeater, elevation angles and the frequency reuse distance between the two co-channel cells.

A.4 VIEWABLE AREA AND MAXIMUM NUMBER OF CO-CHANNEL CELLS

The repeater overlooks an annulus-shaped region of users at any instance of time as shown in Chapter 1. The range of view depends on the azimuth angle, repeater altitude and the location of the nearest co-channel cell.

$$Area = \frac{1}{2} \mathbf{q} (d_{\max} + d_{\min}) \quad (\text{A.8})$$

where d_{\min} and d_{\max} are calculated using A.3 and A.4 respectively.

Maximum number of co-channel cells can then be calculated assuming all the desired users and interferers are located in the annulus shaped region.

$$Cells_{total} = \frac{Area \text{ of annulus}}{Area \text{ of a cell}} = \frac{\frac{1}{2} \mathbf{q} (d_{\max} + d_{\min}) (d_{\max} - d_{\min})}{2.59808 R_{cell}^2} \quad (\text{A.9a})$$

$$N_{\max} = \frac{Cells_{total}}{reuse\ factor} - 1 \quad (\text{A.9b})$$

APPENDIX B: LINK BUDGET CALCULATIONS

B.1 LINK BUDGETS

We have done the link budget analysis by using two different propagation models: One-ray model (modeling just a single LOS ray) and a Two-ray propagation model (modeling a ground reflection ray in addition to the LOS ray for each transmitter).

B.1.1 RECEIVED POWER

In the simulations the following equation is used:

$$P_r (dBm) = P_t (dBm) + PL (dB) \quad (B.1a)$$

where the pathloss (PL) for One-ray model and Two-ray model is given by:

$$PL_{one-ray} (dBm) = G_t (dB) + G_r (dB) - 20\log(d) - 20\log(f) - 32.44 \quad (B.1b)$$

$$PL_{two-ray} = -20\log_{10}(|\mathbf{a}_{21}|^2) \quad (B.1c)$$

where G_t is the transmit antenna gain, G_r is the receive antenna gain, d is distance between transmitter and receiver in km, f is the carrier frequency in MHz and α_{21} is the complex path gain as shown in the system analysis section of Chapter 1.

B.1.2 ANTENNA ARRAY GAIN

For any M -element linearly spaced antenna array of isotropic antennas, the maximum antenna gain is given by

$$G_r = 10\log(M) \quad (B.2)$$

B.1.3 SIGNAL TO NOISE RATIO

$$SNR (dB) = P_r (dBm) - noise \ floor \quad (B.3)$$

where

$$noise \ floor = N_o + NF + 10\log BW$$

$$N_o = 10\log(kT_e) = -174 \frac{dBm}{Hz}$$

$$BW = \text{channel bandwidth (Hz)}, NF = \text{noise figure (dB)} \quad (\text{B.4})$$

B.1.4 TWO-RAY MODEL GEOMETRY

In this section, we give an extensive analysis of the Two-ray model geometry as well as the equations used to approximate the grazing angle and the reflection point. The figures and the equations in this analysis are taken from the presentation slides produced by B. Agee [7].

Figure B.1 illustrates the overall Spherical Two-ray model geometry. Figure B.2 is a normalized version of Figure B.2 where the distances are normalized with respect to the electromagnetic earth radius, R ($4/3$ earth radius). This normalization is used to calculate the azimuth angles and declination angles.

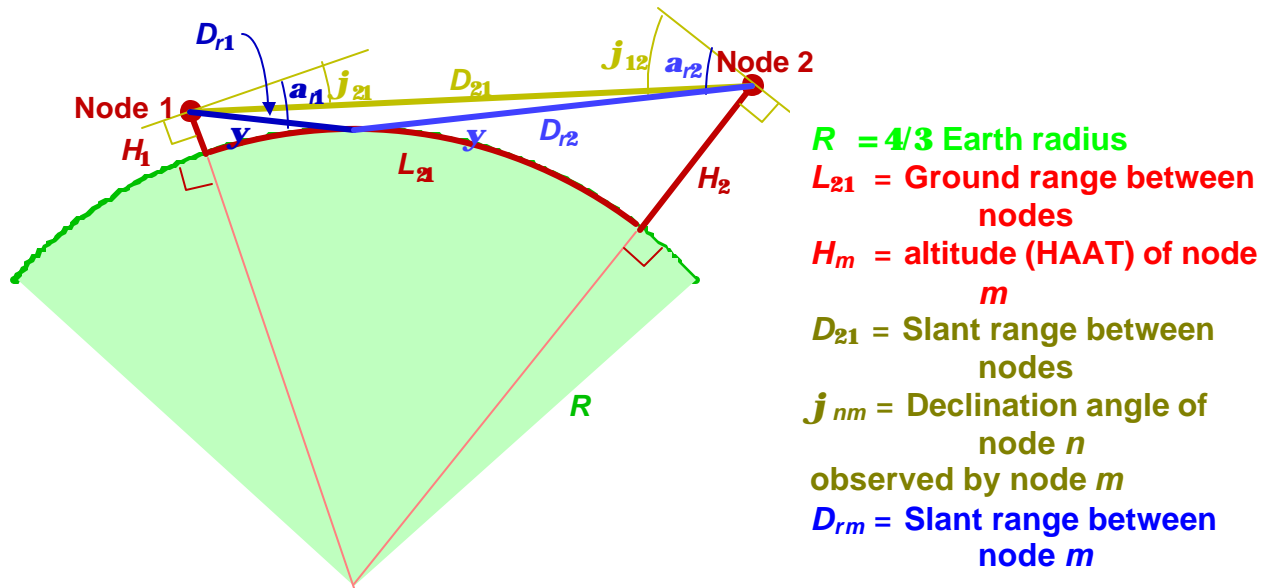
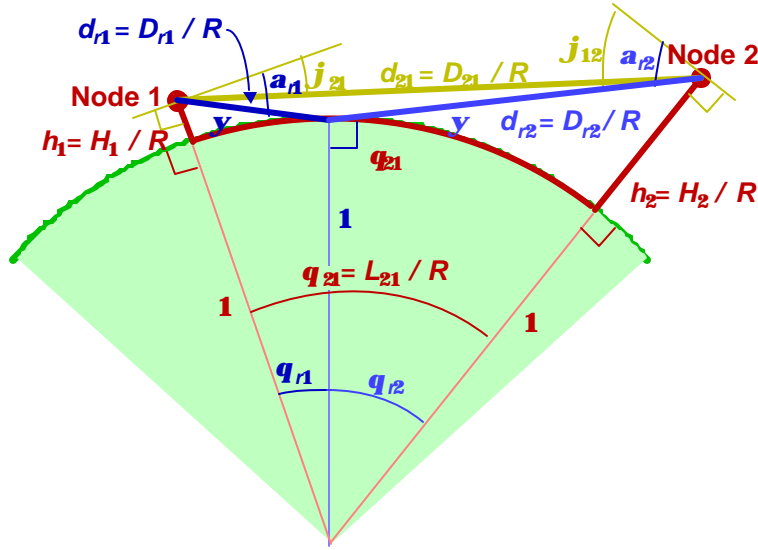


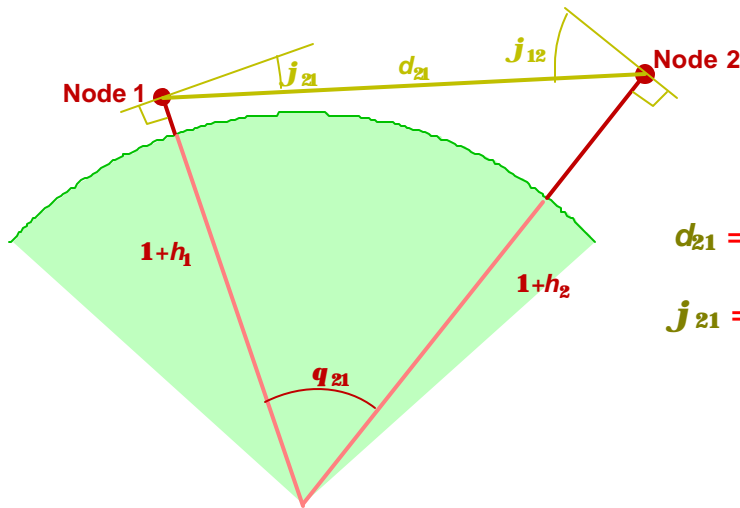
Figure B.1: Spherical Two-ray Model. Node 1 represents the mobile user; node 2 represents the ACN.



$$\begin{aligned}
 q_{21} &= j_{12} + j_{21} \\
 &= q_{r1} + q_{r2} \\
 &= a_{r1} + a_{r2} - 2y \\
 a_{r1} &= q_{r1} + y
 \end{aligned}$$

Figure B.2: Normalized Geometric Two-ray Model.

Figure B.3 depicts the geometry needed to calculate the direct path component parameters. Simple pythagorean theorem is used to calculate the direct LOS slant distance, d_{21} , and the declination angles of the two nodes.



$$\begin{aligned}
 d_{21} &= [(1 + h_1)^2 + (1 + h_2)^2 - 2(1 + h_1)(1 + h_2) \cos(q_{21})]^{1/2} \\
 j_{21} &= \sin^{-1} \left\{ \frac{[(1 + h_1)^2 - (1 + h_2)^2 + d_{21}^2]}{2d_{21}(1 + h_1)} \right\}
 \end{aligned}$$

Figure B.3: Direct Path components

Figure B.4 shows the necessary geometrical calculations for the slant distances in terms of grazing angle (assumed to be known). Finally, figure B.5 depicts the geometry to use for approximating the grazing angle and the reflection point. Since there is no closed form solution

for calculating the grazing angle, Newton-Raphson Recursion is applied to a grazing angle constraint.

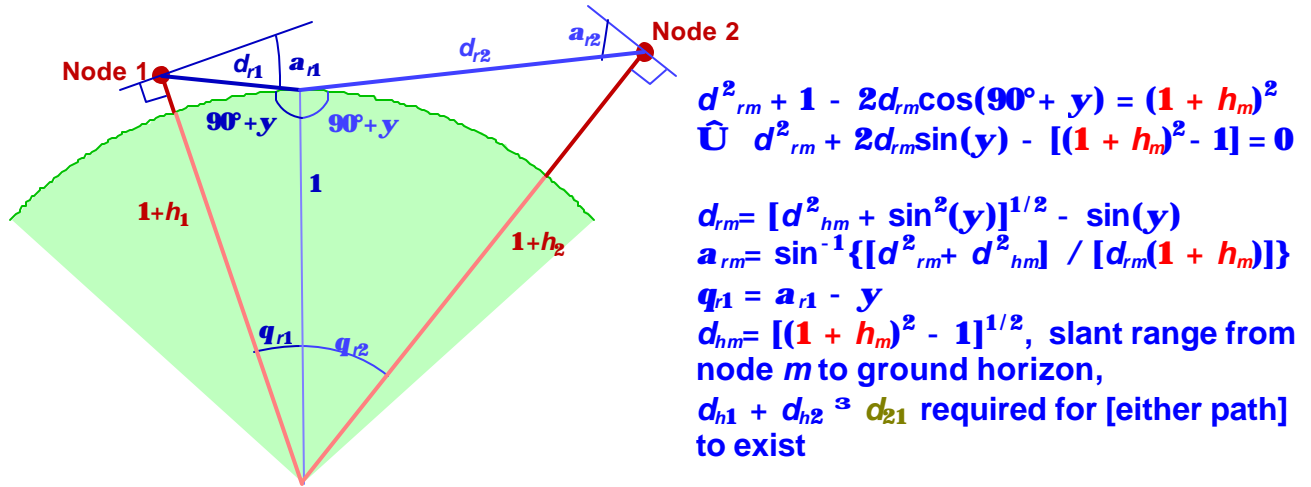


Figure B.4: Reflection path components assuming that the grazing angle is known.

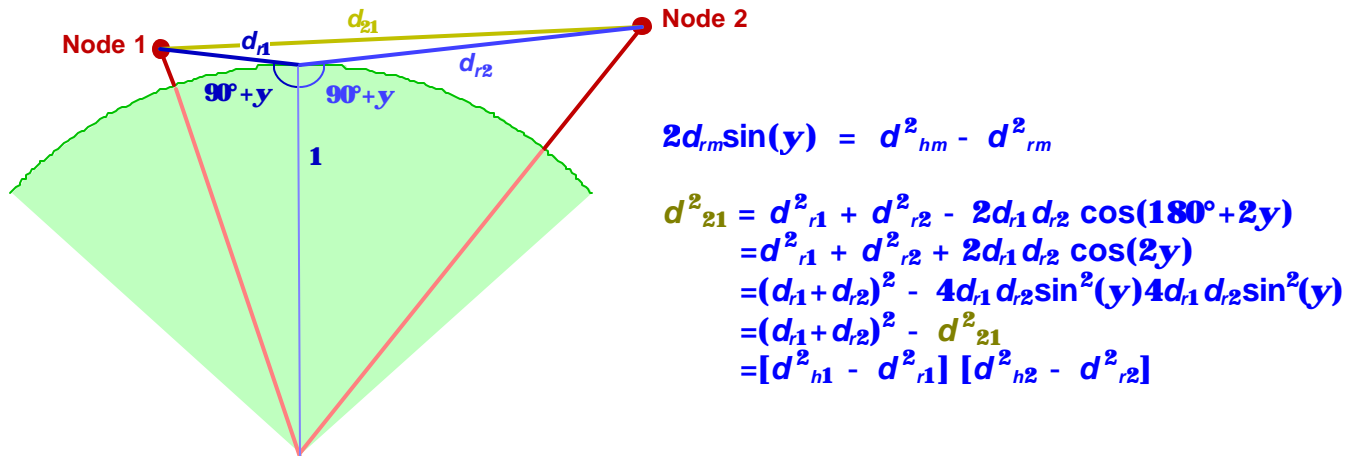


Figure B.5: Geometry for calculating the grazing angle and the reflection point.

In order to approximate the grazing angle and the reflection point we need to pertain to Newton-Raphson Recursion to solve the following constraint:

$$0 = [d_{h1}^2 - d_{r1}^2(\mathbf{x})] [d_{h2}^2 - d_{r2}^2(\mathbf{x})] - [d_{r1}(\mathbf{x}) + d_{r2}(\mathbf{x})]^2 + d_{21}^2$$

$$d_{rm}(\mathbf{x}) = [d_{hm}^2 + x^2]^{1/2} - x, \quad y = \sin^{-1}(x)$$

Once the slant distance, d_{r1} , between the mobile and the reflection point; and slant distance, d_{r2} , between the ACN are approximated, we can apply these results to the path loss formula given in Chapter 1.

APPENDIX C: DERIVATION OF DOPPLER SHIFT AND RATE-DOPPLER

C.1 DOPPLER SHIFT

In this section we will briefly derive analytical expressions for Doppler and Doppler rate-of-change (also called rate-Doppler). Two loitering patterns are considered: race track and circular. We begin with general analytic Doppler expressions in terms of pattern-specific time-varying parameters. Then in two subsequent sections, we derive pattern specific expressions for position, velocity, range-rate, and acceleration.

In the general case, the origin of our coordinate space is arbitrary. All general expressions will make no assumption about the location of the origin. The position of the aircraft and the user are described by the vectors $\vec{r}(t)$ and \vec{r}_u . The classic expression of Doppler frequency is

$$f_d = v_{up} \frac{f_c}{c}, \quad (\text{C.1})$$

where the velocity, f_c , is the carrier frequency, c , is the velocity of light, and \mathbf{n}_{pu} is the velocity of the aircraft in the direction of the user. This is the projection of the aircraft's velocity vector on to a unit-vector *pointing* in the direction of the desired user. The range vector,

$$\Delta\vec{r}(t) = \vec{r}_u - \vec{r}(t)$$

points from the aircraft to the user and has a magnitude of the distance between them. The normalized range vector

$$\Delta\vec{r}(t) / |\Delta\vec{r}(t)|$$

points from the aircraft in the direction of the user such that the dot product,

$$v_{pu} = \vec{v}(t) \cdot \Delta\vec{r}(t) / |\Delta\vec{r}(t)|$$

is the aircraft's velocity in the direction of the user. Hence, the expression for Doppler shift is

$$f_d = \frac{\Delta\vec{r}(t)^T \mathbf{v}(t)}{\|\Delta\vec{r}(t)\|} \frac{f_c}{c}. \quad (\text{C.2})$$

The quantities $\vec{v}(t)$, and $\Delta\vec{r}(t)$ are pattern specific and will be considered later. We can make several observations from this expression. Using the law of cosines, the Doppler shift can also be written as

$$f_d = v_p \frac{f_c}{c} \cos(\Delta\mathbf{q}) \cos(\Delta\mathbf{a}). \quad (\text{C.3})$$

where v_p is the velocity of the plane, $\Delta\theta$ is the difference in azimuth from the plane's direction of flight and $\Delta\alpha$ is the depression angle to the user. The former expression is useful for plotting the time-varying nature of the Doppler shift for a given loitering pattern. The later form is useful for getting an intuitive geometric feel for the Doppler function's behavior.

System analysis shows that for a uniform cell tessellation, as many as ten co-channel interferers may lie within an azimuthal range of 5 degrees relative to the desired user. It is not expected that a 6 to 8 element Nyquist sampled antenna array will have sufficient resolution in elevation to spatially separate these users. The question arises if Doppler is a distinguishing feature between closely spaced co-channel interferers. From (C.3) we see that the answer is no. The cosine relationship in depression angle tells us that differences in depression angle will not translate to significant differences in Doppler. For example, consider two cochannel users with $f_c = 900\text{MHz}$ located at 10° and 3° depression angle² and 0° azimuth. Their Doppler shifts will differ at most by :

$$\frac{[\cos(3^\circ) - \cos(10^\circ)](100\text{m/s})(900\text{MHz})}{3 \times 10^8 \text{ m/s}} = 4.15 \text{ Hz}.$$

For the design of phase locked loops, at the mobile, rate of change of Doppler can be as important as Doppler itself. Taking the temporal derivative of equation (C.2), we arrive at the following expression for rate-Doppler

$$\dot{f}_d = \frac{(\Delta\vec{r}(t) \cdot \dot{\vec{v}}(t) - v_p^2) \|\Delta\vec{r}(t)\| - \Delta\vec{r}(t) \cdot \vec{v}(t) \frac{\partial}{\partial t} \|\Delta\vec{r}(t)\|}{\|\Delta\vec{r}(t)\|^2} \left(\frac{f_c}{c} \right)}. \quad (\text{C.4})$$

² For a spherical earth, these depression angles correspond to approximately 10° and 0° elevation angles, respectively.

Note the rate of change of range, $\frac{\partial}{\partial t} \|\Delta \vec{r}(t)\|$, or range-rate is not the same as the aircraft velocity component in the mobile's direction, v_{pu} . Given an expression for $\Delta \vec{r}(t)$, it is straight forward but tedious to calculate the range-rate. However, it is usually easier to start with the following general equation

$$\frac{\partial}{\partial t} \|\Delta \vec{r}(t)\| = \|\Delta \vec{r}(t)\|^{-1} \left(\frac{1}{2} \frac{\partial}{\partial t} \|\vec{r}(t)\|^2 - \vec{r}_u \cdot \vec{v}(t) \right). \quad (\text{C.5})$$

With these equations we can calculate Doppler and rate Doppler as function of time. For a given loitering pattern, the quantities, $\vec{r}(t)$, \vec{r}_u , $\Delta \vec{r}(t)$, $\frac{\partial}{\partial t} \|\Delta \vec{r}(t)\|$, $\vec{v}(t)$, and $\dot{\vec{v}}(t)$. In the subsequent sections, we derive these quantities for two example loitering patterns.

C.2 RACE-TRACK LOITERING PATTERN.

A race-track loitering pattern is a counter-clockwise pattern around an imaginary ‘‘race-track’’ course shown in figure C.1. The course is divided into two basic parts: a straightaway, and a turn. Straight-aways are assumed to be perfectly straight while turns are perfectly semi-circular. A race-track pattern is depicted in the figure below. The x and y axes are marked. The z -axis is assumed to rise out of the page. For convenience, the planes motion is divided into 6 parts, each depicted with a unique color. Example position vectors of the aircraft and user are also shown. In particular, the position vector of the plane indicates its initial position at time, $t=0$. The arrows for each region indicate the direction of flight. The pattern is completely described with two parameters: the time to fly one stretch of the straight-away, T_{track} , and the time to fly one turn, T_{turn} . Typically, $T_{track} \sim 30$ min, $T_{turn} \sim 1$ min. Hence, this figure is not drawn to scale.

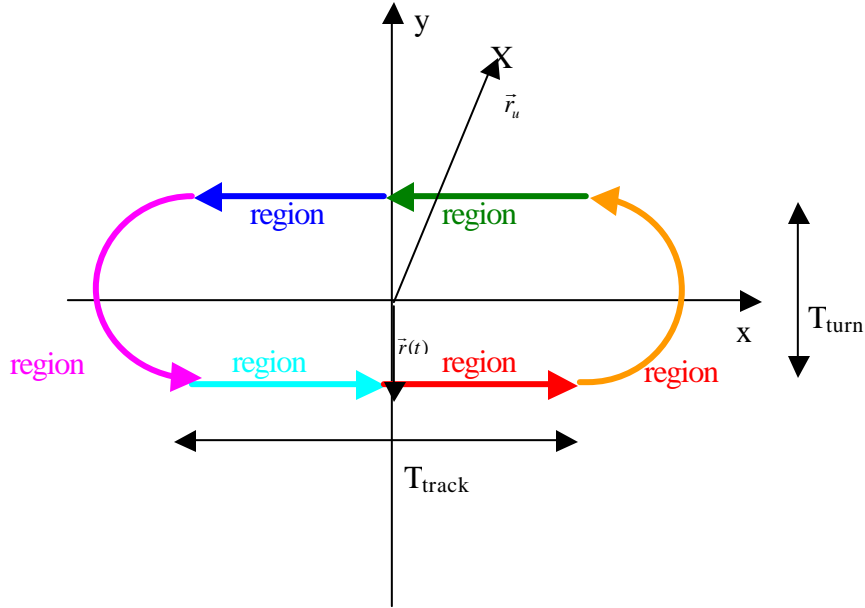


Figure C.1: Diagram of race-track loitering pattern.

We describe the aircraft's motion in a piece-wise linear manner. Let us make the following assumptions in our derivation:

- Flat earth model
- The aircraft speed is constant throughout the entire loitering pattern
- Fixed mobiles
- All vectors are described in a $[z \ y \ x]$ format

For convenience we derive a few preliminary quantities. Let v_p be the aircraft speed. Define the turning radius to be $r_t = v_p T_{turn} / \mathbf{p}$. Let the angular velocity of the aircraft during a turn be $\mathbf{w}_t = \mathbf{p} / T_{turn}$. Define the x -coordinate of the center of the aircraft's turn to be $x_r = v_p T_{turn} / 2$. Finally, define T_i to be time marking the end of a particular region. Therefore,

$$\begin{aligned}
 T_1 &= \frac{1}{2} T_{track} & T_4 &= \frac{3}{2} T_{track} \\
 T_2 &= \frac{1}{2} T_{track} + T_{turn} & T_5 &= \frac{3}{2} T_{track} + 2T_{turn} \\
 T_3 &= T_{track} + T_{turn} & T_6 &= 2(T_{track} + T_{turn})
 \end{aligned} \tag{C.2.1}$$

We will now define the parameters , $\vec{r}(t)$, $\frac{\partial}{\partial t} \|\Delta\vec{r}(t)\|$, $\vec{v}(t)$, and $\dot{\vec{v}}(t)$ for each region.

For region 1, we have:

$$\begin{aligned}\vec{r}(t) &= [h \quad -r_t \quad v_p t]^T \\ \vec{v}(t) &= [0 \quad 0 \quad v_p]^T \\ \frac{\partial}{\partial t} \|\Delta\vec{r}(t)\| &= \|\Delta\vec{r}(t)\|^{-1} (v_p^2 t - \vec{r}_u \cdot \vec{v}(t)) \\ \dot{\vec{v}}(t) &= \mathbf{0}\end{aligned}\tag{C.2.2}$$

Note that the acceleration is zero because the plane is not changing direction.

For region 2, we have:

$$\begin{aligned}\vec{r}(t) &= [h \quad -r_t \cos(\mathbf{w}_t(t-T_1)) \quad r_t \sin(\mathbf{w}_t(t-T_1)) + x_r]^T \\ \vec{v}(t) &= [0 \quad v_p \sin(\mathbf{w}_t(t-T_1)) \quad v_p \cos(\mathbf{w}_t(t-T_1))]^T \\ \frac{\partial}{\partial t} \|\Delta\vec{r}(t)\| &= \|\Delta\vec{r}(t)\|^{-1} (x_r v_p \cos(\mathbf{w}_t(t-T_1)) - \vec{r}_u \cdot \vec{v}(t)) \\ \dot{\vec{v}}(t) &= [0 \quad v_p \mathbf{w}_t \cos(\mathbf{w}_t(t-T_1)) \quad v_p \mathbf{w}_t \sin(\mathbf{w}_t(t-T_1))]^T\end{aligned}\tag{C.2.3}$$

Note the acceleration vector is similar to the classic expression of circular motion $a = -\mathbf{w}^2 r$ except that the motion is not strictly circular. The plane has a z component of h while the acceleration vector has no z component.

For region three and four we have:

$$\begin{aligned}\vec{r}(t) &= [h \quad r_t \quad -v_p(t-T_3)]^T \\ \vec{v}(t) &= [0 \quad 0 \quad -v_p]^T \\ \frac{\partial}{\partial t} \|\Delta\vec{r}(t)\| &= \|\Delta\vec{r}(t)\|^{-1} (v_p^2(t-T_3) - \vec{r}_u \cdot \vec{v}(t)) \\ \dot{\vec{v}}(t) &= \mathbf{0}\end{aligned}\tag{C.2.4}$$

For region five we have:

$$\begin{aligned}
\vec{r}(t) &= [h \quad r_t \cos(\mathbf{w}_t(t-T_4)) \quad -r_t \sin(\mathbf{w}_t(t-T_4)) - x_r]^T \\
\vec{v}(t) &= [0 \quad -v_p \sin(\mathbf{w}_t(t-T_4)) \quad -v_p \cos(\mathbf{w}_t(t-T_4))]^T \\
\frac{\partial}{\partial t} \|\Delta\vec{r}(t)\| &= \|\Delta\vec{r}(t)\|^{-1} (x_r v_p \cos(\mathbf{w}_t(t-T_4)) - \vec{r}_u \cdot \vec{v}(t)) \\
\dot{\vec{v}}(t) &= [0 \quad -v_p \mathbf{w}_t \cos(\mathbf{w}_t(t-T_4)) \quad v_p \mathbf{w}_t \sin(\mathbf{w}_t(t-T_4))]^T
\end{aligned} \tag{C.2.5}$$

For region six we have:

$$\begin{aligned}
\vec{r}(t) &= [h \quad -r_t \quad v_p(t-T_6)]^T \\
\vec{v}(t) &= [0 \quad 0 \quad v_p]^T \\
\frac{\partial}{\partial t} \|\Delta\vec{r}(t)\| &= \|\Delta\vec{r}(t)\|^{-1} (v_p^2(t-T_6) - \vec{r}_u \cdot \vec{v}(t)) \\
\dot{\vec{v}}(t) &= \mathbf{0}
\end{aligned} \tag{C.2.6}$$

C.2.1 CIRCULAR LOITERING PATTERN

An aircraft follows a circular loitering pattern is depicted in Figure C.2. This motion is much simpler than that of a race-track pattern because all parameters may be described with a single set of equations. A circular loitering pattern is illustrated in the figure below. Again, the position vectors of the user and aircraft are illustrated on the figure. The pattern is described in terms of a single parameter: T_{circle} , the time to complete one circle.

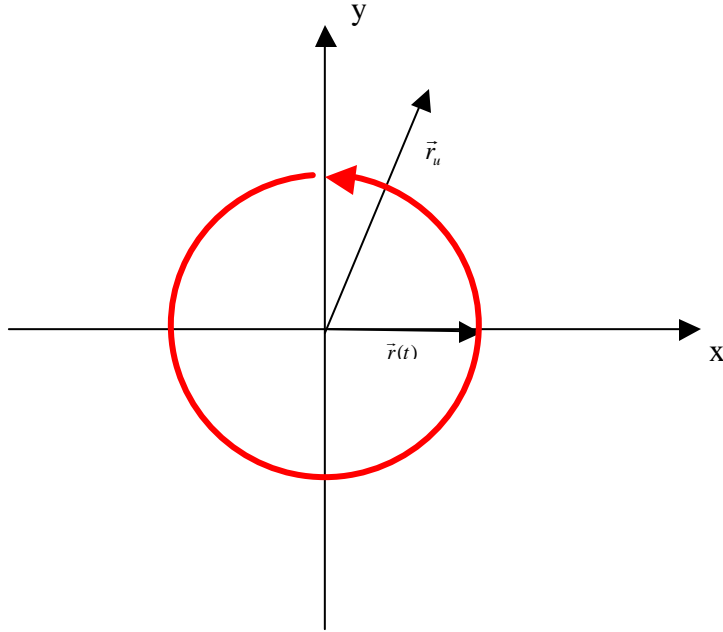


Figure C.2: Diagram of circular loitering pattern.

Let us define a few preliminary parameters. The turning radius of the circle $r_0 = v_p T_{\text{circle}} / (2\pi)$ and the angular velocity of the plane be $\omega_0 = 2\pi / T_{\text{circle}}$. The motion equations are then:

$$\begin{aligned}
 \vec{r}(t) &= [h \quad -r_0 \sin(\omega_0 t) \quad r_0 \cos(\omega_0 t)]^T \\
 \vec{v}(t) &= [0 \quad v_p \cos(\omega_0 t) \quad -v_p \sin(\omega_0 t)]^T \\
 \frac{\partial}{\partial t} \|\Delta \vec{r}(t)\| &= -\frac{\vec{r}_u \cdot \vec{v}(t)}{\|\Delta \vec{r}(t)\|^{-1}} \\
 \dot{\vec{v}}(t) &= [0 \quad -v_p \omega_0 \sin(\omega_0 t) \quad -v_p \omega_0 \cos(\omega_0 t)]^T
 \end{aligned} \tag{C.2.6}$$

APPENDIX D: CIRCULAR ANTENNA ARRAY

Our simulations in this thesis have assumed a circular array geometry as shown in Figure D.1. Consider a single wave-front carrying a signal $s(t)$, impinging on a circular array with a depression angle of α_d , and an azimuth of θ_a . The $K \times 1$ vector of complex, baseband signals experienced by each element, $\vec{x}(t)$, can be expressed as

$$\vec{x}(t) = \vec{a}(\mathbf{a}_d, \mathbf{q}_d) s(t) + \vec{z}(t) \quad (\text{D.1})$$

where $\vec{z}(t)$ is a vector of spatially uncorrelated additive white complex Gaussian noise. The mapping of the received signal (w/o noise) to an array response vector is described with a steering vector, $\vec{a}(\mathbf{a}_d, \mathbf{q}_d)$.

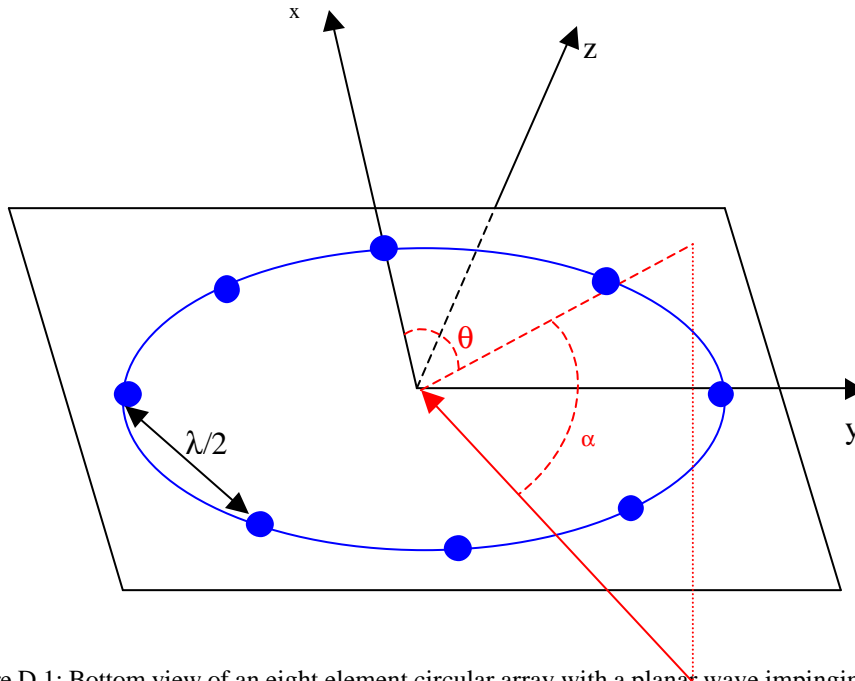


Figure D.1: Bottom view of an eight element circular array with a planar wave impinging on the array at a depression angle of α_d and azimuth of θ_a .

The steering vector for an K element $\lambda/2$ spaced circular array is given as

$$\vec{a}(\mathbf{a}_d, \mathbf{q}_a) = [a_1 \quad \cdots \quad a_K]^T, \quad a_k = \exp\left(jk_R \sin\left(\mathbf{q}_a - \frac{2\mathbf{p}(k-1)}{K}\right) \cos \mathbf{a}_d\right) \quad (\text{D.2})$$

where the constant $\kappa_R = \pi/2 \csc(\pi/K)$.

A linear beam-former forms a single output signal from a linear combination of the antenna elements.

$$y(t) = \vec{w}^H \vec{x}(t) \quad (\text{D.3})$$

where \vec{w} is an arbitrary vector of element weights. Consider a single signal impinging on the array from a depression angle of α_d and an azimuth of θ_a . The optimal-SNR beam-former in spatially uncorrelated additive white complex Gaussian noise is given as

$$\vec{w}_{opt} = \vec{a}(\mathbf{a}_d, \mathbf{q}_a) \quad (\text{D.4})$$

The gain pattern of a beam former indicates the gain in the power of $y(t)$ for a signal received from a certain direction. For a given weight vector, \vec{w} , the gain pattern as a function of azimuth θ , and depression, α , is given as:

$$G(\mathbf{a}, \mathbf{q}) = |\vec{w}^H \vec{a}(\mathbf{a}, \mathbf{q})|^2 \quad (\text{D.5})$$

APPENDIX E: BIBLIOGRAPHY

- [1] T.E. Biedka, M.F. Kahn, "Methods for Constraining a CMA Beamformer to Extract a Cyclostationary Signal," *Second Workshop on Cyclostationary Signals*, Monterey, CA, Aug. 1994.
- [2] Van der Veen, Paulraj, "An Analytical Constant Modulus Algorithm," *IEEE Transactions on Signal Processing*, vol. 44, no. 5, May 1996.
- [3] Van der Veen, "Weighted ACMA," *ICASSP '99, 1999*.
- [4] Castedo, Escudero, Depena, "A Blind Signal Separation Method for Multiuser Communications," *IEEE Transactions on Signal Processing*, vol. 45, no. 5, May 1997.
- [5] J.H. Reed, R. He, "Spectral Correlation of AMPS Signals and its Application to Interference Rejection," *Vehicular Technology Conference*, 1994.
- [6] J. Hamkins, "A Joint Viterbi Algorithm to Separate Cochannel FM Signals," *ICASSP 1998*
- [7] R. Raheli, A. Polydoros, C. Tzou, "Per-Survivor Processing: A General Approach to MLSE in Uncertain Environments," *IEEE Transactions on Communications*, Vol. 43, No. 2/3/4, February/March/April 1995, pp. 354-507.
- [8] A.V. Keerthi, J.J. Shynk, "Separation of Cochannel Signals in TDMA Mobile Radio," *IEEE Transactions on Signal Processing*, Vol.46, No.10, October 1998, pp.2684-2697.
- [9] Y.K. Lee, R. Chandrasekaran, J.J. Shynk, "Separation of Cochannel GSM Signals Using an Adaptive Array," *IEEE Transactions on Signal Processing*, Vol. 47, No.7, July 1999, pp.1977-1987.
- [10] Agee, Bruzzone, Bromberg, "Exploitation of Signal Structure in Array Based Blind Copy and Copy-Aided DF Systems," *Vehicular Technology Conference*, June 1998.

- [11] E.R. Ferrara, Jr. "Frequency domain implementations of periodically time-varying adaptive filters," *IEEE Transactions on Acoustics Speech and Signal Processing*, Vol. 33, No. 8, August 1985, pp. 883-892.
- [12] Ranta, Honkasalo, "Co-Channel Interference Cancelling Receiver for TDMA Mobile Systems," *-Proc. of IEEE ICI, Seattle, 1995*, pp. 17-21.
- [13] Grant, Cavers, "Performance Enhancement Through Joint Detection of Cochannel Signals Using Diversity Arrays," *IEEE Transactions on Communications*, Vol. 46, No. 8, August 1998.
- [14] Giridhar, Chari, Shynk, Gooch, "Joint Demodulation of Cochannel Signals Using MLSE and MAPSD Algorithms," *Proc. of ICASSP, Minneapolis, 1993*, Vol. IV, pp. 160-163, 1993.
- [15] J.H. Reed, A.A. Quilici, and T.C. Hsia, "A frequency domain time-dependent adaptive filter for interference rejection," *IEEE Military Communications Conference*, October 1988, pp. 391-397.
- [16] *TDMA Cellular/PCS –Radio Interface- Mobile Station –Base station Compatibility – Traffic Channels and FSK Control Channel. TIA/EIA/IS-136.2-A.*
- [17] Lindskog, Ahlen, Sternad, "Combined Spatial and Temporal Equalization Using and Adaptive Antenna Array and a Decision Feedback Equalization Scheme," *Proc. Of Int. Conf. On Acoustics, Speech, and Signal Processing*, May 1995.
- [18] Lindskog, Ahlen, Sternad, "Spatio-Temporal Equalization for Multipath Environments in Mobile Radio Applications," *Proc. of the 45th IEEE Vehicular Technology Conference*, pp. 775-779 July, 1995.
- [19] Torlak, Hansen, Xu, "A Fast Blind Source Separation for Digital Wireless Applications," *29th Asilomar Conference on Signals, Systems, & Computers* 1998.

- [20] Giridhar, Shynk, Mathur, Chari, Gooch, "Nonlinear Techniques for the Joint Estimation of Cochannel Signals," *IEEE Transactions on Communications*, Vol 45, No. 4, pp. 473-483, April 1997.
- [21] Tidestav, Ahlen, Sternad, "A Comparison of Interference Rejection and Multiuser Detection," *IEEE International Symposium on Personal, Indoor and Mobile Radio Communications*, pp. 732-736, 1998
- [22] Winters, "Signal Acquisition and Tracking with Adaptive Arrays in the Digital Mobile Radio System IS-54 with Flat Fading," *IEEE Transactions on Vehicular Technology*, Vol. 42, November 1993.
- [23] Fuchs, "Multipath Time-Delay Detection and Estimation," *IEEE Transactions on Signal Processing*, Vol. 47, No.1, January 1999.
- [24] Hallen, Heegard, "Delayed Decision-Feedback sequence Estimation," *IEEE Transactions on Communications*, Vol. 37, No. 5, pp. 435, May 1989.
- [25] Ariyavistakul, Winters, "Joint Equalization and Interference Suppression for High Data Rate Wireless Systems," *Vehicular Technology Conference*, February 1999.
- [26] Ariyavistakul, Winters, Lee, "Optimum Space-Time Processors with Dispersive Interference: Unified Analysis and Required Filter Span," *IEEE Transactions on Communications*, Vol 47, No. 7, July 1999.
- [27] Heidari, Nikias, "Co-Channel Interference Mitigation in the Time-Scale Domain: The CIMTS Algorithm," *IEEE Transactions on Signal Processing*, Vol. 44, No. 9, September 1996.
- [28] Shin, Nikias, "Adaptive Interference Canceller for Narrowband and Wideband Interferences Using Higher Order Statistics," *IEEE Transactions on Signal Processing*, Vol. 42, No. 10, October 1994.
- [29] Petersen, Falconer, "Suppression of Adjacent-Channel, Cochannel, and Intersymbol Interference by Equalizers and Linear Combiners," *IEEE Transactions on*

- Communications*, Vol 42, No. 12, pp. 3109-3117 December 1994.
- [30] Edepalli, Andayam, "Combined Equalization and Cochannel Interference Cancellation for the Downlink Using Tentative Decisions," *Proc. ICASSP*, 1999.
- [31] Ratnavel, Paulraj, Constantinides, "MMSE Space-Time Equalization for GSM Cellular Systems," *Vehicular Technology Conference*, pp. 331-335, 1996.
- [32] Gregory E. Bottomley, Karl J. Molnar, "Adaptive Channel Estimation for Multichannel MLSE Receivers," *IEEE Communication Letters*, Vol.3, No.2, February 1999, pp.40 – 42.
- [33] F. Pipon, P. Chevalier, P. Vila, D. Pirez, "Practical Implementation of a Multichannel Equalizer for a Propagation with ISI and CCI – Application to a GSM Link," *Proc. 47th IEEE Vehicular Technology Conf.*, May 1997, pp. 889-893.
- [34] G.E. Bottomley, K. Jamal, "Adaptive Arrays and MLSE Equalization," *45th IEEE Vehicular Technology Conference*, Volume 1, pages 50-54, 1991.
- [35] H. Yoshino, K. Fukawa, H. Suzuki, "Interference Canceling Equalizer (ICE) for Mobile Radio Communication," *IEEE Transactions on Vehicular Technology*, Vol.46, No.4, November 1997, pp. 849-861.
- [36] S.M. Redl, M.K. Weber, and M.W. Oliphant, *An Introduction to GSM*, Mobile Communications Series, Artech House, Inc., 1995.
- [37] J.D. Laster and J.H. Reed, "Interference Rejection in Digital Wireless Communications," *IEEE Signal Processing Magazine*, pp. 37-62, May 1997.
- [38] K.J. Molnar, G.E. Bottomley, "Adaptive Array Processing MLSE Receivers for TDMA Digital Cellular/PCS Communications," *IEEE Journal on Selected Areas in Communications*, Vol. 16, No.8, October 1998, pp. 1340-1351.
- [39] A.J. Paulraj, B.C. Ng, "Space-Time Modems for Wireless Personal Communications," *IEEE Personal Communications*, February 1998, pp.36-48.

- [40] K. Fukawa, H. Suzuki, "Blind Interference Canceling Equalizer for Mobile Radio Communication," *IEICE Transactions on Communications*, Vol.E77-B, No.5, May 1994, pp. 849-861.
- [41] B. C. W. Lo, K.B. Letaief, "Adaptive Equalization and Interference Cancellation for Wireless Communication Systems," *IEEE Trans. On Communications*, Vol. 47, No. 4, April 1999.
- [42] Alle-Jan vand der Veen, Shipa Talwar, A. Paulraj, "Blind Estimation of Multiple Digital Signals Transmitted over FIR Channels," *Signal Processing Letters*, Vol 2, No. 5, May 1995.
- [43] G. Papanicolaou, K.M. Chugg, "PSP Array Processing for Multipath Fading Channels," *IEEE Transactions on Communications*, Vol. 47, No. 4, April 1999, pp.504-507.
- [44] <http://www.skystation.com/telecom.htm>
- [45] J. Liang, A.J. Paulraj, "Two Stage CCI/ISI Reduction with Space-Time Processing in TDMA Cellular Networks," *Conference Record of Thirtieth Asilomar Conference on Signals, Systems and Computers*, pp. p.607-611
- [46] S. Ratnavel, A.Paulraj, A.G. Constantinides, "MMSE Space-Time Equalization for GSM Cellular Systems," *1996 IEEE 46th Vehicular Technology Conference*, pp.331-335, vol.1, 1996.
- [47] CTIA Web pages, <http://www.wow-com.com/wirelessurvey/>.
- [48] Strategis Group Web page, <http://www.strategisgroup.com/>.
- [49] S. Anderson, M.Millnert, B. Wahlberg, "An Adaptive Array for Mobile Communication Systems," *IEEE Transactions on Vehicular Technology*, Vol. 40, No. 1, February 1991, pp. 231-236.
- [50] Parsons D., *The Mobile Radio Propagation Channel*, Pentech Press, London, 1992.

- [51] Boithias, L., *Radio Wave Propagation*, McGraw-Hill Inc., New York, 1987.
- [53] T.Wu, C. Schlegel, "Interference Cancellation for Narrowband Mobile Communication Systems," *Vehicular Technology Conference '99*.
- [54] Forney, "Maximum-Likelihood Sequence Estimation of Digital Sequences in the Presence of Intersymbol Interference," *IEEE Transactions on Information Theory*, pp.363-378, May 1972.
- [55] Gottfried Ungerboeck, "Adaptive Maximum-Likelihood Receiver for Carrier-Modulated Data-Transmission Systems," *IEEE Transactions on Communications*, vol 22. No. 5, pp. 624-636, May 1974.
- [56] Reed, Hsia, "The Performance of Time-Dependent Adaptive Filters for Interference Rejection," *IEEE Trans. On Acoustics, Speech, and Signal Processing*, Vol. 38, No. 8, August 1990
- [57] W.A. Gardner, "Cyclic Wiener Filtering: Theory and Method," *IEEE Transactions on Communications*, Vol. 41, No. 1, January 1993, pp. 151-163.
- [58] J. Karlsson, J. Heinegard, "Interference Rejection Combining for GSM," *Proc. 5th IEEE ICUPC*, September 1996, pp. 433-437.
- [59] Giridhar, Chari, Shynk, Gooch, Artman, "Joint Estimation Algorithms for Cochannel Signal Demodulation," *Proc. of IEEE ICC, Geneva*, 1993, pp. 1497-1501.
- [60] Hedstrom, Kirilin, "Co-Channel Signal Separation Using Coupled Digital Phase-Locked Loops," *IEEE Transactions on Communications*, vol. 44, no. 10, October 1996.
- [61] Stuller and Hubing, "New Perspectives for Maximum Likelihood Time-Delay Estimation," *IEEE Transactions on Signal Processing*, Vol. 45, No. 3, March 1997.
- [62] Grant and Cavers, "Multiuser Channel Estimation for Detection of Cochannel Signals," www.ensc.sfu.ca/people/grad/grantq

- [63] Iltis, "A Bayesian Maximum-Likelihood Sequence Estimation Algorithm for *a priori* Unknown Channels and Symbol Timing," *IEEE Journal on Selected Areas in Communications*, Vol. 10, No.3, April 1992.
- [64] Hashimoto, "A List-Type Reduced-Constraint Generalization of the Viterbi Algorithm," *IEEE Transactions on Information Theory*, vol. 33, no. 6, pp. 866-976, November 1987.
- [65] van der Veen, Talwar, Paulraj, "A subspace Approach to Blind space-Time Signal Processing for Wireless Communication Systems," *IEEE Transactions on Signal Processing*, vol. 45, no. 1, pp. 173-190 January 1997.
- [66] Sheen, Stuber, "MLSE Equalization and Decoding for Multipath-Fading Channels," *IEEE Transactions on Communications*, vol. 39, no. 10, pp. 1455-1464 October 1991.
- [67] Liu, Xu, "Smart Antennas in Wireless Systems: Uplink Multiuser Blind Channel and Sequence Detection," *IEEE Trans. On Comm.* Vol. 45, no. 2, pp. 187-199 Feb. 1997.
- [68] Jamal, Brismark, "Adaptive MLSE Performance on D-AMPS 1900 Channel," *IEEE Transactions on Vehicular Technology*, vol. 46, no. 3, pp. 634-641 August 1997.
- [69] Krenz, Wesolowski, "Comparative Study of space-Diversity Techniques for MLSE Receivers in Mobile Radio," *IEEE Trans. Vehicular Technology*, vol. 46, no. 3, pp. 653-663 August 1997.
- [70] Godara, "Applications of Antenna Arrays to Mobile Communications, Part 1: Performance Improvement, Feasibility, and system Considerations," vol. 85, no. 7, pp. 1031-1060 July 1997.
- [71] Godara, "Application of Antenna Arrays to Mobile Communications, Part II: Beam-Forming and Direction-of-Arrival Considerations," vol. 85, no. 8, pp. 1195-1245 August 1997.
- [72] Raleigh, Boros, "Joint Space-Time Parameter Estimation for Wireless Communication Channels," *IEEE Trans. on Signal Processing*, vol 46, no. 5, pp. 1333-1343 May 1998.

- [73] Izzo, Paura, Poggi, "An Interference-Tolerant Algorithm for Localization of Cyclostationary-Signal Sources," *IEEE Trans. on Signal Processing*, vol. 40, no. 7, pp. 1682-1686, July 1992.
- [74] R. Chandrasekaran, J.J. Shynk, K. Lai, "A Subspace Method for Separating Cochannel TDMA Signals," *ICASSP 1999*.
- [75] Swindlehurst, "Time Delay and Spatial Signature Estimation Using Known Asynchronous Signals," *IEEE Trans. on Signal Processing*, Vol. 46, No.2, February 1998.
- [76] Jakobsson, Swindlehurst and Stoica, "Subspace-Based Estimation of Time Delays and Doppler Shifts," *IEEE Trans. on Signal Processing*, Vol. 46, No.9, September 1998.
- [77] Wax and Leshem, "Joint Estimation of Time Delays and Directions of Arrival of Multiple Reflections of a Known Signal," *IEEE Trans. on Signal Processing*, Vol. 45, No. 10, October 1997.
- [78] M. Yao, L. Jin, Q. Yin, "Selective Direction Finding for Cyclostationary Signals by Exploitation of New Array Configuration," *ICASSP 1999*.
- [79] V.B. Manimohan, W.J. Fitzgerald, "Direction Estimation Using Conjugate Cyclic Cross-Correlation: More Signals than Sensors," *ICASSP 1999*.
- [80] Alle-Jan Van der Veen, Michaela Van der Veen and A.J. Paulraj, "Joint Angle and Delay Estimation Using Shift-Invariance Properties," *IEEE Signal Processing Letters*, Vol. 4, No. 5, May 1997.
- [81] G. Xu, A. Paulraj, Y. Cho, T. Kailath, "Maximum Likelihood Detection of Co-channel Communication Signals via Exploitation of Spatial Diversity," *26th Asilomar Conference on Signals, Systems and Computers*, Vol. 2, 1992.
- [82] M.C. Vanderveen, Papadias and Paulraj, "Joint Angle and Delay Estimation (JADE) for Multipath Signals Arriving at an Antenna Array," *IEEE Communications Letters*, Vol.1,

- No. 1, January 1997.
- [83] J.W. Modestino, V. Eyuboglu, "Integrated Multielement Receiver Structures for Spatially Distributed Interference Channels," *IEEE Transactions on Information Theory*, Vol. IT-32, No. 2, March 1986, pp. 195-219.
- [84] F.M. Gardner, "A BPSK/QPSK Timing-Error Detector for Sampled Receivers", *IEEE Transactions on Communications*, Vol. 34, No. 5, pp. 423-429, May 1986.
- [85] F.M. Gardner, "Interpolation in Digital Modems – Part I: Fundamentals", *IEEE Transactions on Communications*, Vol. 41, No. 3, pp. 501-507, March 1993.
- [86] A. Paulraj, G.G. Raleigh, "Time Varying Vector Channel Estimation for Adaptive Spatial Equalization," *IEEE Globecom*, Vol.1, 1995.
- [87] L. Erup, F.M. Gardner, R. Harris, "Interpolation in Digital Modems – Part II: Implementation and Performance", *IEEE Transactions on Communications*, Vol. 41, No. 6, pp. 998-1008, June 1993.
- [88] Cowley, "The Performance of Two Symbol Timing Recovery Algorithms for PSK Demodulators", *IEEE Transactions on Communications*, Vol. 42, No. 6, pp. 2345-2355, June 1994.
- [89] Armstrong, and Strickland, "Symbol Synchronization Using Signal Samples and Interpolation", *IEEE Transactions on Communications*, Vol. 41, No. 2, pp. 318-321, February 1993.
- [90] Dooley, and Nandi, "Adaptive Subsample Time Delay Estimation Using Lagrange Interpolators", *IEEE Signal Processing Letters*, vol. 6, no. 3, pp. 65-67, March 1999.
- [91] Armstrong, "Symbol Synchronization Using Baud-Rate Sampling and Data-Sequence-Dependent Signal Processing", *IEEE Transactions on Communications*, Vol. 39, No. 1, pp. 127-132, January 1991.

- [92] K. H. Mueller and M. Muller, "Timing Recovery in Digital Synchronous Data Receivers", *IEEE Transactions on Communications*, Vol. 24, No. 5, pp. 516-531, May 1976.
- [93] Bergmans, Wong-Lam, "A Class of Data-Aided Timing-Recovery Schemes", *IEEE Transactions on Communications*, Vol. 43, No. 2/3/4, pp. 516-531, Feb/March/April 1995.
- [94] Kim, Narasimha, Cox, "Design of Optimal Interpolation Filter for Symbol Timing Recovery", *IEEE Transactions on Communications*, Vol. 45, No. 7, pp. 877-884, July 1997.
- [97] Brian G. Agee, Stephan V. Schell, William Gardner, "Spectral Self-Coherence Restoral: A New Approach to Blind Adaptive Signal Extraction Using Antenna Arrays," *IEEE Proceedings*, Vol 74, No. 40, April 1990.
- [98] C. Tidestav, M. Sternad, A. Ahlen, "Reuse Within a Cell – Interference Rejection or Multiuser Detection," *IEEE Transactions on Communications*, Vol. 47, No. 10, pp. 1511-1522, October 1999.
- [99] Tidestav, Sternad, Ahlen, "Reuse Within a Cell-Interference Rejection or Multiuser Detection?," *Vehicular Technology Conference '99*.
- [100] Ready, Chari, "Demodulation of Cochannel FSK Signals Using Joint Maximum Likelihood Sequence Estimation," *27th Asilomar Conference*, Vol. 2, 1993.
- [102] Tsuji, Xin, Yoshimoto, "Detection of Direction and Number of Impinging Signals in Array Antennas Using Cyclostationarity," *Electronics and Communications in Japan*, Part 1, Vol. 82, No. 10, 1999.
- [103] Agee, "The Least-Squares CMS: A New Technique for Correction of Constant Modulus Signals," *IEEE ICASSP*, April 1986, pp. 953-956.
- [104] Shynk, Keerthi, Mathur, "Steady-State Analysis of the Multistage Constant Modulus Array," *IEEE Transactions on Signal Processing*, Vol. 44, No. 4, April 1996.

- Array,” *IEEE Transactions on Signal Processing*, Vol.44, No.4, April 1996.
- [105] Shynk, Keerthi, Mathur, “Convergence Properties of the Multistage Constant Modulus Array for Correlated Sources,” *IEEE Transactions on Signal Processing*, Vol.45, No.1, January 1997.
- [106] Talwar, Viberg, Paulraj, “Blind Separation of Synchronous Co-Channel Digital Signals Using an Antenna Array – Part I: Algorithms,” *IEEE Transactions on Signal Processing*, Vol. 44, No.5, May 1996, pp. 1184-1197.
- [107] Talwar, Viberg, Paulraj, “Blind Separation of Synchronous Co-Channel Digital Signals Using an Antenna Array – Part II: Performance Analysis,” *IEEE Transactions on Signal Processing*, Vol. 45, No.3, March 1997, pp. 706-718.
- [108] Ranheim A., “A Decoupled Approach to Adaptive Signal Separation Using an Antenna Array,” *IEEE Transactions on Vehicular Technology*, Vol. 48, No. 3, May 1999, pp. 676-682.
- [109] Talwar, Viberg, Paulraj, “Reception of Multiple Co-Channel Digital Signals using Antenna Arrays with Applications to PCS,” *SUPERCOMM/ICC*, Vol. 2, pp. 790-794, 1994.
- [110] Hansen L.K., Xu G., “A Fast Algorithm for the Blind Separation of Digital Co-Channel Signals,” *31st Asilomar Conference*, Vol.2, 1997.
- [111] Dogan M.C, Mendel J.M., “Applications of cumulants to array processing I: Aperture extension and array calibration,” *IEEE Transactions on Signal Processing*, Vol. 43, No.5, May 1995, pp. 1200-1216.
- [112] Dogan M.C, Mendel J.M., “Applications of cumulants to array processing IV: Direction finding in coherent signals case,” *IEEE Transactions on Signal Processing*, Vol. 45, No.9, September 1997, pp. 2265-2276.
- [113] Dogan M.C, Mendel J.M., “Applications of cumulants to array processing III: Blind beamforming for coherent signals,” *IEEE Transactions on Signal Processing*, Vol. 45,

- No.9, September 1997, pp. 2252-2264.
- [115] Agee B.G., "Exploitation of Signal Structure in Array-Based Blind Copy and Copy-Aided DF Systems," *ICASSP Presentation*, May 13, 1998.
- [116] Bottomley G.E., Molnar K.J., Chennakeshu S., "Interference Cancellation with an Array Processing MLSE Receiver," *IEEE Transactions on Vehicular Technology*, Vol.48, No.5, September 1999, pp. 1321-1331.
- [117] R.C. North, R.A. Axford, J.R. Zeidler, "The performance of adaptive equalization for digital communication systems corrupted by interference," *Asilomar1993*, Vol.2, pp. 1548-1554.
- [132] R. Roy, T. Kailath, "ESPRIT-Estimation of Signal Parameters Via Rotational Invariance Techniques," *IEEE Transactions on Acoustics, Speech, and Signal Processing*, Vol.37, No.7, July 1989, pp. 984-994.
- [136] T.S. Rappaport, *Wireless Communications: Principles and Practice*, Prentice Hall, New Jersey, 1996.
- [137] P. Petrus, "Novel Adaptive Array Algorithms and Their Impact on Cellular System Capacity," in *Ph.D. Dissertation, Virginia Polytechnic Institute and State University, Blacksburg*, March 1997.
- [138] J.C. Liberti, T.S. Rappaport, *Smart Antennas for Wireless Communications: IS-95 and Third Generation CDMA Applications*, Prentice Hall, New Jersey, 1999.
- [139] R.O. Schmidt, "Multiple Emitter Location and Signal Parameter Estimation," *Proc. of RADC Spectrum Estimation Workshop*, Griffiss AFB, NY, pp. 243-258, 1979.
- [140] J. Zhang, K.M. Wong, Z.Q. Luo, P.C. Ching, "Blind Adaptive FRESH Filtering for Signal Extraction," *IEEE Transactions on Signal Processing*, Vol.47, No.5, May 1999, pp.1397 – 1402.
- [141] W.A. Gardner, *Cyclostationarity in Communications and Signal Processing*, IEEE Press, NY, 1994.

- NY, 1994.
- [145] M.J. Rude, L.J. Griffiths, "An Untrained, Fractionally-Spaced Equalizer for Co-Channel Interference Environments," *24th Asilomar Conference on Signals, Systems and Computers*, 1992.
- [149] N.W.K. Lo, D.D. Falconer, A.U.H. Sheikh, "Adaptive Equalization for a Multipath Fading Environment with Interference and Noise," *VTC'94*, Vol. 1, 1994.
- [150] N.W.K. Lo, D.D. Falconer, A.U.H. Sheikh, "Adaptive Equalization Techniques for Multipath Fading and Co-Channel Interference," *VTC'93*, 1993.
- [152] B.G. Agee, "Blind Separation and Capture of Communication Signals Using a Multitarget Constant Modulus Beamformer," *Proc. MILCOM*, May 1989, pp. 340-346.
- [157] R. Lupas, S. Verdu, "Linear Multiuser Detectors for Synchronous Code-Division Multiple Access Channels," *IEEE Transactions on Information Theory*, Vol. 35, No. 1, January 1989, pp. 123-136.
- [158] M. Honig, U. Madhow, S. Verdu, "Blind Adaptive Multiuser Detection," *IEEE Transactions on Information Theory*, Vol. 41, No. 4, July 1995, pp. 944-960.
- [169] A. Van der Veen, A. Paulraj, "Singular Value Analysis of Space-Time Equalization in the GSM Mobile System," *ICASSP'96*, Vol. 2, 1996, pp.1073-1076.
- [170] J.G. Proakis, *Digital Communications*, McGraw-Hill, New York, 3rd Ed., 1995.
- [171] K. Abend, B.D. Fritchman, "Statistical Detection for Communication Channels with Intersymbol Interference," *Proc. IEEE*, Vol. 58, May 1970, pp. 779-785.
- [172] M.V. Eyuboglu, S.U.H. Qureshi, "Reduced-state Sequence Estimation with Set Partitioning and Decision Feedback," *IEEE Transactions on Communications*, Vol. 36, January 1988, pp. 13-20.
- [173] G.D. Forney, "The Viterbi Algorithm," *Proceedings of IEEE*, Vol. 61, No.3, March 1973, pp. 268-278.

- 1973, pp. 268-278.
- [174] S. Haykin, *Adaptive Filter Theory*, Third Edition, Prentice-Hall, 1996.
- [175] J.J. Shynk, R.P. Gooch, "The Constant Modulus Array for Cochannel Signal Copy and Direction Finding," *IEEE Transactions on Signal Processing*, Vol. 44, No. 3, March 1996.
- [176] R.P. Gooch, J.D. Lundell, "The CM Array: An Adaptive Beamformer for Constant Modulus Signals," *Proc. ICASSP, Tokyo, Japan*, April 1986.
- [177] B.J. Sublett, R.P. Gooch, S.H. Goldberg, "Separation and Bearing Estimation of Cochannel Signals," *Proc. of IEEE Military Communications Conference*, May 1989, pp. 629-634.
- [178] R. Lonski, R.P. Gooch, "An experimental angle of arrival system," *Proc. of the Asilomar Conf. on Signals, Systems, and Computers*, November 1991, pp. 969-973.
- [179] R.D. Hughes, E.J. Lawrence, L.P. Withers, "A Robust CMA Adaptive Array for Multiple Narrowband Sources," *Proc. of the Asilomar Conf. on Signals, Systems, and Computers*, November 1992, pp. 35-39.
- [180] J. Capon, "High Resolution Frequency-Wavenumber Spectral Analysis," *Proc. of IEEE*, Vol. 57, No. 8, August 1969, pp. 1408-1418.
- [181] J. Capon, "Maximum Likelihood Spectral Estimation," *Nonlinear Methods of Spectral Analysis*, Ed. By S. Haykin, Springer, NY, 1979.
- [182] A.J. Barabell, "Improving the Resolution Performance of Eigenstructure-based Direction Finding Algorithms," *Proc. of ICASSP -83*, 1983, pp. 336-339.
- [183] S.V. Schell, Calabretta, W.A. Gardner, B.G. Agee, "Cyclic MUSIC Algorithms for Signal Selective DOA Estimation," *Proc. of ICAASP -89*, 1989, pp. 2278-2281.
- [184] D. Feldman, L.J. Griffiths, "A Constraint Projection Approach for Robust Adaptive Beamforming," *Proc. of ICASSP May 1991*, pp. 1281-1284.

- Beamforming,” *Proc. of ICASSP*, May 1991, pp. 1381-1384.
- [185] J.E. Evans, J.R. Johnson, D.F. Sun, “High Resolution Angular Spectrum Estimation Techniques for Terrain Scattering Analysis and Angle of Arrival Estimation in ATC Navigation and Surveillance System,” *MIT Lincoln Lab.*, Lexington, MA, Rep. 582, 1982.
- [186] T.J. Shan, M. Wax, T. Kailath, “On Spatial Smoothing for Estimation of Coherent Signals,” *ICASSP*, Vol. ASSP-33, August 1985.
- [187] K. Takao, N. Kikuma, “An Adaptive Array Utilizing an Adaptive Spatial Averaging Technique for Multipath Environments,” *IEEE Trans. on Antennas and Propagation*, Vol. AP-35, No. 12, December 1987, pp. 1389-1396.
- [188] F. Haber, M. Zoltowski, “Spatial Spectrum Estimation in a Coherent Signal Environment Using an Array in Motion,” *IEEE Trans. on Antennas and Propagation*, Vol. AP-34, March 1986, pp. 301-310.
- [189] M.J. Rude, L.J. Griffiths, “Incorporation of Linear Constraints into the Constant Modulus Algorithm,” *Proc. of ICASSP*, Glasgow, Scotland, UK, May 1989.
- [190] W.A. Gardner, “Simplification of MUSIC and ESPRIT by Exploitation of Cyclostationarity,” *Proc. of IEEE*, Vol. 76, July 1988, pp. 845-847.
- [192] G. Gelli, L. Izzo, “Minimum-Redundancy Linear Arrays for Cyclostationary-based Source Location,” *IEEE Transactions on Signal Processing*, Vol. 45, October 1997, pp.2605-2608.
- [194] S.V. Schell, B.G. Agee, “Application of the SCORE Algorithm and SCORE Extensions to Sorting in the Rank-L Spectral Self Coherence Environment,” *Proc. of the 22nd Asilomar Conf. on Signals, Systems, and Computers*, December 1988, pp. 274-278.
- [195] S.V. Schell, W.A. Gardner, “Maximum likelihood and Common Factor Analysis-based Blind Adaptive Spatial Filtering for Cyclostationary Signals,” *Proc. ICAASP*,

- Minneapolis, MN, April 1993, pp. 292-295.
- [196] T.E. Biedka, "Subspace Constrained SCORE Algorithms," *Proc. of Asilomar Conf. on Signals, Systems, and Computers*, November 1993, pp. 716-720.
- [197] S. Verdu, "Minimum Probability of Error for Asynchronous Gaussian Multiple-Access Channels," *IEEE Transactions on Information Theory*, vol IT-32, no. 1, January 1986.
- [198] G.J. Bierman, *Factorization Method for Discrete Sequential Estimation*, Academic Press, New York, 1977.
- [200] R.M. Buehrer, A. Kaul, S. Striglis, and B.D. Woerner, "Analysis of DS-CDMA Parallel Interference Cancellation with Phase and Timing Errors," *IEEE Journal on Selected Areas in Communications*, vol. 14, pp. 1522-1535, October 1996.
- [201] S.N. Diggavi, A. Paulraj, "Performance of Multisensor Adaptive MLSE in fading channels," *Proc. IEEE VTC*, pp. 2148-2152, May 1997.
- [202] E. Lindskog, "Multi-channel Maximum Likelihood Sequence Estimation," *Proc. IEEE VTC*, pp. 715-719, May 1997.
- [203] K. Fukawa, H. Suzuki, "Blind Interference Canceling Equalizer for Mobile Radio Communications," *IEICE transactions on communications*, Vol. E77-B, No. 5, May 1994.
- [204] R. Mendoza, J.H. Reed, T.C. Hsia, B.G. Agee, "Interference Rejection Using the Time-Dependent Constant Modulus Algorithm (CMA) and the Hybrid CMA/Spectral Correlation Discriminator," *IEEE Transactions on Signal Processing*, Vol. 39, No. 9, September 1991, pp. 2108 – 2111.
- [205] Van Etten, "Maximum Likelihood Receiver for Multiple Channel Transmission Systems," *IEEE Transactions on Communications*, pp. 276, vol. 24, February, 1976.
- [206] Liu, Xu, Tong, Kailath, "Recent developments in Blind Channel Equalization: from Cyclostationarity to Subspaces," *Signal Processing*, pp. 83-89, vol 50, April 1996.

VITA

Saffet Bayram was borne in Cyprus on May 5, 1977. He received his Bachelor of Science degree in Electrical Engineering from Pennsylvania State University, University Park Campus, PA in May 1994. Saffet started his Master's program in Electrical Engineering at Virginia Polytechnic Institute and State University in Fall of 1998. He joined Mobile and Portable Radio Research Group (MPRG) at Virginia Tech in Fall of 1999 as a Graduate Research Assistant. His research interests are space-time processing for overloaded antenna arrays (algorithm development) and timing delay estimation techniques for multi-user communication systems.